

NASA/TM—2001-210811



A Hybrid Numerical Method for Turbulent Mixing Layers

Nicholas J. Georgiadis
Glenn Research Center, Cleveland, Ohio

National Aeronautics and
Space Administration

Glenn Research Center

Acknowledgments

I would like to thank my advisor, Professor J. Iwan D. Alexander, for his mentoring, teaching, and continual enthusiasm for my work. I also want to thank my co-advisor, Professor Eli Reshotko, for instructing and guiding me during my entire doctoral program. I am very fortunate to have worked with Professor Alexander and Professor Reshotko. Thanks are also due to Professor Yasuhiro Kamotani and Professor Robert Edwards for serving on my thesis committee. I am grateful for the support I received from my supervisors at NASA Glenn Research Center, Dr. Rickey Shyne and Mr. Bernard Blaha. I also want to acknowledge the programmatic support of this work as a base research project provided by Mr. Waldo Acosta and Ms. Mary Jo Long-Davis. Special acknowledgment is due to Mr. James DeBonis. The daily interaction with him on the topics of computational methods and LES was invaluable to this work and made the process enjoyable. I thank Mr. Chanthy Iek for being my study partner for much of the doctoral coursework. Thanks also to Dr. Thomas Barber, Dr. Ray Hixon, Dr. Philippe Spalart, and Mr. Dennis Yoder for the informative discussions on computational methods for turbulent flows.

Available from

NASA Center for Aerospace Information
7121 Standard Drive
Hanover, MD 21076

National Technical Information Service
5285 Port Royal Road
Springfield, VA 22100

Available electronically at <http://gltrs.grc.nasa.gov/GLTRS>

TABLE OF CONTENTS

	Page
List of Tables	v
List of Figures	vii
List of Symbols	xiii
Abstract	xvii
 Chapters:	
1. Introduction	1
1.1 RANS Methods	4
1.2 LES Methods	9
1.3 Hybrid RANS-LES Methods	13
1.4 Overview and Objectives of the Current Work	15
1.5 Outline of the Dissertation	15
2. Formulation of the RANS and LES Equations	19
2.1 Navier-Stokes Equations of Motion	19
2.2 Mass-Weighted RANS Equations	22
2.3 Spatially Filtered LES Equations	30
2.4 Turbulence Modeling	37
2.4.1 RANS Turbulence Model	39
2.4.2 LES Subgrid Scale Model	44

3.	Solution Procedure	49
3.1	Governing Equations	49
3.2	Numerical Method	55
3.3	Extension of the Gottlieb-Turkel Scheme to Generalized Coordinates	57
3.3.1	Generalized Coordinates	58
3.3.2	Time Step Calculation	60
3.3.3	Numerical Dissipation	61
4.	RANS Calculations of Wall Boundary Layers	65
4.1	Incompressible Laminar Boundary Layer	67
4.2	Incompressible Turbulent Boundary Layer	74
4.3	Compressible Turbulent Boundary Layers	81
4.3.1	Mach 1.91 Flat Plate Flow	85
4.3.2	Mach 1.36 Flat Plate Flow	92
5.	Two Dimensional Mixing Layer Calculations	99
5.1	Experimental Configuration	99
5.2	Two Dimensional Computational Modeling	102
5.3	Axial Grid Density Effects	108
5.4	Boundary Condition Effects	130
6.	Three Dimensional Mixing Layer Calculations	149
6.1	Three Dimensional Computational Modeling	149
6.2	Three Dimensional Simulations	151
7.	Conclusions and Recommendations	177
Appendices:		
A.	Accuracy Analysis of the Gottlieb-Turkel Scheme	185
B.	Transformation Metrics	191
C.	Turbulent Time Averaging Procedure	195
D.	Time Series of Initial Mixing Layer Development	199
Bibliography		209

LIST OF TABLES

Table	Page
5.1 Flow conditions for case 2 of the Goebel-Dutton experiments	102
5.2 Comparison of boundary layer quantities at splitter plate trailing edge	103
5.3 Comparison of axial grid spacings .	109

LIST OF FIGURES

Figure	Page
1.1 Schematic of mixing layer demonstrating the hybrid RANS/LES approach	16
4.1 Schematic of flat plate boundary layer	66
4.2 Computational grid for the incompressible laminar flat plate case . .	67
4.3 Skin friction for incompressible laminar boundary layer	70
4.4 Velocity profiles for incompressible laminar boundary layer	72
4.5 Boundary layer thickness for incompressible laminar boundary layer .	73
4.6 Displacement thickness for incompressible laminar boundary layer . .	73
4.7 Momentum thickness for incompressible laminar boundary layer . .	74
4.8 Computational grid for the incompressible turbulent flat plate case .	76
4.9 Skin friction for the incompressible turbulent boundary layer	77
4.10 Velocity profile for the incompressible turbulent boundary layer at $Re_x = 1,050,000$	78
4.11 Velocity profile for the incompressible turbulent boundary layer at $Re_x = 1,050,000$ using wall coordinates	78
4.12 Boundary layer thickness for incompressible turbulent boundary layer	79
4.13 Displacement thickness for the incompressible turbulent boundary layer	79

4.14 Momentum thickness for the incompressible turbulent boundary layer	80
4.15 Computational grid for the Mach 1.91 turbulent flat plate case using the wall-integration method	86
4.16 Computational grid for the turbulent Mach 1.91 flat plate case using the Ota-Goldberg wall function	86
4.17 Skin friction for the Mach 1.91 turbulent boundary layer	88
4.18 Velocity profile for the Mach 1.91 turbulent boundary layer at $Re_x = 4,000,000$	88
4.19 Velocity profile for the Mach 1.91 turbulent boundary layer at $Re_x = 4,000,000$ using wall coordinates	89
4.20 Boundary layer thickness for the Mach 1.91 turbulent boundary layer	90
4.21 Displacement thickness for the Mach 1.91 turbulent boundary layer	90
4.22 Momentum thickness for the Mach 1.91 turbulent boundary layer	91
4.23 Computational grid for the turbulent Mach 1.36 flat plate case using the wall-integration method	93
4.24 Computational grid for the turbulent Mach 1.36 flat plate case using the Ota-Goldberg wall function	93
4.25 Skin friction for the Mach 1.36 turbulent boundary layer	94
4.26 Velocity profile for the Mach 1.36 turbulent boundary layer at $Re_x = 4,000,000$	95
4.27 Velocity profile for the Mach 1.36 turbulent boundary layer at $Re_x = 4,000,000$ using wall coordinates	95
4.28 Boundary layer thickness for the Mach 1.36 turbulent boundary layer	96
4.29 Displacement thickness for the Mach 1.36 turbulent boundary layer	97

4.30 Momentum thickness for the Mach 1.36 turbulent boundary layer	97
5.1 Schematic of Goebel-Dutton mixing layer experiment	101
5.2 Schlieren photograph of the Goebel-Dutton mixing layer (from Ref. 34, used with permission)	115
5.3 Computational grid for the 200 axial grid point case	116
5.4 Comparison of computational grids near the splitter plate trailing edge	117
5.5 Instantaneous density contours for the 200 axial grid point case	118
5.6 Instantaneous entropy contours for the 200 axial grid point case	119
5.7 Instantaneous density contours for the 400 axial grid point case	120
5.8 Instantaneous entropy contours for the 400 axial grid point case	121
5.9 Instantaneous density contours for the baseline 800 axial grid point case	122
5.10 Instantaneous entropy contours for the baseline 800 axial grid point case	123
5.11 Time-averaged axial velocity profiles for 2D hybrid calculations investigating axial grid density effects	124
5.12 Profiles of u_{rms} for 2D hybrid calculations investigating axial grid density effects	126
5.13 Profiles of v_{rms} for 2D hybrid calculations investigating axial grid density effects	128
5.14 Comparison of computational grids using 800 axial points, near the splitter plate trailing edge	136
5.15 Computational grid for the 800 axial grid point case with the mixing section walls removed (every fourth point shown in each direction) . .	137
5.16 Instantaneous density contours for the 800 axial grid point case with a sharp trailing edge for the splitter	138

5.17 Instantaneous entropy contours for the 800 axial grid point case with a sharp trailing edge for the splitter	139
5.18 Instantaneous density contours for the 800 axial grid point case with mixing section walls removed	140
5.19 Instantaneous entropy contours for the 800 axial grid point case with mixing section walls removed	141
5.20 Time-averaged axial velocity profiles for 2D hybrid calculations investigating boundary condition effects	142
5.21 Profiles of u_{rms} for 2D hybrid calculations investigating boundary condition effects	144
5.22 Profiles of v_{rms} for 2D hybrid calculations investigating boundary condition effects	146
6.1 Instantaneous density contours for the 200 axial grid point case (3D)	159
6.2 Instantaneous entropy contours for the 200 axial grid point case (3D)	160
6.3 Instantaneous density contours for the 400 axial point case using the standard turbulent length scale and $C_s = 0.10$	161
6.4 Instantaneous entropy contours for the 400 axial point case using the standard turbulent length scale and $C_s = 0.10$	162
6.5 Schlieren photograph of the Clemens-Mungal experiment near the trailing edge of the splitter plate, showing vortex shedding followed by a transition to turbulence (from Ref. 21, used with permission)	163
6.6 Comparison of density contours near splitter trailing edge	164
6.7 Instantaneous density contours for the 400 axial point case using the standard turbulent length scale and $C_s = 0.24$	165
6.8 Instantaneous entropy contours for the 400 axial point case using the standard turbulent length scale and $C_s = 0.24$	166

6.9 Instantaneous density contours for the 400 axial point case using the modified turbulent length scale and $C_s = 0.24$	167
6.10 Instantaneous entropy contours for the 400 axial point case using the modified turbulent length scale and $C_s = 0.24$	168
6.11 Time-averaged axial velocity profiles for 3D hybrid calculations	169
6.12 Profiles of u_{rms} for 3D hybrid calculations	171
6.13 Profiles of v_{rms} for 3D hybrid calculations	173
6.14 Instantaneous density contours for the 800 axial point case using the modified turbulent length scale and $C_s = 0.24$	175
6.15 Instantaneous entropy contours for the 800 axial point case using the modified turbulent length scale and $C_s = 0.24$	176
D.1 Time series of density contours for the 3D hybrid calculation using the standard length scale expression and $C_s = 0.10$	201
D.2 Time series of entropy contours for the 3D hybrid calculation using the standard length scale expression and $C_s = 0.10$	205

LIST OF SYMBOLS

a	speed of sound
A^+	Van Driest coefficient
b	local mixing layer width
C_f	skin friction coefficient
C_I	Smagorinsky subgrid model (second) coefficient
C_P	specific heat at constant pressure
C_s	Smagorinsky subgrid model (first) coefficient
C_v	specific heat at constant volume
C_x, C_y, C_z	Corrector operators
D	matrix filter function
ϵ	internal energy
E, F, G	flux vectors
E_t	total energy
f	frequency
\hat{f}	Reynolds-averaged variable using mass (Favre) weighting
\tilde{f}	Spatially-filtered variable using mass (Favre) weighting
F_{kleb}	Klebanoff intermittency function
G	filter function

h	static enthalpy
H	mixing duct height
J	Jacobian of coordinate transformation
k	thermal conductivity
k^{sgs}	effective subgrid thermal conductivity
k^T	effective turbulent thermal conductivity
\hat{k}	turbulent kinetic energy
\check{k}	unresolved turbulent kinetic energy
ℓ_{mix}	turbulent mixing length
L	flat plate length
M_c	convective Mach number
P	static pressure
P_x, P_y, P_z	Predictor operators
Pr	Prandtl number
Pr^T	turbulent Prandtl number
q_j	heat flux
q_j^{sgs}	subgrid scale heat flux
q_j^T	turbulent heat flux
\mathbf{Q}	conservation variables vector
r	recovery factor
R	ideal gas constant
Re_x	Reynolds number based on axial position
Re_θ	Reynolds number based on momentum thickness
S	entropy

S_{ij}	rate of strain tensor
St	Strouhal number
t	time
T	static temperature
T_t	stagnation temperature
T_w	wall temperature
u, v, w	velocity components
u_e	velocity at boundary layer edge
u_i	velocity tensor
u_τ	shear velocity
u^+	velocity normalized with the shear velocity
x, y, z	Cartesian coordinates
x_i	position tensor
y^+	wall normal coordinate
α	coefficient of outer layer turbulent viscosity
α_n	filter function coefficient
δ	boundary layer thickness
δ_{ij}	Kronecker delta function
δ_v	velocity thickness
δ^*	displacement thickness
Δ	filter width
Δt	time step
ΔU	freestream velocity difference
$\Delta x, \Delta y, \Delta z$	Cartesian grid spacing

θ	momentum thickness
γ	compressibility parameter
κ	Von Karman constant
λ	second coefficient of viscosity
μ	first coefficient of viscosity
μ^T	turbulent viscosity
μ_{inner}^T	inner region turbulent viscosity
μ_{outer}^T	outer region turbulent viscosity
μ^{sgs}	subgrid scale turbulent viscosity
ξ, η, ζ	generalized coordinates
π	subgrid scale rate of strain parameter
ρ	density
τ	time period for Reynolds averaging
τ_{ij}	viscous stress tensor
τ_{ij}^T	turbulent or Reynolds stress
τ_{ij}^{sgs}	subgrid scale stress
τ_w	wall shear stress

A Hybrid Numerical Method for
Turbulent Mixing Layers

Abstract

by

NICHOLAS JACOB GEORGIADIS

A hybrid method has been developed for simulations of compressible turbulent mixing layers. Such mixing layers dominate the flows in exhaust systems of modern day aircraft and also those of hypersonic vehicles currently under development. The method developed here is intended for configurations in which a dominant structural feature provides an unsteady mechanism to drive the turbulent development in the mixing layer.

The hybrid method uses a Reynolds-averaged Navier-Stokes (RANS) procedure to calculate wall bounded regions entering a mixing section, and a Large Eddy Simulation (LES) procedure to calculate the mixing dominated regions. A numerical technique was developed to enable the use of the hybrid RANS-LES method on stretched, non-Cartesian grids. Closure for the RANS equations was obtained using the Cebeci-Smith algebraic turbulence model in conjunction with the wall-function approach of Ota and Goldberg. The wall-function approach enabled a

continuous computational grid from the RANS regions to the LES region. The LES equations were closed using the Smagorinsky subgrid scale model.

The hybrid RANS-LES method is applied to a benchmark compressible mixing layer experiment. Preliminary two dimensional calculations are used to investigate the effects of axial grid density and boundary conditions. Vortex shedding from the base region of a splitter plate separating the upstream flows was observed to eventually transition to turbulence. The location of the transition, however, was much further downstream than indicated by experiments.

Actual LES calculations, performed in three spatial directions, also indicated vortex shedding, but the transition to turbulence was found to occur much closer to the beginning of the mixing section, which is in agreement with experimental observations. These calculations demonstrated that LES simulations must be performed in three dimensions. Comparisons of time-averaged axial velocities and turbulence intensities indicated reasonable agreement with experimental data.

CHAPTER 1

INTRODUCTION

The use of computational fluid dynamics (CFD) to assist in the analysis and design of aerospace vehicles and their components has substantially increased in recent years. For analyzing one particular class of flows, that of aircraft engine exhaust nozzles, Reynolds-averaged Navier-Stokes (RANS) codes have been used extensively by government organizations (i.e. NASA) and aerospace companies. Exhaust nozzles being developed for modern day subsonic commercial aircraft typically have multiple streams with a core flow and one or more bypass streams which mix with the high energy core flow before exiting the nozzle to lower jet noise while maintaining high thrust levels. Similarly in NASA's High-Speed Research program, the engine exhaust systems for the proposed supersonic transport were designed to be mixer-ejector nozzles, which entrain secondary air into the exhaust nozzle to mix with the core engine stream, again with the goal of simultaneously lowering jet noise and maintaining sufficient thrust [91]. Propulsion systems currently under development for use on hypersonic and reusable space launch vehicles, such as the Turbine-Based Combined-Cycle (TBCC) and Rocket-Based Combined-Cycle (RBCC) concepts also employ mixer-ejector ducts. The TBCC concept [30, 104]

uses a mixer-ejector to integrate a turbine engine with a ramjet into a propulsion system with a common nozzle, while the RBC'C' concept [28, 101, 103] integrates a rocket with a ramjet, again with a common nozzle.

The flows in these nozzle systems all have compressible turbulent mixing as the dominant flow characteristic. RANS codes used by research and development engineers to analyze these nozzles have employed turbulence models to replace the unsteady turbulent motion with an effective eddy viscosity. Unfortunately, no turbulence model has been developed to date which is able to accurately represent the turbulent motion for such nozzle flows. References [5] and [32] show that the “state of the art” turbulence models available in production-use RANS codes have major deficiencies in predicting turbulent mixing in nozzle and jet flows involving compressibility, high temperatures, and three-dimensionality.

The known limitations of RANS techniques to calculate complex turbulent flows, coupled with continually increasing computing power, have led to interest in more sophisticated calculation techniques such as direct numerical simulation (DNS) and large eddy simulation (LES). DNS is currently limited by computer hardware to very simple flows at low Reynolds numbers, and LES, which directly solves for the large turbulent scales and limits empirical modeling to the smallest scales, is becoming practical for more complex flows at higher Reynolds numbers. Birch [10] and Bradshaw [14] suggest that LES techniques offer the best prospects for improving the capability to calculate turbulent flows, particularly for flow regions not including wall boundary layers.

As a result, an LES-based technique is an attractive option for calculating the mixing dominated regions of nozzle flows. However, applying such an LES technique simultaneously to the wall bounded regions that enter the mixing region (which are an important part of multi-stream nozzles that should be calculated accurately) will not be practical in the near future. This is because computational resources far greater than those available today would be required to capture the wide range of turbulent time and length scales that are important in such a problem. These turbulent scales range from very small eddies in the wall boundary layers to very large eddies in the developing mixing layer.

While RANS-based methods have major deficiencies in predicting compressible mixing layers and inherently are not formulated for calculation of unsteady turbulent flows, they have been shown to predict the mean flow behavior of wall bounded regions quite well, particularly in the absence of adverse pressure gradients. As a result, it would be desirable to combine a RANS-based technique for the wall boundary layers upstream of the mixing region with an LES-based technique for the downstream unsteady, turbulent mixing region. The development of such a hybrid RANS/LES approach is the subject of this work.

In the rest of this chapter, a survey of methods currently used for the computational modeling of nozzle flows dominated by compressible turbulent mixing and new techniques under development are presented. First, RANS methods are discussed in section 1.1 with emphasis placed on turbulence modeling, which is most frequently considered the limiting factor of such CFD simulations. Next, a discussion of LES techniques, as applied to nozzle and jet flow fields, is presented in section 1.2.

Section 1.3 discusses hybrid methods, which have recently been proposed for flows in which wall boundary layer regions may be adequately calculated with a RANS method, while unsteady regions with large scale recirculations are calculated with an LES method. An overview of the hybrid method developed in this work is presented in section 1.4. Finally, an outline of this dissertation is provided in section 1.5.

1.1 RANS Methods

The RANS codes used to simulate the nozzle flows discussed at the beginning of this chapter are largely general-purpose flow solvers, capable of handling a variety of turbulent flows extending beyond only nozzle and jet problems. State-of-the-art turbulence models, such as Reynolds-stress closures, have found their way into codes intended for basic research and simple flow problems, but the general-purpose codes used for nozzle simulations and other realistic configurations usually employ computationally cheaper eddy viscosity models. Eddy viscosity models use the Boussinesq approximation to calculate the Reynolds stress as the product of an eddy viscosity and the rate-of-strain tensor. These models vary in complexity from algebraic (also termed zero-equation) formulations to more complex formulations which solve additional transport equations (normally one or two partial differential equations).

Algebraic models typically use a form of Prandtl's mixing length hypothesis to calculate the eddy (or turbulent) viscosity, but are usually optimized for a single flow and are not accurate for a wide range of flows. One of the first widely used algebraic models was developed by Cebeci and Smith [18,19]. Another widely used

algebraic model is that due to Baldwin and Lomax [4]. Both the Cebeci-Smith and Baldwin-Lomax models are formulated only for the calculation of wall boundary layers and have been used successfully for calculations of flows without adverse pressure gradients or separation regions.

One-equation models offer, to some degree, more generality than algebraic models, because they solve for a quantity such as the turbulent kinetic energy or the turbulent viscosity. However, they frequently have the limitation of not solving a transport equation for the turbulent length scale. Two of the more widely used one-equation models are the Baldwin-Barth [3] and Spalart-Allmaras [98] models. While one-equation models have shown promise for turbulent wall bounded flows at a lower computational cost than algebraic models, they have not been shown to be accurate for flows with significant turbulent mixing, which is of primary importance to the nozzle problems discussed here.

Two-equation turbulence models usually solve one equation for the turbulent kinetic energy and a second equation from which the turbulent length scale can be obtained. The most popular of these are $k-\epsilon$ models, that solve one transport equation for the turbulent kinetic energy, k , and the second for the rate of turbulent kinetic energy dissipation, ϵ . Probably the one $k-\epsilon$ turbulence model that has served as the basis of most other $k-\epsilon$ models (and itself is still in wide use) is that due to Jones and Launder [47]. Also referred to as the “standard” $k-\epsilon$ model, the Jones-Launder model has one form that may be directly integrated down to solid surfaces including the laminar sublayer, through the use of damping terms, and a second form that requires the use of a wall function to bridge the gap from the fully

turbulent region of a boundary layer to the laminar sublayer very near the wall. The former is referred to as the “low Reynolds number” form while the latter is referred to as the “high Reynolds number” or “wall-function” form. Both have the same formulation away from walls and in mixing layers.

Although $k-\epsilon$ models are generally more accurate than the simpler algebraic or one-equation models, they have several limitations. For wall bounded flows, $k-\epsilon$ models are particularly deficient in regions of strong adverse pressure gradients and in separation zones (Rodi and Scheuerer [84]). For high-speed flows involving mixing of multiple streams, such as those in the nozzle and jet flows described previously, standard $k-\epsilon$ models deviate substantially from experimental data for highly compressible shear layers and for round jets.

Several new $k-\epsilon$ models have been developed beyond the standard Jones-Launder model to address pressure gradient and separated boundary layer problems, but have not demonstrated wide spread improvement over the Jones-Launder formulation. To address the compressibility issue, several modifications have been proposed. Most of these modify the equation for dissipation rate, ϵ , so as to account for the experimentally observed reduction in turbulent kinetic energy production with the relative speed of streams (frequently referred to as the convective Mach number) that form compressible shear layers. The mostly widely used are those of Sarkar [88,89] and Zeman [115].

Experimental data have also indicated that round (or axisymmetric) jets mix less rapidly than planar jets. Because the empirical coefficients of most $k-\epsilon$ models,

including Jones-Launder, have been calibrated against incompressible planar shear layers, corrections have been developed to improve the capability of $k-\epsilon$ models to calculate round jets. The most widely used of these is that due to Pope [79], which like the compressibility corrections of Sarkar and Zeman, modifies the dissipation rate equation. Essentially, the Pope correction increases the dissipation rate of turbulent kinetic energy in the presence of vortex stretching, which is characteristic of round jets. Finally, one recently developed $k-\epsilon$ model, due to Thies and Tam [102], substantially modified the empirical coefficients from those of the standard $k-\epsilon$ model, and included the Sarkar compressibility correction and Pope round jet correction intended for turbulent jets with flow conditions similar to those found in the exhaust nozzles of high speed aircraft. The Tam-Thies model, with its substantially modified coefficients, has only been calibrated for mixing layers using calculations beginning downstream of any nozzle surfaces. As a result, some other method is required to accurately calculate the wall boundary layer regions upstream of the mixing layer.

Despite some of the aforementioned limitations of $k-\epsilon$ models and the necessity of empirically based corrections to handle specific flow complexities, $k-\epsilon$ models are still the most frequently used models for calculating nozzle and jet flow fields. This is because more complex models, such as Reynolds stress closures, have not demonstrated significant accuracy improvements that would warrant their much more computationally expensive use. As a result, several validation studies have been conducted to determine the accuracy of $k-\epsilon$ models for specific classes of nozzle and jet problems. Some recent examples of such validation studies are provided in

references [5, 6, 22, 31, 75, 106]. Nearly all of the flows investigated have operating conditions (velocities and temperatures) similar to those of real configurations, but the geometries were simpler to allow comprehensive studies of different models and corrections to be conducted.

Two other popular two-equation models will be briefly discussed here. The $k-\omega$ model is another two-equation turbulence model which is similar in form to the $k-\epsilon$ model. The second transport equation of this model solves for the dissipation rate per unit turbulent kinetic energy. The most widely used $k-\omega$ in current use is that due to Wilcox [113]. The $k-\omega$ model has demonstrated improved capability to handle adverse pressure gradient boundary layers relative to the $k-\epsilon$ model. However, it has been shown to be worse than $k-\epsilon$ in predicting free shear layer mixing, and demonstrates significant sensitivity to freestream turbulence levels. Wilcox [114] extended his original model in a new formulation to address these limitations. The last two-equation model discussed here is the Shear Stress Transport Model (SST) of Menter [66, 67]. Menter's model employs a $k-\omega$ formulation in regions near solid boundaries and a $k-\epsilon$ formulation away from walls. This model has become popular in recent years because it used the $k-\omega$ and $k-\epsilon$ formulations in the regions where each performs the best.

The most recent adaptation of a Reynolds-averaged Navier-Stokes approach has been in the emerging field of computational aeroacoustics to address the problem of developing quieter aircraft engine exhaust nozzles. One procedure is to use the solution from a turbulent CFD simulation of a jet flow field (using a $k-\epsilon$ model) as input into an acoustic prediction method. The jet noise field is then determined by

integration of the sound propagation equations. References [50, 51] present some recent aeroacoustic calculations of convergent-divergent nozzles having flow characteristics again representative of realistic high speed nozzles. In computational aeroacoustics, which has its own set of limitations related to the acoustic modeling methods, the input is also limited by the quality of the aerodynamic flow field. As with the nozzle and jet aerodynamic prediction methods, significant work is being performed to improve the accuracy of acoustic prediction techniques [56].

1.2 LES Methods

Although LES techniques have been used in selective applications, such as meteorology and atmospheric sciences [83] for several years, only recently has LES been considered as a potential tool for nozzle and jet flow problems. Much of the foundation of LES was established in the meteorology field by Smagorinsky [94], Lilly [58], and Deardorff [25] near the end of the 1960's. Reference [69] mentions that after some interest in LES by the United States engineering community in the early 1970's, the 1980's saw only limited development and application. Recently, however, the realization of the shortcomings of RANS, and improvement in computer speeds have sparked new interest in LES for engineering applications.

Several recent U.S. aeronautics research and development programs have sponsored research in developing and applying LES based techniques for analyzing jet flows. Of particular interest to the these programs is the potential of LES as a computational aeroacoustic technique for enabling accurate predictions of jet noise. In reference [65], Mankbadi et al. discusses that large scale turbulent structures are

believed to be the dominant noise producing mechanisms in free jet flows. Choi et al. [20] have used an LES technique to calculate the aerodynamic field of a Mach 1.4 axisymmetric jet and then employed a Kirchoff method, detailed in references [60] and [92], to calculate the noise field. Since LES reserves modeling for the smallest turbulent length and time scales while directly solving for the large scales, it is thought to be appropriate for application to certain classes of jet noise problems. In particular, success is being realized for jet problems in which the flow regions of interest are far removed from solid boundaries, such as relatively simple single flow nozzles exiting into ambient air. LES methods are not yet prepared to handle more complex configurations, like those of the multiple stream nozzles discussed previously. Such configurations, if they contain turbulent boundary layers along solid surfaces, have a large range of turbulent scales that are important to the overall flow problem, and at this point, the cut-off scale at which direct solution ends and modeling begins is one of the major unresolved issues of LES.

A brief review of the fundamental steps of LES is as follows, more details of the process will be given in chapter 2. A filtering process removes the smallest spatial scales of the Navier-Stokes equations. A set of equations is produced that represents the spatial and time evolution of the larger turbulent scales, but contains a subgrid scale tensor to account for the unresolved smallest scales that were removed by the filtering process. Next, the subgrid scale stress is replaced by a model (appropriately termed a subgrid scale model), which is analogous to the eddy viscosity models described in the last section for Reynolds-averaged Navier-Stokes codes. Using the subgrid scale model to handle the small scale structures ranging

from the Kolmogorov scale up to the cut-off scale, the large scale equations are then solved using a time-accurate algorithm.

The features of the subgrid scale model has been one of the most heavily researched aspects of LES. The most commonly used subgrid scale model is the Smagorinsky eddy viscosity model [94]. One of the primary reasons for the popularity of the Smagorinsky model is that it provides sufficient diffusion and dissipation to keep an LES computation stable. Because of the importance of the subgrid scale model in allowing for the correct transfer of turbulent energy between the large scales (which are directly solved) and the modeled subgrid scales, several modifications to the Smagorinsky model have been proposed. The most popular of these are known as dynamic eddy-viscosity models [26,33,77] which replace the model constant of the Smagorinsky model with a coefficient that is allowed to vary both spatially and temporally as a calculation progresses. The major advantage of the dynamic eddy-viscosity models over the Smagorinsky model is the improved capability of the dynamic eddy-viscosity models to provide the correct turbulent kinetic energy dissipation. As with the turbulence models for Reynolds-averaged Navier-Stokes codes, however, no single subgrid-scale model has been found to work well for all flows. Nelson [70] and Vreman [107,108] have investigated the effects of subgrid-scale model selection on LES calculations of compressible planar shear layers.

There are other issues related to LES that will require significant work to make LES an appropriate tool for engineering applications, and in particular for the nozzle and jet flows that are the subject of this report. Since LES directly solves for the largest scales of turbulent motion, a highly accurate solver is necessary for the

time-marching procedure. References [39, 55, 68] discuss higher order schemes as applied to LES. Compact finite difference schemes, introduced by Lele in reference [55], are particularly promising for LES calculations because they are available to accurately resolve a greater range of scales than other finite difference schemes. Several LES algorithms are using (MacCormack-type) explicit schemes, which lend themselves well to calculations distributed over parallel processors (see references [10] and [93]). Boundary conditions provide some of the most challenging modeling uncertainties for LES. Many LES simulations of simple geometry benchmark cases, such as fully-developed channel flow, have used periodic boundary conditions for the computational inflow and exit. For jet flows, however, such a boundary condition cannot be used, because of the fundamentally different nature of the inflow and outflow stations.

Nearly all LES simulations of jet and mixing layer flows performed to date have placed the inflow of the computational domain downstream of any wall bounded regions and have either ignored the upstream boundary layer effects or used some approximation to initialize the turbulent mixing layer. Several authors, such as Ragab [81, 82] and Hedges [38] have imposed hyperbolic tangent mean velocity profiles at the plane which represents the end of the wall boundary layer regions and the beginning of the mixing region. Ragab then used the results of a linear stability analysis to generate perturbations about the mean velocity profile located at the mixing plane. Hedges added small amplitude perturbations to the vertical velocity component in simulations of heated jet flows.

The difficulty in using an artificially generated inflow, such as that assuming a hyperbolic tangent velocity profile, is that the characteristics of the upstream turbulent boundary layers, including velocity, temperature, and turbulence profiles, are not accurately represented. This is a significant deficiency since the state of the incoming boundary layers have been shown to have significant effects on the development of turbulent mixing layers in the experiments conducted by Bradshaw [13], Browand and Latigo [15], and Hussain and Clark [44].

Recently, Li et al. [57] proposed a method in which parallel calculations of the upstream boundary layers are used to generate time-varying inflow conditions for a spatially developing mixing layer. This method offers a promising technique for reducing the computational cost relative to performing a complete LES calculation containing both the wall-bounded and mixing regions, but itself is probably too expensive to use in the near future for high speed, high Reynolds number cases. The hybrid RANS-LES method developed in this work is proposed as an alternative computational technique to performing LES calculations everywhere in the computational domain, that includes the mean flow characteristics of the incoming boundary layers and is also feasible when considering foreseeable computational resources.

1.3 Hybrid RANS-LES Methods

The realization that LES calculations of flows in aerospace and industrial applications at realistic Reynolds numbers will not be possible for some time has led to interest into the development of hybrid techniques. The objective of a hybrid

method is to retain the essential features of the LES method, but to employ a computationally cheaper RANS method in regions where it is appropriate. As a result, nearly all hybrid methods proposed to date apply a RANS approach to attached wall boundary layer regions and an LES approach to regions of large scale separation. The work detailed in this dissertation represents the first hybrid method development for application to compressible mixing layers.

The most widely publicized hybrid method to date is the Detached Eddy Simulation (DES) method of Spalart [96, 97, 99]. In the DES method, the wall bounded regions are calculated using RANS with the Spalart-Allmaras [98] one equation turbulence model. Constantinescu and Squires [23] have applied Spalart's DES method to turbulent flow over a sphere, which is an appropriate geometry for the method due to the large scale separation in the wake of the sphere.

Speziale [100] suggested an approach that allows for computations varying from RANS in the coarse grid limit, through LES, and finally to DNS in the very fine grid limit. A Reynolds Stress model is used to close the turbulent stresses in the RANS limit, and provides the basis for a subgrid model necessary in LES simulations. Batten et al. [7] also propose a hybrid model that employs a Reynolds-Stress model to close the RANS and LES equations. Lastly, Arunajatesan et al. [1] have applied a hybrid RANS-LES method to cavity flowfields. Their approach employed a two-equation $k-k_l$ turbulence model to close the RANS equations and a one-equation model solving for the filtered subgrid kinetic energy to close the LES equations.

1.4 Overview and Objectives of the Current Work

The hybrid RANS-LES method presented in this dissertation is developed for application to configurations such as the mixing layer shown in figure 1.1. This relatively simple configuration is representative of the more complex nozzle geometries discussed at the beginning of this chapter, in that two wall bounded regions provide isolated flows to a single region where compressible mixing is the primary flow characteristic. Development of the hybrid method and assessment of the method for a benchmark compressible mixing layer configuration are the focus of the dissertation.

The hybrid method employs a RANS approach to provide the mean flow characteristics of the wall boundary layers entering the mixing region. The downstream mixing layer is then calculated using LES. The method developed here is intended for those nozzle and mixing layer problems in which a dominant geometric feature, such as the base region of a nozzle or splitter plate separating the upstream flows, will provide an unsteady mechanism to drive the turbulent development in the mixing layer which will dominate unsteady effects from the incoming turbulent wall boundary layers. Although the upstream RANS approach does not provide any unsteady turbulent information to the mixing layer, the mean flow momentum and thermal boundary layer effects can be provided.

1.5 Outline of the Dissertation

The equation sets which must be solved for the RANS and LES regions are derived from the general form of the compressible Navier-Stokes equations in chapter 2. The

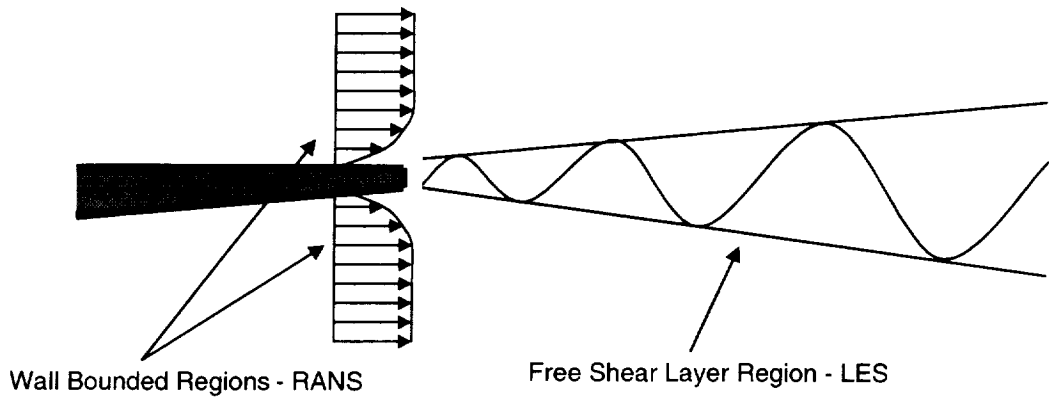


Figure 1.1: Schematic of mixing layer demonstrating the hybrid RANS/LES approach.

turbulence model used to close the RANS equations and the subgrid scale model needed to close the LES equations are also presented. Chapter 3 provides details of the numerical procedure used to perform the hybrid RANS-LES computations. Validation of the RANS method for a series of flat plate boundary layer cases is presented in chapter 4. These cases include an incompressible laminar boundary layer, an incompressible turbulent boundary layer, and finally two supersonic boundary layers which have the same flow conditions as the two streams entering

the compressible mixing layer that is the focus of this work. The hybrid RANS-LES method is investigated for the compressible mixing layer in chapters 5 and 6.

Although true LES simulations require calculations in three spatial directions, two-dimensional calculations are examined first in chapter 5 to investigate effects of grid resolution and boundary conditions. Three dimensional calculations are examined next in chapter 6 with emphasis placed on comparison to experimental data, and to parametric studies of subgrid scale model and grid resolution effects. The importance of using three dimensional calculations to capture the initial development of the turbulent mixing layer is also investigated. Conclusions of the hybrid RANS-LES method development and benchmark computations as well as recommendations for further research are presented in chapter 7.

CHAPTER 2

FORMULATION OF THE RANS AND LES EQUATIONS

In this chapter, the equations that are used to solve the flow in the RANS and LES regions are derived. The general form of the Navier-Stokes equations, written in tensor notation, is presented first. Next, the RANS equations are derived using the mass-weighted form of the Reynolds-averaging process and the LES equations are derived using a mass-weighted spatial filtering process. Turbulence modeling for the RANS and LES equations is presented in the last section of the chapter.

2.1 Navier-Stokes Equations of Motion

The Navier-Stokes equations represent the time-dependent, three-dimensional motion of a fluid. They consist of expressions for the conservation of mass, momentum, and energy.

The expression for conservation of mass, or the continuity equation is written in tensor form as:

$$\frac{\partial \rho}{\partial t} + \frac{\partial}{\partial x_i} (\rho u_i) = 0 \quad (2.1)$$

Conservation of momentum is written:

$$\frac{\partial}{\partial t}(\rho u_i) + \frac{\partial}{\partial x_j}(\rho u_i u_j) = -\frac{\partial P}{\partial x_i} + \frac{\partial \tau_{ij}}{\partial x_j} \quad (2.2)$$

Conservation of energy is expressed as follows:

$$\frac{\partial E_t}{\partial t} + \frac{\partial}{\partial x_j}(u_j(E_t + P)) = \frac{\partial}{\partial x_j}(u_i \tau_{ij}) - \frac{\partial q_j}{\partial x_j} \quad (2.3)$$

Here, the variable E_t represents the total energy (internal energy plus kinetic energy) per unit volume:

$$E_t = \rho \epsilon + \frac{1}{2} \rho u_i u_i \quad (2.4)$$

The equation of state for an ideal gas is used to relate the pressure, temperature, and density through:

$$P = \rho R T \quad (2.5)$$

For the viscous stresses τ_{ij} , it is assumed that the fluid is a Newtonian fluid, and as a result, the viscous stress is proportional to the rate of strain. This is written:

$$\tau_{ij} = 2\mu S_{ij} + \lambda \frac{\partial u_j}{\partial x_i} \delta_{ij} \quad (2.6)$$

where the rate of strain tensor S_{ij} is:

$$S_{ij} = \frac{1}{2} \left(\frac{\partial u_i}{\partial x_j} + \frac{\partial u_j}{\partial x_i} \right) \quad (2.7)$$

Using Stokes's assumption that the thermodynamic and mechanical pressures are the same for a fluid undergoing and expansion or compression:

$$\lambda = -\frac{2}{3}\mu \quad (2.8)$$

Equation (2.6) can then be rewritten as:

$$\tau_{ij} = 2\mu S_{ij} - \frac{2}{3}\mu \frac{\partial u_j}{\partial x_j} \delta_{ij} \quad (2.9)$$

To calculate the viscosity, the Sutherland model is used which assumes that the viscosity is only a function of temperature for a gas:

$$\mu = \frac{C_1 T^{\frac{3}{2}}}{C_2 + T} \quad (2.10)$$

For air, the values of the constants C_1 and C_2 are (in SI units):

$$C_1 = 1.458 \times 10^{-6} \frac{kg}{m \cdot s \cdot K^{\frac{1}{2}}} \quad (2.11)$$

$$C_2 = 110.4 K$$

The heat flux q_j is obtained from Fourier's law:

$$q_j = -k \frac{\partial T}{\partial x_j} \quad (2.12)$$

where k is the thermal conductivity. It is assumed that the fluid is thermally perfect, such that the internal energy and enthalpy are only functions of the temperature, and it is also assumed that the fluid is calorically perfect such that the

specific heats C_V and C_P are constants. As a result, the internal energy and enthalpy can be written as:

$$\begin{aligned} e &= C_V T \\ h &= C_P T \end{aligned} \quad (2.13)$$

Assuming that the air is of constant composition and does not undergo any chemical reaction, the thermal conductivity is only a function of temperature. Using the specification of constant specific heats, the following expression is obtained for the thermal conductivity as a function of the constant pressure specific heat, Prandtl number, and the viscosity defined in equation (2.10):

$$k = \frac{\mu C_P}{Pr} \quad (2.14)$$

2.2 Mass-Weighted RANS Equations

In the classical form of Reynolds averaging, the time dependent form of the Navier-Stokes equations given by (2.1) through (2.3) are averaged over a period of time that is much larger than the period of turbulent fluctuations. Each of the dependent variables appearing in these equations is replaced by the sum of mean and fluctuating components. As an example, the velocity would be given by:

$$u_i = \bar{u}_i + u'_i \quad (2.15)$$

where the time averaged velocity \bar{u}_i is given by:

$$\bar{u}_i = \frac{1}{\tau} \int_t^{t+\tau} u_i dt \quad (2.16)$$

For the current work, where fluctuations in density are important, a mass (or density) weighting is employed in the averaging process, which will make the final form of the RANS equations much more convenient to work with. The dependent variables are again broken into mean and fluctuating components:

$$u_i = \hat{u}_i + u''_i \quad (2.17)$$

where the time averaged (using mass weighting) velocity \hat{u}_i is given by:

$$\hat{u}_i = \frac{1}{\bar{\rho}\tau} \int_t^{t+\tau} \rho u_i dt \quad (2.18)$$

This mass-weighted Reynolds averaging process is frequently referred to as Favre averaging, and in general, the Favre average of any variable f is defined by:

$$\hat{f} = \frac{\overline{\rho f}}{\bar{\rho}} \quad (2.19)$$

Before averaging the Navier-Stokes equations (2.1 - 2.3) the flow variables are separated into mean and fluctuating components:

$$\rho = \bar{\rho} + \rho'$$

$$P = \bar{P} + P'$$

$$u_i = \hat{u}_i + u''_i$$

$$\epsilon = \hat{\epsilon} + \epsilon'' \quad (2.20)$$

$$h = \hat{h} + h''$$

$$T = \hat{T} + T''$$

$$q_i = \bar{q}_i + q'_i$$

Note that the density, pressure, and heat flux are not decomposed using mass weighted variables. Starting with the continuity expression (2.1), a time averaging is performed to obtain:

$$\frac{\partial \bar{\rho}}{\partial t} + \frac{\partial}{\partial x_i} (\bar{\rho} \bar{u}_i) = 0 \quad (2.21)$$

Using the definition of mass weighted variables, this can be rewritten as:

$$\frac{\partial \bar{\rho}}{\partial t} + \frac{\partial}{\partial x_i} (\bar{\rho} \hat{u}_i) = 0 \quad (2.22)$$

Working next with the momentum equation (2.2), a time average of the entire equation is performed, resulting in:

$$\frac{\partial}{\partial t} (\bar{\rho} \bar{u}_i) + \frac{\partial}{\partial x_j} (\bar{\rho} \bar{u}_i \bar{u}_j) = - \frac{\partial \bar{P}}{\partial x_i} + \frac{\partial \bar{\tau}_{ij}}{\partial x_j} \quad (2.23)$$

In equation (2.23), the time dependent term is rewritten in terms of mass averaged variables as:

$$\frac{\partial}{\partial t} (\overline{\rho u_i}) = \frac{\partial}{\partial t} (\overline{\rho \hat{u}_i}) \quad (2.24)$$

The convective term is expanded as:

$$\begin{aligned} \frac{\partial}{\partial x_j} (\overline{\rho u_i u_j}) &= \frac{\partial}{\partial x_j} \left(\overline{\rho (\hat{u}_i + u''_i) (\hat{u}_j + u''_j)} \right) \\ &= \frac{\partial}{\partial x_j} (\overline{\rho \hat{u}_i \hat{u}_j}) + \frac{\partial}{\partial x_j} (\overline{\rho \hat{u}_i u''_j}) + \frac{\partial}{\partial x_j} (\overline{\rho u''_j \hat{u}_i}) + \frac{\partial}{\partial x_j} (\overline{\rho u''_i u''_j}) \end{aligned} \quad (2.25)$$

The first term in the expansion of (2.25) is rewritten as:

$$\frac{\partial}{\partial x_j} (\overline{\rho \hat{u}_i \hat{u}_j}) = \frac{\partial}{\partial x_j} (\overline{\rho \hat{u}_i \hat{u}_j}) \quad (2.26)$$

Over the period of the time averaging, the the mass weighted variables denoted with a hat are constant. As a result:

$$\frac{\partial}{\partial x_j} (\overline{\rho \hat{u}_i u''_j}) = \frac{\partial}{\partial x_j} (\overline{\rho u''_j \hat{u}_i}) = 0 \quad (2.27)$$

The last term in equation (2.25) is the turbulent or Reynolds stress, and is the term from the momentum equation that is replaced with a turbulence model:

$$\frac{\partial}{\partial x_j} (\overline{\rho u''_i u''_j}) = -\frac{\partial \tau_{ij}^T}{\partial x_j} \quad (2.28)$$

Replacing the terms in equation (2.23) with those in equations (2.24) through (2.28), the resulting RANS momentum equation written in terms of mass averaged variables is:

$$\frac{\partial}{\partial t} (\bar{\rho} \hat{u}_i) + \frac{\partial}{\partial x_j} (\bar{\rho} \hat{u}_i \hat{u}_j) = - \frac{\partial \bar{P}}{\partial x_i} + \frac{\partial \bar{\tau}_{ij}}{\partial x_j} + \frac{\partial \tau_{ij}^T}{\partial x_j} \quad (2.29)$$

To obtain the time averaged energy equation written in mass averaged variables, the total energy terms in equation (2.3) are replaced with the expanded energy expression shown in (2.4) and then the entire equation is time averaged:

$$\frac{\partial}{\partial t} \left(\overline{\rho \epsilon + \frac{1}{2} \rho u_i u_i} \right) + \frac{\partial}{\partial x_j} \left(\overline{u_j (\rho \epsilon + \frac{1}{2} \rho u_i u_i + P)} \right) = \frac{\partial}{\partial x_j} (\overline{u_i \tau_{ij}}) - \frac{\partial \bar{q}_j}{\partial x_j} \quad (2.30)$$

Working first with the time dependent term, this term is expanded in terms of mean plus fluctuating velocities as:

$$\frac{\partial}{\partial t} \left(\overline{\rho \epsilon + \frac{1}{2} \rho u_i u_i} \right) = \frac{\partial}{\partial t} (\bar{\rho} \hat{\epsilon}) + \frac{\partial}{\partial t} \left(\overline{\frac{1}{2} \rho (\hat{u}_i + u''_i) (\hat{u}_i + u''_i)} \right) \quad (2.31)$$

The kinetic energy term is further expanded as:

$$\frac{\partial}{\partial t} \left(\overline{\frac{1}{2} \rho (\hat{u}_i + u''_i) (\hat{u}_i + u''_i)} \right) = \frac{\partial}{\partial t} \left(\overline{\frac{1}{2} \rho \hat{u}_i \hat{u}_i} \right) + \frac{\partial}{\partial t} \left(\overline{\frac{1}{2} \rho \hat{u}_i u''_i} \right) + \frac{\partial}{\partial t} \left(\overline{\frac{1}{2} \rho u''_i u''_i} \right) \quad (2.32)$$

The the first term on the right side of equation (2.32) is rewritten as:

$$\frac{\partial}{\partial t} \left(\overline{\frac{1}{2} \rho \hat{u}_i \hat{u}_i} \right) = \frac{\partial}{\partial t} \left(\overline{\frac{1}{2} \bar{\rho} \hat{u}_i \hat{u}_i} \right) \quad (2.33)$$

Over the period of the time averaging, the mass weighted variables are treated as constants and as a result, the second term on the right side of equation (2.32) is zero:

$$\frac{\partial}{\partial t} \left(\frac{1}{2} \rho \hat{u}_i \hat{u}_i'' \right) = 0 \quad (2.34)$$

The last term is the turbulent kinetic energy and is written as:

$$\frac{\partial}{\partial t} \left(\frac{1}{2} \rho \hat{u}_i'' \hat{u}_i'' \right) = \frac{\partial}{\partial t} \left(\bar{\rho} \hat{k} \right) \quad (2.35)$$

The resulting time dependent term is:

$$\frac{\partial}{\partial t} \left(\bar{\rho} \epsilon + \frac{1}{2} \rho \hat{u}_i \hat{u}_i \right) = \frac{\partial}{\partial t} \left(\bar{\rho} \hat{\epsilon} + \frac{1}{2} \bar{\rho} \hat{u}_i \hat{u}_i + \bar{\rho} \hat{k} \right) \quad (2.36)$$

Working next with the convective term, $h = \epsilon + P/\rho$ is used to obtain:

$$\frac{\partial}{\partial x_j} \left(\bar{u}_j \left(\rho \epsilon + \frac{1}{2} \rho \hat{u}_i \hat{u}_i + P \right) \right) = \frac{\partial}{\partial x_j} \left(\bar{u}_j \left(\rho h + \frac{1}{2} \rho \hat{u}_i \hat{u}_i \right) \right) \quad (2.37)$$

Expanding this expression in terms of mean plus fluctuating velocities as:

$$\begin{aligned} \frac{\partial}{\partial x_j} \left(\bar{u}_j \left(\rho h + \frac{1}{2} \rho \hat{u}_i \hat{u}_i \right) \right) &= \frac{\partial}{\partial x_j} \left(\bar{\rho} \left(\hat{u}_j + u_j'' \right) \left(\hat{h} + h'' \right) \right) \\ &+ \frac{\partial}{\partial x_j} \left(\frac{1}{2} \rho \left(\hat{u}_j + u_j'' \right) \left(\hat{u}_i + u_i'' \right) \left(\hat{u}_i + u_i'' \right) \right) \end{aligned} \quad (2.38)$$

Working first with the enthalpy expression:

$$\begin{aligned} \frac{\partial}{\partial x_j} \left(\bar{\rho} \left(\hat{u}_j + u_j'' \right) \left(\hat{h} + h'' \right) \right) &= \frac{\partial}{\partial x_j} \left(\bar{\rho} \hat{u}_j \hat{h} \right) + \frac{\partial}{\partial x_j} \left(\bar{\rho} \hat{u}_j h'' \right) \\ &+ \frac{\partial}{\partial x_j} \left(\bar{\rho} u_j'' \hat{h} \right) + \frac{\partial}{\partial x_j} \left(\bar{\rho} u_j'' h'' \right) \end{aligned} \quad (2.39)$$

The second and third terms on the right side of equation (2.39) are zero by the same argument as that for (2.34). The last term contains the turbulent heat flux and is rewritten as:

$$\frac{\partial}{\partial x_j} (\overline{\rho u_j'' h''}) = \frac{\partial q_j^T}{\partial x_j} \quad (2.40)$$

This turbulent heat flux must be modeled, and is done so in a manner similar to that for the Reynolds stress appearing in the momentum equation (2.28).

Working next with the second term on the right side of equation (2.38):

$$\begin{aligned} \frac{\partial}{\partial x_j} \left(\frac{1}{2} \rho \overline{(\hat{u}_j + u_j'') (\hat{u}_i + u_i'') (\hat{u}_i + u_i'')} \right) &= \frac{\partial}{\partial x_j} \left(\frac{1}{2} \overline{\rho \hat{u}_j \hat{u}_i \hat{u}_i} \right) \\ &+ \frac{\partial}{\partial x_j} \left(\overline{\rho \hat{u}_j \hat{u}_i u_i''} \right) + \frac{\partial}{\partial x_j} \left(\frac{1}{2} \overline{\rho \hat{u}_j u_i'' u_i''} \right) + \frac{\partial}{\partial x_j} \left(\frac{1}{2} \overline{\rho u_j'' \hat{u}_i \hat{u}_i} \right) \\ &+ \frac{\partial}{\partial x_j} \left(\overline{\rho u_j'' \hat{u}_i u_i''} \right) + \frac{\partial}{\partial x_j} \left(\frac{1}{2} \overline{\rho u_j'' u_i'' u_i''} \right) \end{aligned} \quad (2.41)$$

The second and fourth terms on the right side of equation (2.41) are zero over the period of the time average. The third term includes the turbulent kinetic energy as defined in equation (2.35) and is rewritten:

$$\frac{\partial}{\partial x_j} \left(\frac{1}{2} \overline{\rho \hat{u}_j u_i'' u_i''} \right) = \frac{\partial}{\partial x_j} \overline{\rho \hat{u}_j \hat{k}} \quad (2.42)$$

The fifth term includes the turbulent Reynolds stress as defined in equation (2.28) and is rewritten:

$$\frac{\partial}{\partial x_j} \left(\overline{\rho u_j'' \hat{u}_i u_i''} \right) = - \frac{\partial}{\partial x_j} \left(\hat{u}_i \tau_{ij}^T \right) \quad (2.43)$$

The resulting convective term is:

$$\begin{aligned} \frac{\partial}{\partial x_j} \left(\overline{u_j (\rho h + \frac{1}{2} \rho u_i u_i)} \right) &= \frac{\partial}{\partial x_j} (\overline{\rho \hat{u}_j \hat{h}}) + \frac{\partial q_j^T}{\partial x_j} \\ &+ \frac{\partial}{\partial x_j} \left(\frac{1}{2} \overline{\rho \hat{u}_j \hat{u}_i \hat{u}_i} \right) + \frac{\partial}{\partial x_j} \overline{\rho \hat{u}_j \hat{k}} - \frac{\partial}{\partial x_j} \left(\hat{u}_i \overline{\tau_{ij}^T} \right) + \frac{\partial}{\partial x_j} \left(\frac{1}{2} \overline{\rho u_j'' u_i'' u_i''} \right) \end{aligned} \quad (2.44)$$

The viscous dissipation term on the right side of equation (2.30) is examined next.

After expansion, this term becomes:

$$\begin{aligned} \frac{\partial}{\partial x_j} (\overline{u_i \tau_{ij}}) &= \frac{\partial}{\partial x_j} \left((\hat{u}_i + u_i'') (\overline{\tau_{ij}} + \tau_{ij}') \right) \\ &= \frac{\partial}{\partial x_j} (\hat{u}_i \overline{\tau_{ij}}) + \frac{\partial}{\partial x_j} (\overline{u_i'' \tau_{ij}}) \end{aligned} \quad (2.45)$$

The heat flux term is left as it appears in equation (2.30). Rewriting the energy equation (2.30) with the terms we obtained in equations (2.36), (2.44), and (2.45) results in:

$$\begin{aligned} \frac{\partial}{\partial t} (\overline{\rho \hat{\epsilon}} + \frac{1}{2} \overline{\rho \hat{u}_i \hat{u}_i} + \overline{\rho \hat{k}}) + \frac{\partial}{\partial x_j} (\overline{\rho \hat{u}_j \hat{h}} + \frac{1}{2} \overline{\rho \hat{u}_j \hat{u}_i \hat{u}_i} + \overline{\rho \hat{u}_j \hat{k}}) \\ = \frac{\partial}{\partial x_j} (\hat{u}_i \overline{\tau_{ij}} + \hat{u}_i \overline{\tau_{ij}^T} + \overline{u_i'' \tau_{ij}}) - \frac{\partial}{\partial x_j} \left(\overline{q_j} + q_j^T + \frac{1}{2} \overline{\rho u_j'' u_i'' u_i''} \right) \end{aligned} \quad (2.46)$$

In order to simplify this expression to the form that will be used in the computations, the terms involving the turbulent kinetic energy and those with the fluctuating velocity u_i'' are assumed to be small compared to the other terms in the energy equation. The enthalpy in the convective term is first expanded using $\overline{\rho \hat{h}} = \overline{\rho \hat{\epsilon}} + \overline{P}$. Equation (2.4) is then used to rewrite the sum of the internal and mean flow kinetic energy, appearing in both the time-dependent and convective terms, as the total energy:

$$\hat{E}_t = \bar{\rho}\hat{e} + \frac{1}{2}\bar{\rho}\hat{u}_i\hat{u}_i \quad (2.47)$$

The resulting final form of the RANS energy equation is:

$$\frac{\partial}{\partial t}(\hat{E}_t) + \frac{\partial}{\partial x_j}(\hat{u}_j\hat{E}_t + \hat{u}_j\bar{P}) = \frac{\partial}{\partial x_j}(\hat{u}_i\bar{\tau}_{ij} + \hat{u}_i\tau_{ij}^T) - \frac{\partial}{\partial x_j}(\bar{q}_j + q_j^T) \quad (2.48)$$

2.3 Spatially Filtered LES Equations

To derive the LES equations used in this work, the time dependent form of the Navier-Stokes equations given in equations (2.1) through (2.3) is used as the starting point. Instead of time averaging these equations, however, an approach similar to the work of Ragab and Sheen [81,82] and Erlebacher et al [27] is used that will filter out small scale fluctuations, and only retain scales that are large enough to be resolved by a particular computational scheme and the computational mesh. The filtering operation is defined on any variable f by the expression:

$$\bar{f}(\mathbf{x}, t) = \int_D G(\mathbf{x} - \boldsymbol{\xi}, \Delta) f(\boldsymbol{\xi}, t) d^3\boldsymbol{\xi} \quad (2.49)$$

In equation (2.49), G is the filter function, D is the flow domain, and Δ is the filter width. The filter width Δ is usually taken to be the grid spacing, and is the approach taken here. Note that the overbar used in equation (2.49) indicates a filtered variable. This is in contrast to the previous use of an overbar to indicate a time averaged quantity in the previous section.

As discussed in [71], the exact form of the filter function is not typically known.

However, the filter function must satisfy:

$$\int_D G(\mathbf{x} - \boldsymbol{\xi}, \Delta) d^3 \boldsymbol{\xi} = 1 \quad (2.50)$$

In addition, the form of the function G allows the operations of filtering and differentiation to commute such that:

$$\overline{\frac{\partial f}{\partial t}} = \frac{\partial \overline{f}}{\partial t} \quad (2.51)$$

and

$$\overline{\frac{\partial f}{\partial x_j}} = \frac{\partial \overline{f}}{\partial x_j} \quad (2.52)$$

In large eddy simulations of compressible flows, it is common to use Favre-filtering which is defined as:

$$\tilde{f} = \frac{\overline{\rho f}}{\overline{\rho}} \quad (2.53)$$

where a quantity f is decomposed into resolved and unresolved (also referred to as sub-grid scale) components as:

$$f = \tilde{f} + f' \quad (2.54)$$

Equations (2.53) and (2.19) are very similar in appearance, but they refer to very different operations. Both operations employ mass (density) weighting, but equation

(2.19) defines a time averaged quantity, while equation (2.53) defines a spatially filtered quantity. As was the case for the RANS equations, the density, pressure, and heat flux terms are not decomposed using mass-weighting. Again note that the overline represented a time averaging process in the previous section, but it will refer to a spatial filtering operation in the current section. In addition, Favre filtering differs from Favre time averaging in that:

$$\tilde{f} \neq \hat{f} \quad (2.55)$$

and

$$\tilde{f}' \neq 0 \quad (2.56)$$

Applying the filtering operation to the continuity expression (2.1) results in:

$$\frac{\partial \bar{\rho}}{\partial t} + \frac{\partial}{\partial x_i} (\bar{\rho} \bar{u}_i) = 0 \quad (2.57)$$

This is rewritten in terms of Favre-filtered variables as:

$$\frac{\partial \bar{\rho}}{\partial t} + \frac{\partial}{\partial x_i} (\bar{\rho} \tilde{u}_i) = 0 \quad (2.58)$$

Filtering the momentum equation yields:

$$\frac{\partial}{\partial t} (\bar{\rho} \bar{u}_i) + \frac{\partial}{\partial x_j} (\bar{\rho} \bar{u}_i \bar{u}_j) = - \frac{\partial \bar{P}}{\partial x_i} + \frac{\partial \bar{\tau}_{ij}}{\partial x_j} \quad (2.59)$$

Rewriting this in terms of Favre-filtered variables results in:

$$\frac{\partial}{\partial t} (\bar{\rho} \tilde{u}_i) + \frac{\partial}{\partial x_j} (\bar{\rho} \tilde{u}_i \tilde{u}_j) = -\frac{\partial \bar{P}}{\partial x_i} + \frac{\partial \bar{\tau}_{ij}}{\partial x_j} \quad (2.60)$$

The convective term is further expanded:

$$\begin{aligned} \frac{\partial}{\partial x_j} (\bar{\rho} \tilde{u}_i \tilde{u}_j) &= \frac{\partial}{\partial x_j} \left(\bar{\rho} (\tilde{u}_i + \tilde{u}'_i) (\tilde{u}_j + \tilde{u}'_j) \right) \\ &= \frac{\partial}{\partial x_j} \left[\bar{\rho} \left(\tilde{u}_i \tilde{u}_j + \tilde{u}_i \tilde{u}'_j + \tilde{u}'_i \tilde{u}_j + \tilde{u}'_i \tilde{u}'_j \right) \right] \end{aligned} \quad (2.61)$$

This is reorganized to separate the resolved convective term from the unresolved (subgrid-scale) terms as follows:

$$\begin{aligned} \frac{\partial}{\partial x_j} (\bar{\rho} \tilde{u}_i \tilde{u}_j) &= \frac{\partial}{\partial x_j} \bar{\rho} (\tilde{u}_i \tilde{u}_j) + \frac{\partial}{\partial x_j} \left[\bar{\rho} \left(\tilde{u}_i \tilde{u}_j - \tilde{u}_i \tilde{u}_j \right) \right] + \\ &\quad \frac{\partial}{\partial x_j} \left[\bar{\rho} \left(\tilde{u}_i \tilde{u}'_j - \tilde{u}'_i \tilde{u}_j \right) \right] + \frac{\partial}{\partial x_j} \left(\bar{\rho} \tilde{u}'_i \tilde{u}'_j \right) \end{aligned} \quad (2.62)$$

The right side of equation (2.62) contains the resolved convective term, Leonard stress, cross stress, and subgrid scale Reynolds stress, respectively. This is often written in more compact form as:

$$\frac{\partial}{\partial x_j} (\bar{\rho} \tilde{u}_i \tilde{u}_j) = \frac{\partial}{\partial x_j} \bar{\rho} (\tilde{u}_i \tilde{u}_j) + \frac{\partial}{\partial x_j} [\bar{\rho} (\tilde{u}_i \tilde{u}_j - \tilde{u}_i \tilde{u}_j)] \quad (2.63)$$

The cross stress and subgrid stress are frequently modeled together, while the magnitude of the Leonard stress is on the order of the truncation error when employing most finite difference schemes, and as a result, is implicitly represented [114]. Other authors such as Choi et. al [20] neglect the cross stress and

Leonard stress contributions entirely. For the method presented in this work, it is assumed that the Leonard, cross stress, and subgrid-scale Reynolds stress can be modeled together as the subgrid-stress term, as is done in reference [17] or:

$$\begin{aligned}\tau_{ij}^{sgs} &= \bar{\rho} \left(\widetilde{\hat{u}_i \hat{u}_j} - \hat{u}_i \hat{u}_j \right) + \bar{\rho} \left(\widetilde{\hat{u}_i u'_j} - \widetilde{u'_i \hat{u}_j} \right) + \bar{\rho} \widetilde{u'_i u'_j} \\ &= \bar{\rho} \left(\widetilde{\hat{u}_i \hat{u}_j} - \hat{u}_i \hat{u}_j \right)\end{aligned}\quad (2.64)$$

The subgrid scale Reynolds stress is replaced with a model. In contrast to the Reynolds stress resulting from the time averaging process appearing in equation (2.28), in which all turbulent motion is replaced by a model, the subgrid model employed here only represents the net effects of turbulence motion that is not resolved by the computational method. More details of both the RANS and LES turbulence modeling will be provided in a later section.

The final form of the filtered momentum expression that will be used for the LES calculations is:

$$\frac{\partial}{\partial t} (\bar{\rho} \hat{u}_i) + \frac{\partial}{\partial x_j} (\bar{\rho} \hat{u}_i \hat{u}_j) = - \frac{\partial \bar{P}}{\partial x_i} + \frac{\partial \bar{\tau}_{ij}}{\partial x_j} + \frac{\partial \tau_{ij}^{sgs}}{\partial x_j} \quad (2.65)$$

Many different forms of the energy equation are used by researchers investigating compressible flows with LES. Piomelli provides a comprehensive summary of several forms of the energy equation in reference [78]. The form used in this work solves for the total energy, as defined in equation (2.3).

The Favre-filtered energy expression has the form:

$$\begin{aligned} \frac{\partial}{\partial t} (\bar{\rho} \dot{c} + \frac{1}{2} \bar{\rho} \bar{u}_i \bar{u}_i) + \frac{\partial}{\partial x_j} (\bar{\rho} \bar{u}_j \bar{h} + \frac{1}{2} \bar{\rho} \bar{u}_j \bar{u}_i \bar{u}_i) \\ = \frac{\partial}{\partial x_j} (\bar{u}_i \bar{\tau}_{ij}) - \frac{\partial}{\partial x_j} (\bar{q}_j) \end{aligned} \quad (2.66)$$

The kinetic energy part of the time dependent term is rewritten analogously to the convective term of the momentum equation:

$$\begin{aligned} \frac{1}{2} \bar{\rho} \bar{u}_i \bar{u}_i = \frac{1}{2} \bar{\rho} \bar{u}_i \bar{u}_i + \frac{1}{2} \bar{\rho} (\bar{u}_i \bar{u}_i - \bar{u}_i \bar{u}_i) \\ = \frac{1}{2} \bar{\rho} \bar{u}_i \bar{u}_i + \bar{k} \end{aligned} \quad (2.67)$$

where \bar{k} is the unresolved kinetic energy term.

The expression involving enthalpy in equation (2.66) can also be rewritten as the sum of resolved and unresolved components:

$$\bar{\rho} \bar{u}_j \bar{h} = \bar{\rho} \bar{u}_j \bar{h} + \bar{\rho} (\bar{u}_j \bar{h} - \bar{u}_j \bar{h}) \quad (2.68)$$

The unresolved term on the right side of equation (2.68) is the subgrid scale heat flux, so that equation (2.68) becomes:

$$\bar{\rho} \bar{u}_j \bar{h} = \bar{\rho} \bar{u}_j \bar{h} + q_j^{sgs} \quad (2.69)$$

The kinetic energy part of the convective term in equation (2.66) is expanded as follows:

$$\begin{aligned} \frac{1}{2} \bar{\rho} \bar{u}_j \bar{u}_i \bar{u}_i = \frac{1}{2} \bar{\rho} (\bar{u}_j \bar{u}_i \bar{u}_i + 2 \bar{u}_j \bar{u}_i \bar{u}'_i + \bar{u}_j \bar{u}'_i \bar{u}'_i + \bar{u}'_j \bar{u}_i \bar{u}_i \\ + 2 \bar{u}'_j \bar{u}_i \bar{u}'_i + \bar{u}'_j \bar{u}'_i \bar{u}'_i) \end{aligned} \quad (2.70)$$

Rewriting this in terms of resolved and unresolved components results in the following expression:

$$\begin{aligned} \frac{1}{2} \overline{\rho} \widehat{u_j u_i u_i} = & \frac{1}{2} \overline{\rho} (\widehat{u_j} \widehat{u_i} \widehat{u_i}) + \frac{1}{2} \overline{\rho} (\widehat{u_j} \widehat{u_i} \widehat{u_i} - \widehat{u_j} \widehat{u_i} \widehat{u_i} + 2 \widehat{u_j} \widehat{u_i} \widehat{u_i} + \widehat{u'_j} \widehat{u_i} \widehat{u_i} + \widehat{u'_j} \widehat{u'_i} \widehat{u'_i} \\ & + \widehat{u_j} \widehat{u'_i} \widehat{u'_i} + 2 \widehat{u'_j} \widehat{u_i} \widehat{u'_i}) \end{aligned} \quad (2.71)$$

Of unresolved terms in equation (2.71), it is common practice to ignore all terms except for the last two term, as demonstrated in reference [82]. Following Ragab, the next-to-last term is rewritten as:

$$\frac{1}{2} \overline{\rho} \widehat{u_j u'_i u'_i} = \widehat{u_j} \widehat{k} \quad (2.72)$$

and the last term is rewritten as:

$$\overline{\rho} \widehat{u'_j} \widehat{u_i} \widehat{u'_i} = \widehat{u_i} \tau_{ij}^{sgs} \quad (2.73)$$

The viscous dissipation term on the right side of equation (2.66) is rewritten as the sum of resolved and unresolved components as follows:

$$\frac{\partial}{\partial x_j} (\overline{u_i \tau_{ij}}) = \frac{\partial}{\partial x_j} (\widehat{u_i} \overline{\tau_{ij}}) + \frac{\partial}{\partial x_j} (\widehat{u_i} \overline{\tau_{ij}} - \overline{u_i \tau_{ij}}) \quad (2.74)$$

It is common practice to assume that only the resolved dissipation term on the right side of equation (2.74) is important, although Erlebacher [27] and Piomelli [78] indicate that the unresolved contributions should not be ignored for highly compressible flows.

The heat flux term is left unchanged, as was done for the RANS energy equation in the preceding section. Rewriting the filtered energy equation (2.66) with the terms derived in equations (2.67, 2.69, 2.72, 2.73, and 2.74), the following form is obtained:

$$\begin{aligned} \frac{\partial}{\partial t} (\bar{\rho}\hat{\epsilon} + \frac{1}{2}\bar{\rho}\hat{u}_i\hat{u}_i + \bar{k}) + \frac{\partial}{\partial x_j} (\bar{\rho}\hat{u}_j\bar{h} + \frac{1}{2}\bar{\rho}\hat{u}_j\hat{u}_i\hat{u}_i + \hat{u}_j\bar{k}) \\ = \frac{\partial}{\partial x_j} (\hat{u}_i\bar{\tau}_{ij} + \hat{u}_i\tau_{ij}^{sgs}) - \frac{\partial}{\partial x_j} (\bar{q}_j + q_j^{sgs}) \end{aligned} \quad (2.75)$$

The final form of the LES energy equation is obtained using a procedure analogous to that used to obtain the final RANS energy equation (2.48). First, the terms involving the unresolved turbulent kinetic energy are assumed to be small compared to the other terms in the filtered energy equation, and the enthalpy term is recast as $\bar{\rho}\bar{h} = \bar{\rho}\hat{\epsilon} + \bar{P}$. Then, the resolved total energy is defined to be the sum of the resolved internal energy and the resolved kinetic energy:

$$\tilde{E}_t = \bar{\rho}\hat{\epsilon} + \frac{1}{2}\bar{\rho}\hat{u}_i\hat{u}_i \quad (2.76)$$

The resulting final form of the filtered LES energy equation is:

$$\frac{\partial}{\partial t} (\tilde{E}_t) + \frac{\partial}{\partial x_j} (\hat{u}_j\tilde{E}_t + \hat{u}_j\bar{P}) = \frac{\partial}{\partial x_j} (\hat{u}_i\bar{\tau}_{ij} + \hat{u}_i\tau_{ij}^{sgs}) - \frac{\partial}{\partial x_j} (\bar{q}_j + q_j^{sgs}) \quad (2.77)$$

2.4 Turbulence Modeling

Both the RANS and LES sets of equations derived in sections 2.2 and 2.3 require a turbulence model to close the momentum and energy equations. In the RANS approach, all unsteady turbulent motion is replaced by a turbulence model. The

resulting LES equations are very similar in appearance to the RANS equations, and also require a model to close the momentum and energy equations. The difference for the LES equations, however, is that the terms replaced by a model are only the turbulent terms that are too small to be resolved using the filtered LES equations. As a result, the large scale turbulent motion is directly calculated, and the effects of the smallest scale turbulence are accounted for using a subgrid turbulence model.

The turbulence model employed here to close the RANS equations is the Cebeci-Smith algebraic turbulence model [18,19]. Since the RANS equations are only used in this hybrid method to calculate wall boundary layer regions with no adverse pressure gradients, the selection of a relatively simple algebraic model such as the Cebeci-Smith formulation is appropriate. The wall function technique of Ota and Goldberg [73] is used in conjunction with the Cebeci-Smith model to enable use of a computational grid with the first point off solid boundaries placed in the logarithmic layer. This wall function approach is based upon the compressible law of the wall formulation of White and Christoph [110,111]. The filtered LES equations are closed using the Smagorinsky subgrid model [94].

Implementation of the wall function technique is critical to the development of this hybrid approach in order to enable use of a single computational grid extending continuously from the RANS regions to the LES regions. If a wall function approach were not used, grids for the RANS regions would have to be packed very tightly to the wall and use significant grid stretching, while a separate grid which minimizes grid stretching would need to be constructed for the LES region. Use of such non-continuous grids for the RANS and LES regions would require an

interpolation scheme that would likely introduce undesirable errors into the combined hybrid method.

Use of the Cebeci-Smith model to close the RANS equations and the Smagorinsky subgrid model to close the LES equations is desirable in terms of code implementation. While the function of the Cebeci-Smith model to replace all of the turbulent stresses with a model is quite different from that of the Smagorinsky subgrid model, which only replaces the small subgrid turbulent stresses, both are eddy viscosity models and are derived at least in part from mixing-length theory. The similar formulation of these two models enables the RANS equations and LES equations to be solved with a single solution scheme and computational grid, as mentioned previously. For a compressible nozzle or mixing layer flow, such as that depicted in figure 1.1, the change from RANS regions to LES region occurs at the vertical plane passing through the trailing edge of the splitter separating the wall bounded flows.

In the following sections, details of the Cebeci-Smith turbulence model and the Smagorinsky subgrid model are provided.

2.4.1 RANS Turbulence Model

The unclosed terms from the RANS momentum and energy equations are the Reynolds stress shown in equation (2.28) and the turbulent heat flux, which is given in equation (2.40). As mentioned previously in section 1.1, the Boussinesq approximation is used to relate the turbulent Reynolds stress to the mean rate of strain tensor through a turbulent (or eddy) viscosity. This is directly analogous to

equation (2.9) which relates the viscous stress to the mean rate of strain through the molecular (or laminar) viscosity. The turbulent analogy to equation (2.9) is:

$$\begin{aligned}\tau_{ij}^T &= -\overline{\rho u_i'' u_j''} \\ &= \mu^T \left(2\hat{S}_{ij} - \frac{2}{3} \frac{\partial \hat{u}_k}{\partial x_k} \delta_{ij} \right)\end{aligned}\quad (2.78)$$

Similarly, the turbulent heat flux is related to the temperature gradient through a turbulent conductivity, k^T :

$$\begin{aligned}q_j^T &= \overline{\rho u_j'' h''} \\ &= -k^T \frac{\partial \hat{T}}{\partial x_j}\end{aligned}\quad (2.79)$$

The turbulent Prandtl number, Pr^T is used to relate the turbulent viscosity to the turbulent conductivity:

$$Pr^T = \frac{\mu^T C_P}{k^T} \quad (2.80)$$

The turbulent Prandtl number is taken to be a constant here and equal to 0.9. Using equation (2.80) and assuming a constant turbulent Prandtl number enables the turbulent heat flux to be expressed as a function of the turbulent viscosity that is used to calculate the Reynolds stress. The turbulent heat flux becomes:

$$q_j^T = -\frac{C_P \mu^T}{Pr^T} \frac{\partial \hat{T}}{\partial x_j} \quad (2.81)$$

The Cebeci-Smith model, which was chosen here to close the RANS equations in the wall boundary layer regions, treats the wall boundary layer as having inner and outer regions where the turbulent viscosity is defined as:

$$\mu^T = \begin{cases} \mu_{inner}^T, & y \leq y_m \\ \mu_{outer}^T, & y > y_m \end{cases} \quad (2.82)$$

In equation (2.82), y_m is defined as the smallest value of y (the distance away from a wall) at which $\mu_{inner}^T = \mu_{outer}^T$. The expressions for the inner and outer layer turbulent viscosities are as follows:

Inner Layer:

$$\mu_{inner}^T = \bar{\rho} \ell_{mix}^2 \sqrt{\left(\frac{\partial \hat{u}}{\partial y} \right)^2 + \left(\frac{\partial \hat{v}}{\partial x} \right)^2} \quad (2.83)$$

with the mixing length ℓ_{mix} is given by:

$$\ell_{mix} = \kappa y \left(1 - e^{-y^+ / A^+} \right) \quad (2.84)$$

Outer Layer:

$$\mu_{outer}^T = \alpha \bar{\rho} \delta_v u_\epsilon F_{kleb} \quad (2.85)$$

In equation (2.85), the quantity δ_v is the velocity thickness, u_ϵ is the boundary layer edge velocity, and F_{kleb} is the Klebanoff intermittency function. The velocity thickness is defined as:

$$\delta_v = \int_0^\delta \left(1 - \frac{u}{u_\epsilon} \right) dy \quad (2.86)$$

This velocity thickness is identical to the displacement thickness for incompressible flows.

In references [52] and [53], Klebanoff presents an expression for the intermittency of turbulence near the edge of a boundary, which has a functional form involving the complimentary error function. This original intermittency function is usually approximated by the following formula, as indicated by Cebeci [18]:

$$F_{kleb} = \left[1 + 5.5 \left(\frac{y}{\delta} \right)^6 \right]^{-1} \quad (2.87)$$

The closure coefficients appearing in equations (2.84) and (2.85) are

$$\kappa = 0.40 \quad \alpha = 0.0168 \quad A^+ = 26$$

Wall Function Implementation:

The Cebeci-Smith model is usually integrated down to the wall, using a computational grid with the first point off of the wall placed well within the laminar sublayer, corresponding to $y^+ < 5$. For the hybrid method developed in this work, the objective is to place the first point off of the wall in the logarithmic layer to enable the use of computational grids that are not packed as tightly to the wall. Removing the tight spacing requirement will enable a continuous grid into the LES region. In addition, because the allowable time step of the computations is proportional to the size of the smallest grid cell, a less tightly packed grid enables a larger time step for the solution scheme. The wall function technique of Ota and Goldberg [73] is one of the more simple and effective methods currently in use, and it is the technique used in this work.

Wall functions have been implemented most frequently in conjunction with two-equation $k-\epsilon$ models. The benefits of implementing a wall function for use with

a $k-\epsilon$ model are the same as that for the Cebeci-Smith model used in this work including reducing grid requirements, and increasing the permissible time step of the computations. In addition, the need for the near-wall damping terms associated with low-Reynolds number $k-\epsilon$ models is removed. These near-wall damping terms frequently result in numerical stiffness of the solution procedure. Nichols [72] implemented the White-Christoph law of the wall with a $k-\epsilon$ model for application to time dependent aerodynamic flows. Mani [64] implemented the Ota-Goldberg formulation in the WIND code for use with turbulence models ranging from algebraic to two-equation formulations.

The use of a wall-function approach is strictly only valid in flow regions absent of adverse pressure gradients and separations, due to the assumption that the law of the wall holds. However, Avva et al. [2] have shown results for separated flows in which wall function methods perform no worse than methods integrating to the wall. The intention of the wall function implementation in this work is to only apply the method to attached wall boundary layers where the law of the wall is valid. The wall function approach is compared to the standard procedure of integrating to the wall for two supersonic boundary layers in chapter 4.

The Ota-Goldberg wall function employs the White-Christoph [110,111] compressible law of the wall:

$$u_2^+ = \frac{1}{\sqrt{\gamma}} \sin \left(\frac{\sqrt{\gamma}}{\kappa} \ln \frac{y_2^+}{y_0^+} \right) \quad (2.88)$$

where the compressibility parameter γ is given by:

$$\gamma = \frac{ru_\tau^2}{2C_P T_w} \quad (2.89)$$

In equation (2.88) u_2^+ is the value of u^+ at the first point off of the wall, y_2^+ is the value of y^+ at the first point off of the wall, and $y_0^+ = 0.1287$. In equation (2.89), the parameter r is the recovery factor, which is typically taken to be $Pr^{\frac{1}{3}}$ for turbulent boundary layers, and T_w is the wall temperature. An iteration procedure is used with equations (2.88) and (2.89) to solve for u_2^+ , from which the shear velocity u_τ can be obtained:

$$u_2^+ = \frac{u_2}{u_\tau} \quad (2.90)$$

Finally, the shear velocity is used to compute the wall shear stress through:

$$\tau_w = \rho u_\tau^2. \quad (2.91)$$

The wall shear stress calculated in equation (2.91) is then used in the solution scheme for the momentum and energy equations in the RANS regions.

2.4.2 LES Subgrid Scale Model

The terms that must be closed for LES equations are the subgrid-scale stress given by equation (2.28) and the subgrid scale heat flux, shown in equation (2.69). The earliest subgrid scale model for LES computations was developed by Smagorinsky [94]. Despite significant efforts to develop more sophisticated subgrid scale models, the Smagorinsky formulation is still widely used, and is itself the

foundation upon which some of the more sophisticated models are derived. The form of the model is very similar to the Cebeci-Smith model used for the RANS equations, in that a gradient-diffusion mixing-length approach is used.

The Smagorinsky expression for the subgrid scale stress is:

$$\begin{aligned}\tau_{ij}^{sgs} &= \bar{\rho} (\widetilde{u_i u_j} - \bar{u}_i \bar{u}_j) \\ &= 2(C_S \Delta)^2 \bar{\rho} \sqrt{\pi} (\tilde{S}_{ij} - \frac{1}{3} \tilde{S}_{kk} \delta_{ij}) - \frac{2}{3} C_I \Delta^2 \bar{\rho} \pi \delta_{ij}\end{aligned}\quad (2.92)$$

The parameter π is defined:

$$\pi = \tilde{S}_{ij} \tilde{S}_{ij} \quad (2.93)$$

The parameter Δ is the filter width and as a result, it is also used as the length scale that is characteristic of the subgrid turbulence. For use with a computational method, Δ is usually taken to be the grid spacing. In three dimensions, with a computational grid having unequal spacing in the three directions, this subgrid length scale is usually taken to be:

$$\Delta = (\Delta x \Delta y \Delta z)^{\frac{1}{3}} \quad (2.94)$$

For computational grids with substantially different spacing in the three directions, an alternative form (see Ragab [82]) is

$$\Delta = \left[\frac{(\Delta x)^2 + (\Delta y)^2 + (\Delta z)^2}{3} \right]^{\frac{1}{2}} \quad (2.95)$$

In the three dimensional simulations of a compressible mixing layer discussed later in this work, the two forms of the subgrid length scale presented in equations (2.94) and (2.95) are investigated. The constants C_s and C_I have been found to be highly dependent on the flow under investigation. Rogallo and Moin [85] suggest a range for C_s in the range $0.10 \leq C_s \leq 0.24$. Both of the limits on C_s given by Rogallo and Moin are investigated for the mixing layer in this work. The constant C_I is usually equal to 0.01, but several authors, including Ragab [82] and Choi et al. [20] mention that the contribution of the term involving C_I may not be important and may be neglected. This approach is taken in this work, and as a result, the original expression for the Smagorinsky subgrid scale stress in equation (2.92) may be rewritten as follows:

$$\tau_{ij}^{sgs} = 2\mu^{sgs} \hat{S}_{ij} - \frac{2}{3}\mu^{sgs} \frac{\partial \hat{u}_j}{\partial x_i} \delta_{ij} \quad (2.96)$$

where the subgrid scale turbulent viscosity is given by:

$$\mu^{sgs} = \bar{\rho}(C_s \Delta)^2 \sqrt{\pi} \quad (2.97)$$

Note the similar form of equation (2.97) to the expression for the Cebeci-Smith inner region turbulent viscosity in equation (2.83). While the mixing length defined for the Cebeci-Smith model is used to characterize all of the turbulent motion, the length scale defined here for the Smagorinsky model only characterizes the subgrid-scale motion.

Finally, the subgrid scale heat flux is modeled analogously to that done for the turbulent heat flux of the RANS equations:

$$\begin{aligned}
q_j^{sgs} &= \bar{\rho} \left(\widetilde{u_j h} - \tilde{u}_j \tilde{h} \right) \\
&= -k^{sgs} \frac{\partial \tilde{T}}{\partial x_j}
\end{aligned} \tag{2.98}$$

where k^{sgs} is related to μ^{sgs} through the turbulent Prandtl number. As in the RANS regions, the turbulent Prandtl number is assumed to be constant in the LES regions and equal to 0.9. The subgrid scale heat flux becomes

$$q_j^{sgs} = -\frac{C_P \mu^{sgs}}{Pr^T} \frac{\partial \tilde{T}}{\partial x_j} \tag{2.99}$$

CHAPTER 3

SOLUTION PROCEDURE

The procedure used to solve the equations developed in chapter 2 is formulated in this chapter. The RANS and LES equation sets are recast in vector form, which corresponds directly to the form of the equations that are solved by the computational method. The numerical scheme used to solve these equation sets is first illustrated using a one-dimensional model problem. The extension of the solution scheme to the RANS and LES equations in three dimensions on stretched, non-rectangular computational grids is presented next. The use of a generalized coordinate transformation, time-step selection, and artificial dissipation is discussed.

3.1 Governing Equations

Before discussing the numerical method used in this hybrid method, the RANS and LES equations are expressed in vector notation, which combines the continuity, three momentum equations (corresponding to each of the cartesian coordinates), and the energy equation into a compact form that is actually used by the solution scheme. For reference, the RANS and LES equations derived using tensor notation in chapter 2 are repeated here. The equations written here differ from those in

chapter 2 only in that all terms now appear on the left side of the equations, which will make the conversion to the vector notation more straightforward.

In the RANS regions, the continuity, momentum, and energy equations are:

$$\frac{\partial \bar{\rho}}{\partial t} + \frac{\partial}{\partial x_i} (\bar{\rho} \hat{u}_i) = 0 \quad (3.1)$$

$$\frac{\partial}{\partial t} (\bar{\rho} \hat{u}_i) + \frac{\partial}{\partial x_j} (\bar{\rho} \hat{u}_i \hat{u}_j) + \frac{\partial \bar{P}}{\partial x_i} - \frac{\partial \bar{\tau}_{ij}}{\partial x_j} - \frac{\partial \tau_{ij}^T}{\partial x_j} = 0 \quad (3.2)$$

$$\frac{\partial}{\partial t} (\hat{E}_t) + \frac{\partial}{\partial x_j} (\hat{u}_j \hat{E}_t + \hat{u}_j \bar{P}) - \frac{\partial}{\partial x_j} (\hat{u}_i \bar{\tau}_{ij} + \hat{u}_i \tau_{ij}^T) + \frac{\partial}{\partial x_j} (\bar{q}_j + q_j^T) = 0 \quad (3.3)$$

Likewise in the LES region, the continuity, momentum, and energy equations are:

$$\frac{\partial \bar{\rho}}{\partial t} + \frac{\partial}{\partial x_i} (\bar{\rho} \hat{u}_i) = 0 \quad (3.4)$$

$$\frac{\partial}{\partial t} (\bar{\rho} \hat{u}_i) + \frac{\partial}{\partial x_j} (\bar{\rho} \hat{u}_i \hat{u}_j) + \frac{\partial \bar{P}}{\partial x_i} - \frac{\partial \bar{\tau}_{ij}}{\partial x_j} - \frac{\partial \tau_{ij}^{sgs}}{\partial x_j} = 0 \quad (3.5)$$

$$\frac{\partial}{\partial t} (\hat{E}_t) + \frac{\partial}{\partial x_j} (\hat{u}_j \hat{E}_t + \hat{u}_j \bar{P}) - \frac{\partial}{\partial x_j} (\hat{u}_i \bar{\tau}_{ij} + \hat{u}_i \tau_{ij}^{sgs}) + \frac{\partial}{\partial x_j} (\bar{q}_j + q_j^{sgs}) = 0 \quad (3.6)$$

Both the RANS equations (3.1 - 3.3) and the LES equations (3.4 - 3.6) can be expressed in Cartesian coordinates (x,y,z) using the compact vector form:

$$\frac{\partial \mathbf{Q}}{\partial t} + \frac{\partial \mathbf{E}}{\partial x} + \frac{\partial \mathbf{F}}{\partial y} + \frac{\partial \mathbf{G}}{\partial z} = 0 \quad (3.7)$$

For the RANS equations, the vectors \mathbf{Q} , \mathbf{E} , \mathbf{F} , and \mathbf{G} are:

$$\mathbf{Q} = \begin{bmatrix} \bar{\rho} \\ \bar{\rho}\hat{u} \\ \bar{\rho}\hat{v} \\ \bar{\rho}\hat{w} \\ \hat{E}_t \end{bmatrix} \quad (3.8)$$

$$\mathbf{E} = \begin{bmatrix} \bar{\rho}\hat{u} \\ \bar{\rho}\hat{u}^2 + \bar{P} - \bar{\tau}_{xx} - \tau_{xx}^T \\ \bar{\rho}\hat{u}\hat{v} - \bar{\tau}_{xy} - \tau_{xy}^T \\ \bar{\rho}\hat{u}\hat{w} - \bar{\tau}_{xz} - \tau_{xz}^T \\ \hat{u}[\hat{E}_t + \bar{P}] - \hat{u}(\bar{\tau}_{xx} + \tau_{xx}^T) - \hat{v}(\bar{\tau}_{xy} + \tau_{xy}^T) - \hat{w}(\bar{\tau}_{xz} + \tau_{xz}^T) + \hat{q}_x + q_x^T \end{bmatrix} \quad (3.9)$$

$$\mathbf{F} = \begin{bmatrix} \bar{\rho}\hat{v} \\ \bar{\rho}\hat{u}\hat{v} - \bar{\tau}_{xy} - \tau_{xy}^T \\ \bar{\rho}\hat{v}^2 + \bar{P} - \bar{\tau}_{yy} - \tau_{yy}^T \\ \bar{\rho}\hat{v}\hat{w} - \bar{\tau}_{yz} - \tau_{yz}^T \\ \hat{v}[\hat{E}_t + \bar{P}] - \hat{u}(\bar{\tau}_{xy} + \tau_{xy}^T) - \hat{v}(\bar{\tau}_{yy} + \tau_{yy}^T) - \hat{w}(\bar{\tau}_{yz} + \tau_{yz}^T) + \hat{q}_y + q_y^T \end{bmatrix} \quad (3.10)$$

$$\mathbf{G} = \begin{bmatrix} \bar{\rho}\hat{w} \\ \bar{\rho}\hat{u}\hat{w} - \bar{\tau}_{xz} - \tau_{xz}^T \\ \bar{\rho}\hat{v}\hat{w} - \bar{\tau}_{yz} - \tau_{yz}^T \\ \bar{\rho}\hat{w}^2 + \bar{P} - \bar{\tau}_{zz} - \tau_{zz}^T \\ \hat{w}[\hat{E}_t + \bar{P}] - \hat{u}(\bar{\tau}_{xz} + \tau_{xz}^T) - \hat{v}(\bar{\tau}_{yz} + \tau_{yz}^T) - \hat{w}(\bar{\tau}_{zz} + \tau_{zz}^T) + \hat{q}_z + q_z^T \end{bmatrix} \quad (3.11)$$

In section 2.4.1, the form of the modeled turbulent stress in equation (2.78) was shown to be the product of a turbulent viscosity and the mean rate of strain term. This was directly analogous to the form of the viscous stress tensor shown in equation (2.9) which was defined as the product of a laminar viscosity and the same mean rate of strain term. This similarity allows the viscous and turbulent stresses in the flux vectors **E**, **F**, and **G** to be written together as the product of an effective viscosity, $\mu + \mu^T$ and the mean rate of strain term. These combined stresses are as follows:

$$\begin{aligned}
 \bar{\tau}_{xx} + \tau_{xx}^T &= \frac{2}{3} (\mu + \mu^T) \left(2 \frac{\partial \hat{u}}{\partial x} - \frac{\partial \hat{v}}{\partial y} - \frac{\partial \hat{w}}{\partial z} \right) \\
 \bar{\tau}_{yy} + \tau_{yy}^T &= \frac{2}{3} (\mu + \mu^T) \left(2 \frac{\partial \hat{v}}{\partial y} - \frac{\partial \hat{u}}{\partial x} - \frac{\partial \hat{w}}{\partial z} \right) \\
 \bar{\tau}_{zz} + \tau_{zz}^T &= \frac{2}{3} (\mu + \mu^T) \left(2 \frac{\partial \hat{w}}{\partial z} - \frac{\partial \hat{u}}{\partial x} - \frac{\partial \hat{v}}{\partial y} \right) \\
 \bar{\tau}_{xy} + \tau_{xy}^T &= \bar{\tau}_{yx} + \tau_{yx}^T = (\mu + \mu^T) \left(\frac{\partial \hat{u}}{\partial y} + \frac{\partial \hat{v}}{\partial x} \right) \\
 \bar{\tau}_{xz} + \tau_{xz}^T &= \bar{\tau}_{zx} + \tau_{zx}^T = (\mu + \mu^T) \left(\frac{\partial \hat{w}}{\partial x} + \frac{\partial \hat{u}}{\partial z} \right) \\
 \bar{\tau}_{yz} + \tau_{yz}^T &= \bar{\tau}_{zy} + \tau_{zy}^T = (\mu + \mu^T) \left(\frac{\partial \hat{v}}{\partial z} + \frac{\partial \hat{w}}{\partial y} \right)
 \end{aligned} \tag{3.12}$$

The same reasoning used to combine the viscous and turbulent stresses may be employed to combine the laminar and turbulent heat flux terms using an effective thermal conductivity $k + k^T$. The combined heat flux terms in the vectors **E**, **F**, and **G** are

$$\begin{aligned}
\bar{q}_x + q_x^T &= -(k + k^T) \frac{\partial \hat{T}}{\partial x} = - \left(\frac{C_P \mu}{Pr} + \frac{C_P \mu^T}{Pr^T} \right) \frac{\partial \hat{T}}{\partial x} \\
\bar{q}_y + q_y^T &= -(k + k^T) \frac{\partial \hat{T}}{\partial y} = - \left(\frac{C_P \mu}{Pr} + \frac{C_P \mu^T}{Pr^T} \right) \frac{\partial \hat{T}}{\partial y} \\
\bar{q}_z + q_z^T &= -(k + k^T) \frac{\partial \hat{T}}{\partial z} = - \left(\frac{C_P \mu}{Pr} + \frac{C_P \mu^T}{Pr^T} \right) \frac{\partial \hat{T}}{\partial z}
\end{aligned} \tag{3.13}$$

For the LES equations, the vectors **Q**, **E**, **F**, and **G** are:

$$\mathbf{Q} = \begin{bmatrix} \bar{\rho} \\ \bar{\rho} \tilde{u} \\ \bar{\rho} \tilde{v} \\ \bar{\rho} \tilde{w} \\ \hat{E}_t \end{bmatrix} \tag{3.14}$$

$$\mathbf{E} = \begin{bmatrix} \bar{\rho} \tilde{u} \\ \bar{\rho} \tilde{u}^2 + \bar{P} - \bar{\tau}_{xx} - \tau_{xx}^{sgs} \\ \bar{\rho} \tilde{u} \tilde{v} - \bar{\tau}_{xy} - \tau_{xy}^{sgs} \\ \bar{\rho} \tilde{u} \tilde{w} - \bar{\tau}_{xz} - \tau_{xz}^{sgs} \\ \tilde{u} [\hat{E}_t + \bar{P}] - \tilde{u} (\bar{\tau}_{xx} + \tau_{xx}^{sgs}) - \tilde{v} (\bar{\tau}_{xy} + \tau_{xy}^{sgs}) - \tilde{w} (\bar{\tau}_{xz} + \tau_{xz}^{sgs}) + \tilde{q}_x + q_x^{sgs} \end{bmatrix} \tag{3.15}$$

$$\mathbf{F} = \begin{bmatrix} \bar{\rho} \tilde{v} \\ \bar{\rho} \tilde{u} \tilde{v} - \bar{\tau}_{xy} - \tau_{xy}^{sgs} \\ \bar{\rho} \tilde{v}^2 + \bar{P} - \bar{\tau}_{yy} - \tau_{yy}^{sgs} \\ \bar{\rho} \tilde{v} \tilde{w} - \bar{\tau}_{yz} - \tau_{yz}^{sgs} \\ \tilde{v} [\hat{E}_t + \bar{P}] - \tilde{u} (\bar{\tau}_{xy} + \tau_{xy}^{sgs}) - \tilde{v} (\bar{\tau}_{yy} + \tau_{yy}^{sgs}) - \tilde{w} (\bar{\tau}_{yz} + \tau_{yz}^{sgs}) + \tilde{q}_y + q_y^{sgs} \end{bmatrix} \tag{3.16}$$

$$\mathbf{G} = \begin{bmatrix} \bar{\rho}\bar{w} \\ \bar{\rho}\bar{u}\bar{w} - \bar{\tau}_{xz} - \tau_{xz}^{sgs} \\ \bar{\rho}\bar{v}\bar{w} - \bar{\tau}_{yz} - \tau_{yz}^{sgs} \\ \bar{\rho}\bar{w}^2 + \bar{P} - \bar{\tau}_{zz} - \tau_{zz}^{sgs} \\ \bar{w} [\bar{E}_t + \bar{P}] - \bar{u} (\bar{\tau}_{xz} + \tau_{xz}^{sgs}) - \bar{v} (\bar{\tau}_{yz} + \tau_{yz}^{sgs}) - \bar{w} (\bar{\tau}_{zz} + \tau_{zz}^{sgs}) + \bar{q}_z + q_z^{sgs} \end{bmatrix} \quad (3.17)$$

As was done for the RANS equations, the viscous and subgrid scale stresses appearing in the flux vectors \mathbf{E} , \mathbf{F} , and \mathbf{G} are written together for the LES equations as the product of an effective viscosity $\mu + \mu^{sgs}$ and the resolved rate of strain term:

$$\begin{aligned} \bar{\tau}_{xx} + \tau_{xx}^{sgs} &= \frac{2}{3} (\mu + \mu^{sgs}) \left(2 \frac{\partial \bar{u}}{\partial x} - \frac{\partial \bar{v}}{\partial y} - \frac{\partial \bar{w}}{\partial z} \right) \\ \bar{\tau}_{yy} + \tau_{yy}^{sgs} &= \frac{2}{3} (\mu + \mu^{sgs}) \left(2 \frac{\partial \bar{v}}{\partial y} - \frac{\partial \bar{u}}{\partial x} - \frac{\partial \bar{w}}{\partial z} \right) \\ \bar{\tau}_{zz} + \tau_{zz}^{sgs} &= \frac{2}{3} (\mu + \mu^{sgs}) \left(2 \frac{\partial \bar{w}}{\partial z} - \frac{\partial \bar{u}}{\partial x} - \frac{\partial \bar{v}}{\partial y} \right) \\ \bar{\tau}_{xy} + \tau_{xy}^{sgs} &= \bar{\tau}_{yx} + \tau_{yx}^{sgs} = (\mu + \mu^{sgs}) \left(\frac{\partial \bar{u}}{\partial y} + \frac{\partial \bar{v}}{\partial x} \right) \\ \bar{\tau}_{xz} + \tau_{xz}^{sgs} &= \bar{\tau}_{zx} + \tau_{zx}^{sgs} = (\mu + \mu^{sgs}) \left(\frac{\partial \bar{w}}{\partial x} + \frac{\partial \bar{u}}{\partial z} \right) \\ \bar{\tau}_{yz} + \tau_{yz}^{sgs} &= \bar{\tau}_{zy} + \tau_{zy}^{sgs} = (\mu + \mu^{sgs}) \left(\frac{\partial \bar{v}}{\partial z} + \frac{\partial \bar{w}}{\partial y} \right) \end{aligned} \quad (3.18)$$

The laminar and turbulent heat fluxes are also expressed in a combined format using an effective thermal conductivity $k + k^{sgs}$:

$$\begin{aligned} \bar{q}_x + q_x^{sgs} &= - (k + k^{sgs}) \frac{\partial \tilde{T}}{\partial x} = - \left(\frac{C_P \mu}{Pr} + \frac{C_P \mu^{sgs}}{Pr^{sgs}} \right) \frac{\partial \tilde{T}}{\partial x} \\ \bar{q}_y + q_y^{sgs} &= - (k + k^{sgs}) \frac{\partial \tilde{T}}{\partial y} = - \left(\frac{C_P \mu}{Pr} + \frac{C_P \mu^{sgs}}{Pr^{sgs}} \right) \frac{\partial \tilde{T}}{\partial y} \\ \bar{q}_z + q_z^{sgs} &= - (k + k^{sgs}) \frac{\partial \tilde{T}}{\partial z} = - \left(\frac{C_P \mu}{Pr} + \frac{C_P \mu^{sgs}}{Pr^{sgs}} \right) \frac{\partial \tilde{T}}{\partial z} \end{aligned} \quad (3.19)$$

3.2 Numerical Method

The solution algorithm used in this work is the predictor-corrector scheme due to Gottlieb and Turkel [37]. This method was developed in the same philosophy as the original MacCormack scheme [61]. While the accuracy of the MacCormack scheme is second order in time and second order in space, the Gottlieb-Turkel scheme is second order accurate in time and effectively fourth order accurate in space, and as a result, is often referred to as the “MacCormack 2-4” scheme.

The Gottlieb-Turkel scheme has been applied to several time dependent flow problems because of its robustness, accuracy, and relative ease of implementation in methods for solving the Navier-Stokes equations. Snyder and Scott [95] demonstrated that the Gottlieb-Turkel was more accurate than other similar schemes for benchmark acoustic problems. Bayliss, et al. [8,9] successfully applied the scheme to boundary layer calculations. Ragab and Sheen [81,82] used the Gottlieb-Turkel scheme to perform LES calculations of compressible mixing layers in which the computational domain contained only the mixing region.

The Gottlieb-Turkel scheme is illustrated using the following one-dimensional equation, which is a simplified model equation of the vector equation (3.7):

$$\frac{\partial q}{\partial t} + \frac{\partial f}{\partial x} = 0 \quad (3.20)$$

The predictor step is:

$$q_i^* = q_i - \frac{\Delta t}{6\Delta x} (-7f_i + 8f_{i+1} - f_{i+2}) \quad (3.21)$$

The corrector step is:

$$q_i^{n+1} = \frac{1}{2} \left[q_i + q_i^* - \frac{\Delta t}{6\Delta x} (7f_i^* - 8f_{i-1}^* - f_{i+2}^*) \right] \quad (3.22)$$

The predictor-corrector scheme advances a solution in time from the time level (n) to ($n + 1$). The time step, Δt , is related to the grid spacing, Δx , and the propagation speed, A , through the CFL (Courant-Friedrichs-Lowy) number:

$$\Delta t = CFL \frac{\Delta x}{A} \quad (3.23)$$

The Gottlieb-Turkel scheme is cited by several authors, such as Hudson and Long [43], as providing second order accuracy in time and fourth order accuracy in space. Bayliss et al. [9] indicated that the scheme has fourth order accuracy only if Δt is of the order $(\Delta x)^2$, and Nelson [71] showed that the spatial accuracy of the scheme is only third order for CFL numbers approaching 1. A detailed analysis of the truncation error for the Gottlieb-Turkel scheme is provided in appendix A. This analysis shows that the leading truncation error terms resulting from discretization of the model equation 3.20 is obtained from the following equation:

$$\frac{\partial q}{\partial t} + \frac{\partial f}{\partial x} = -\frac{\Delta t^2}{6} \frac{\partial^3 q}{\partial t^3} - CFL \frac{\Delta x^3}{18} \frac{\partial^4 f}{\partial x^4} + \frac{\Delta x^4}{30} \frac{\partial^5 f}{\partial x^5} + \dots \quad (3.24)$$

The left side of this equation is the form of the model problem in equation (3.20) while the right side is the truncation error. The first term on the right side of

equation (A.13) indicates that the scheme provides second order accuracy in time. The second truncation error term indicates that the scheme is only third order accurate in space for *CFL* numbers approaching 1, as previously shown by Nelson [71]. However, for most problems in which the Gottlieb-Turkel scheme is used, the maximum *CFL* number is usually set to a value of 0.5 or less. In addition, for computational grids that employ non-uniform stretched grids, the limiting time step is inversely proportional to the smallest grid spacing and the resulting effective *CFL* number will be much smaller in regions where the grid spacing is larger. This is demonstrated by considering equation (3.23) for the case of variable grid spacing, Δx , but for a constant time step Δt . For such regions of the computational domain, the second truncation error term on the right side of equation (3.24) will be insignificant, and then the next truncation error term indicates that the scheme provides fourth order spatial accuracy. In conclusion, the Gottlieb-Turkel scheme is strictly second order accurate in time and third order accurate in space, but in the case of computational grids with significant stretching, the spatial accuracy is effectively fourth order for most of the computational domain.

3.3 Extension of the Gottlieb-Turkel Scheme to Generalized Coordinates

The Gottlieb-Turkel predictor-corrector scheme is extended to three dimensions and generalized curvilinear coordinates in this section. The use of generalized coordinates, necessary for the solution of the RANS and LES equations on computational grids with non-uniform stretched spacing and non-rectangular grid cells, is presented in section 3.3.1. The time step calculation procedure is discussed

in section 3.3.2 and the use of numerical dissipation for stability, particularly in the RANS regions, is discussed in section 3.3.3.

3.3.1 Generalized Coordinates

The three dimensional vector forms of the RANS and LES equations, both given by equation (3.7), are an extension of the one dimensional problem given in equation (3.20). The Gottlieb-Turkel scheme can be written for three dimensional problems as follows:

$$\mathbf{Q}^{n+1} = C_z C_y C_x P_z P_y P_x \mathbf{Q}^n \quad (3.25)$$

where P_x , P_y , and P_z are the one-dimensional predictor operators and C_x , C_y , and C_z are the one-dimensional corrector operators that correspond to the flux vectors \mathbf{E} , \mathbf{F} , and \mathbf{G} respectively.

The numerical scheme is further extended to generalized coordinates through the transformation of the RANS and LES equations from cartesian physical space (x, y, z) to computational space (ξ, η, ζ) . Hixon et al. [41] found that the chain rule formulation was more accurate than other formulations using generalized curvilinear coordinates. The chain rule formulation is used in this work, in which the flux vector derivatives are expressed as:

$$\begin{aligned} \frac{\partial \mathbf{E}}{\partial x} &= \xi_x \frac{\partial \mathbf{E}}{\partial \xi} + \eta_x \frac{\partial \mathbf{E}}{\partial \eta} + \zeta_x \frac{\partial \mathbf{E}}{\partial \zeta} \\ \frac{\partial \mathbf{F}}{\partial y} &= \xi_y \frac{\partial \mathbf{F}}{\partial \xi} + \eta_y \frac{\partial \mathbf{F}}{\partial \eta} + \zeta_y \frac{\partial \mathbf{F}}{\partial \zeta} \\ \frac{\partial \mathbf{G}}{\partial z} &= \xi_z \frac{\partial \mathbf{G}}{\partial \xi} + \eta_z \frac{\partial \mathbf{G}}{\partial \eta} + \zeta_z \frac{\partial \mathbf{G}}{\partial \zeta} \end{aligned} \quad (3.26)$$

The terms ξ_x , η_x , ζ_x , ξ_y , η_y , ζ_y , ξ_z , η_z , and ζ_z are the metrics of the transformation from physical space to computational space. The derivation of these metric terms are detailed in appendix B. They are computed using a fourth order finite difference method to be consistent with the Gottlieb-Turkel scheme.

The stress and heat flux terms appearing within the flux vector expressions for the RANS and LES equations were shown to involve the derivatives of the velocity components and temperature with respect to the cartesian coordinates x , y , and z in equations (3.12, 3.13) and (3.18, 3.19). These velocity and temperature derivatives are also computed using the chain rule form. For example, the RANS derivative of the mean velocity \hat{u} with respect to x is:

$$\frac{\partial \hat{u}}{\partial x} = \xi_x \frac{\partial \hat{u}}{\partial \xi} + \eta_x \frac{\partial \hat{u}}{\partial \eta} + \zeta_x \frac{\partial \hat{u}}{\partial \zeta} \quad (3.27)$$

Similarly, the LES derivative of the resolved velocity \tilde{u} with respect to x is:

$$\frac{\partial \tilde{u}}{\partial x} = \xi_x \frac{\partial \tilde{u}}{\partial \xi} + \eta_x \frac{\partial \tilde{u}}{\partial \eta} + \zeta_x \frac{\partial \tilde{u}}{\partial \zeta} \quad (3.28)$$

To compute the derivatives of the velocity and temperature terms with respect to the computational coordinates ξ, η, ζ , Bayliss et al. [9] have shown that a specific procedure is required retain the overall accuracy of the Gottlieb-Turkel scheme. For the predictor step, which uses forward differencing for the flux terms as shown in equation (3.21), the velocity and temperature derivatives taken in the same computational direction as the flux vector derivative are obtained with a two point backward difference operation, while the derivatives taken in the other two

directions are obtained with a central difference operation. For example, the u velocity derivatives taken to compute the flux vector terms $\frac{\partial \mathbf{E}}{\partial \xi}$, $\frac{\partial \mathbf{F}}{\partial \xi}$, and $\frac{\partial \mathbf{G}}{\partial \xi}$ in equation (3.26) are:

$$\begin{aligned}\frac{\partial \hat{u}}{\partial \xi} &= \hat{u}_i - \hat{u}_{i-1} \\ \frac{\partial \hat{u}}{\partial \eta} &= \frac{1}{2} (\hat{u}_{j+1} - \hat{u}_{j-1}) \\ \frac{\partial \hat{u}}{\partial \zeta} &= \frac{1}{2} (\hat{u}_{k+1} - \hat{u}_{k-1})\end{aligned}\quad (3.29)$$

A similar procedure is used for the corrector step, for which the flux terms are backward differenced, as shown in equation (3.22). The velocity and temperature derivatives taken in the same computational direction as the flux are calculated using a two-point forward differenced difference expression, while the derivatives in the other two directions are calculated with a central difference operation.

3.3.2 Time Step Calculation

A procedure for calculating a time step that will allow for stable calculations with predictor-corrector schemes was proposed by MacCormack in reference [62]. The procedure involves searching the entire computational domain for the minimum value of:

$$\Delta t = \left(\frac{|u|}{\Delta x} + \frac{|v|}{\Delta y} + \frac{|w|}{\Delta z} + a \sqrt{\frac{1}{(\Delta x)^2} + \frac{1}{(\Delta y)^2} + \frac{1}{(\Delta z)^2}} \right)^{-1} \quad (3.30)$$

The minimum time step obtained from equation (3.30) was modified through the use of the *CFL* number, which was always less than one for the Gottlieb-Turkel scheme, so that the actual time step used in the computations is given by:

$$\Delta t_{act} = CFL \Delta t \quad (3.31)$$

For the hybrid calculations of the compressible mixing layer, the calculated time step is allowed to vary during the initial transient part of the calculation, when the mixing layer is allowed to develop. For the rest of the calculation, however, the time step is fixed to a constant value corresponding to the minimum value observed during the initial transient development. A constant time step is necessary for the LES region to calculate turbulent statistics from flowfield data stored at constant intervals in time.

3.3.3 Numerical Dissipation

Numerical dissipation is usually required in Euler and RANS computations to remove numerical oscillations that are undesirable in terms of solution accuracy and code stability. These oscillations are typically at large wave numbers caused by nonlinearities in the solution process. Jameson et al. [46] and Pulliam [80] have developed numerical dissipation schemes that have been used extensively for Euler and Navier-Stokes calculations of aerodynamic flows. These schemes operate by adding dissipative terms to the equations of motion, and require careful use to keep the levels of numerical dissipation as small as possible while retaining stability of the solution.

For LES computations, the filtering process is used to develop a set of equations that only resolve the large scale unsteadiness associated with smaller wave numbers. The larger wave number unsteadiness, including both the subgrid scale turbulence

and the unphysical numerical oscillations, are handled through the use of a subgrid scale model. The eddy viscosity formulation of the Smagorinsky model used in this work effectively adds a viscous stress to the momentum and energy equations which serves to both replace the unresolved subgrid scale stresses and to damp unphysical oscillations away from the flow regions of interest.

Some authors such as Kennedy and Carpenter [48,49] and Hixon [40] have developed explicit filters for damping unphysical large wave number oscillations in time dependent flow calculations. These filters are not directly associated with the filtering process, described previously, used to derive the LES equations, but instead are another class of numerical dissipation schemes. Hixon [40] has shown that the explicit filters of Kennedy and Carpenter may be used in conjunction with explicit solvers such as the Gottlieb-Turkel scheme to damp unresolved oscillations, and as a result, this method is employed here.

The Kennedy and Carpenter filters have the form:

$$\check{\mathbf{Q}} = (1 + \alpha_n \mathbf{D}) \mathbf{Q} \quad (3.32)$$

where \mathbf{D} is a symmetric matrix filter function of order $2n (n = 1, 2, 3, \dots)$ and the coefficient α_n is given by:

$$\alpha_n = \frac{-(1)^n}{(2)^{-2n}} \quad (3.33)$$

Kennedy and Carpenter developed the filter $\alpha_n \mathbf{D}$ to be of a form that retains larger wave number components with increasing n , and to always be dissipative in effect.

The matrix function \mathbf{D} and the coefficient α_n are derived for filters of orders 2 through 20, corresponding to $n = 1, 10$ in reference [49]. In this work, an eighth order filter ($n = 4$) is used, which has the form in one dimension:

$$\alpha_n \mathbf{D} = \frac{(-q_{i-4} + 8q_{i-3} - 28q_{i-2} + 56q_{i-1} - 70q_i + 56q_{i+1} - 28q_{i+2} + 8q_{i+3} - q_{i+4})}{256} \quad (3.34)$$

Skewed stencils of similar form to equation (3.34) are used for points at and near boundaries. The filter function is applied everywhere in the RANS region, but is only applied in the LES region when a transient in pressure indicates that the solution scheme will numerically become unstable. As a result, the procedure used in the LES region is to modify the coefficient α_n to be a function of the local pressure, such that when the pressure at a point in the flow drops lower than 10 percent of a reference pressure characteristic of the flow, α_n , is modified to be

$$\alpha_n = \frac{-(1)^n}{(2)^{-2n}} \left(\frac{.10P_{ref}}{P} \right)^4 \quad (3.35)$$

CHAPTER 4

RANS CALCULATIONS OF WALL BOUNDARY LAYERS

In this chapter, a series of flat plate boundary layers are calculated to investigate the RANS solver of the hybrid method. Since no free shear layer mixing regions occur in these cases, the LES part of the method is not used in these calculations. All of these boundary layer calculations were obtained for a flowfield situation depicted by figure 4.1 where a uniform inflow meets a smooth flat plate and a boundary layer develops over the plate surface.

The first case considered here is an incompressible laminar boundary layer that is calculated using the RANS solver without any turbulence model. The second case is an incompressible turbulent boundary layer that is calculated with the Cebeci-Smith turbulence model integrated to the wall, without the use the wall function approach. This will be referred to hereafter as the “wall-integration” approach. The third and fourth cases investigate two supersonic boundary layers that have the same flow conditions as the two isolated flows that form the mixing layer which will be investigated in the next two chapters using the combined RANS-LES procedure. These last two boundary layer calculations are run with both the wall-integration and wall-function approaches. With the formulation of the

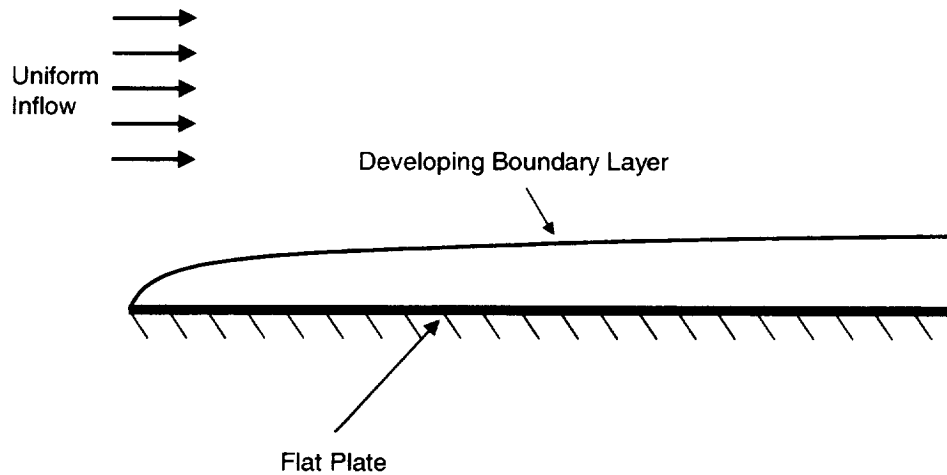


Figure 4.1: Schematic of flat plate boundary layer

RANS solution procedure to march in time using the Gottlieb-Turkel scheme, the flowfields for all of these cases are initially set to the freestream conditions everywhere in the computational domain, and the calculations progress until a steady state solution is obtained. The residual error and flowfield quantities such as the skin friction coefficient were used to monitor convergence to steady state.

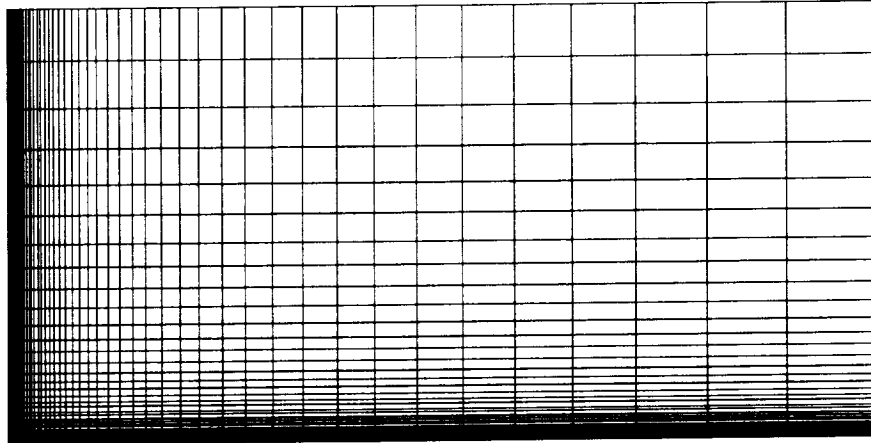


Figure 4.2: Computational grid for the incompressible laminar flat plate case

4.1 Incompressible Laminar Boundary Layer

The flow used for the laminar boundary layer case was constructed such that the Reynolds number was 10000 at the end of the plate, using the freestream density, velocity, and viscosity. The vertical dimension of the flow domain was one half that of the axial dimension. Because the flow solver was developed using the compressible form of the Navier-Stokes equations, the freestream flow was set to correspond to Mach 0.2. Use of a smaller freestream Mach number would substantially slow down the convergence characteristics of the numerical scheme.

Figure 4.2 shows the computational grid used for the calculations with 51 axial points by 51 vertical points. Calculations were initially obtained using this two dimensional grid and a two-dimensional version of the flow solver. Additional calculations were obtained with the three dimensional solver to further validate the implementation of the computational method. For the three-dimensional

calculations, 11 points were used in the spanwise direction to accommodate the three-dimensional flow solver, but no flow development occurs in this direction. The grid was packed to the leading edge in the axial direction such that the grid spacing from the first to second point corresponds to a Reynolds number of 10, again using freestream flow properties. In the vertical direction, the grid was packed to the plate surface such that the grid spacing from the first to second point corresponds to a Reynolds number of 2. A hyperbolic tangent stretching function was used to stretch the grid both in the axial and vertical directions. For the three-dimensional calculations, the grid points were equally spaced in the spanwise direction.

The boundary condition for the flat plate is set to be a no-slip, adiabatic surface such that all of the velocity components are set to zero, and the vertical temperature gradient is zero. At the inflow, the total pressure and total temperature are specified to correspond to Mach 0.2 flow at sea level atmospheric conditions. The static pressure is set at the outflow to also correspond to Mach 0.2 flow at sea level atmospheric conditions. The boundary along the plane at the highest vertical point is modeled as a slip-wall surface, which is also known as a symmetry surface. A boundary condition in which all flow quantities were extrapolated from the interior was also investigated for the top boundary, and produced identical results for that obtained with the slip surface. For the three dimensional calculations, the boundaries along the two extreme spanwise planes were also set as slip surfaces. Because the solutions obtained with the two and three dimensional calculations were found to be nearly identical, only one set of computed results are discussed in the the rest of this section.

The exact solution for the incompressible flat plate boundary layer with constant fluid properties and no pressure gradient was obtained by Blasius [11], and as a result, is known as the Blasius solution. The Blasius solution enables velocity profiles at different axial positions, x to be reduced to a single similarity profile, through the use of a similarity variable, η , defined as:

$$\eta = y \sqrt{\frac{\rho U}{\mu x}} = \frac{y}{x} \sqrt{Re_x} \quad (4.1)$$

The exact solution of Blasius enables the skin friction coefficient, boundary layer thickness, displacement thickness, and momentum thickness to be expressed as a function of axial position.

Skin friction coefficient:

$$C_f = \frac{0.664}{\sqrt{Re_x}} \quad (4.2)$$

Boundary layer thickness:

$$\frac{\delta}{x} = \frac{5}{\sqrt{Re_x}} \quad (4.3)$$

Displacement thickness:

$$\frac{\delta^*}{x} = \frac{1.7208}{\sqrt{Re_x}} \quad (4.4)$$

Momentum thickness:

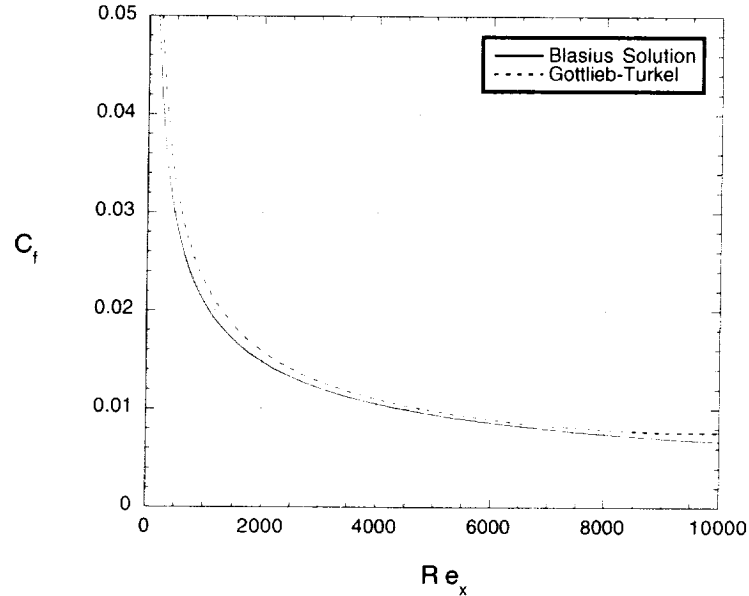


Figure 4.3: Skin friction for incompressible laminar boundary layer

$$\frac{\theta}{x} = \frac{0.664}{\sqrt{Re_x}} \quad (4.5)$$

The calculated skin friction along the flat plate is compared to the expression from the Blasius solution given in equation (4.2) in figure 4.3. The overall agreement between the calculation and the expression from the Blasius solution is good. At the end of the plate, near $Re_x = 10000$, the calculation indicates that the skin friction levels off. This is a numerical effect of the outflow boundary condition which extrapolates the velocity components at the outflow plane from the interior, and indicates that the outflow plane should be downstream of the flow region of interest when such an outflow boundary condition is used.

Comparisons of the calculated velocity profiles are made to the exact solution of Blasius in figure 4.4 at two axial positions corresponding to $Re_x = 2000$ and $Re_x = 5000$. Again, the agreement between the exact solution and the calculated results is close. Comparisons of the calculated boundary layer, displacement, and momentum thicknesses to those obtained from the Blasius solution are shown in figures 4.5, 4.6, and 4.7 respectively.

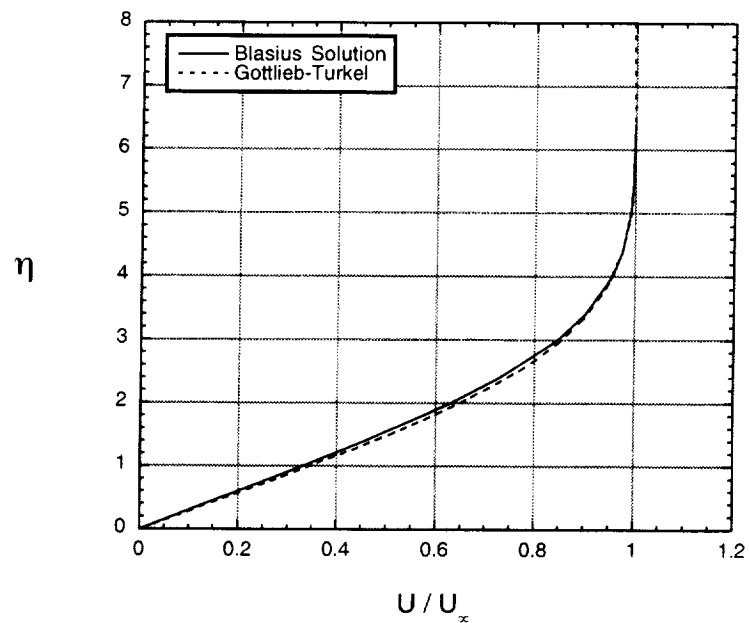
The boundary layer thickness along the flat plate obtained from the calculations was determined to be the distance from the wall where the local axial velocity became 99 percent of the freestream velocity. The displacement and momentum thicknesses were obtained by numerical integration using equations (4.6) and (4.7) respectively:

$$\delta^* = \int_{y=0}^{\infty} \left(1 - \frac{u}{U_{\infty}}\right) dy \quad (4.6)$$

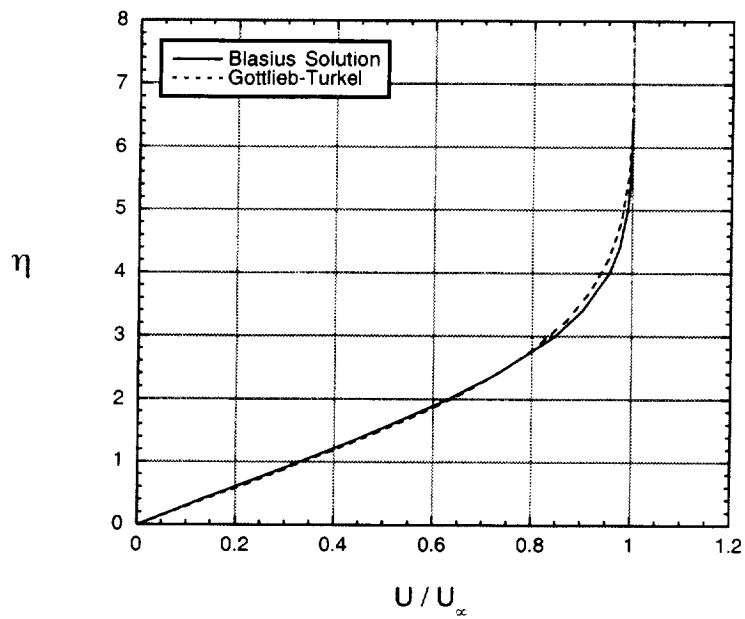
$$\theta = \int_{y=0}^{\infty} \frac{u}{U_{\infty}} \left(1 - \frac{u}{U_{\infty}}\right) dy \quad (4.7)$$

These forms of the displacement and momentum thicknesses are valid for both laminar and turbulent incompressible flows. For compressible flows, the variation in density appears in the two expressions, which will be shown later in the discussion on the compressible boundary layer calculations.

The agreement between the exact Blasius solution and the computed solutions obtained with the Gottlieb-Turkel scheme is very close for the boundary layer thickness and the integral thicknesses. At the end of the plate, $X/L = 1$, all of the three thicknesses flatten in slope. As was the case for the skin friction comparison in



(a) $Re_x = 2000$



(b) $Re_x = 5000$

Figure 4.4: Velocity profiles for incompressible laminar boundary layer

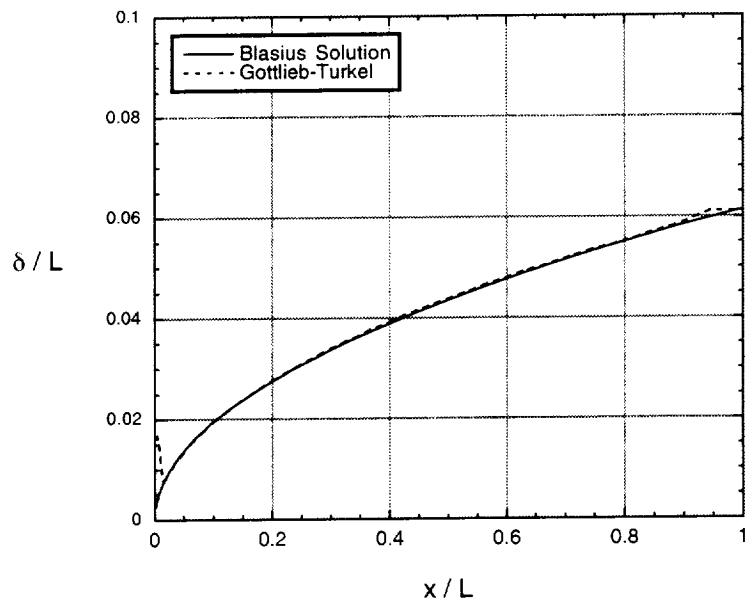


Figure 4.5: Boundary layer thickness for incompressible laminar boundary layer

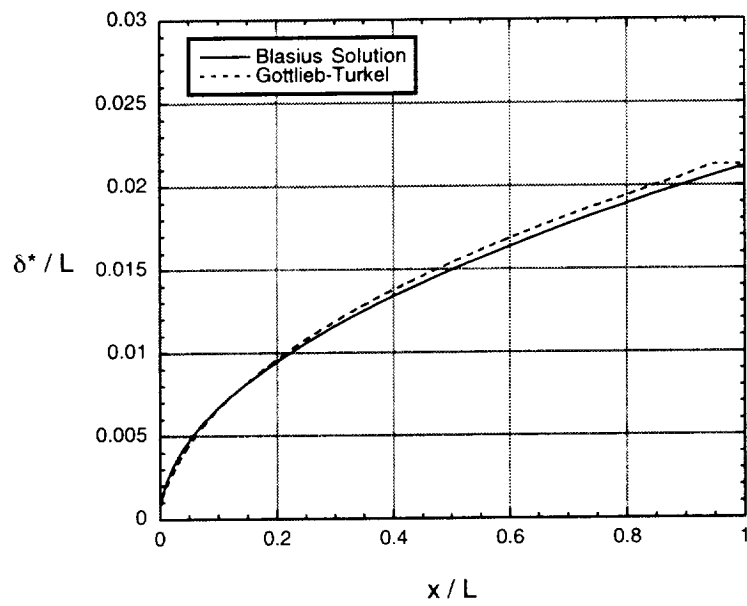


Figure 4.6: Displacement thickness for incompressible laminar boundary layer

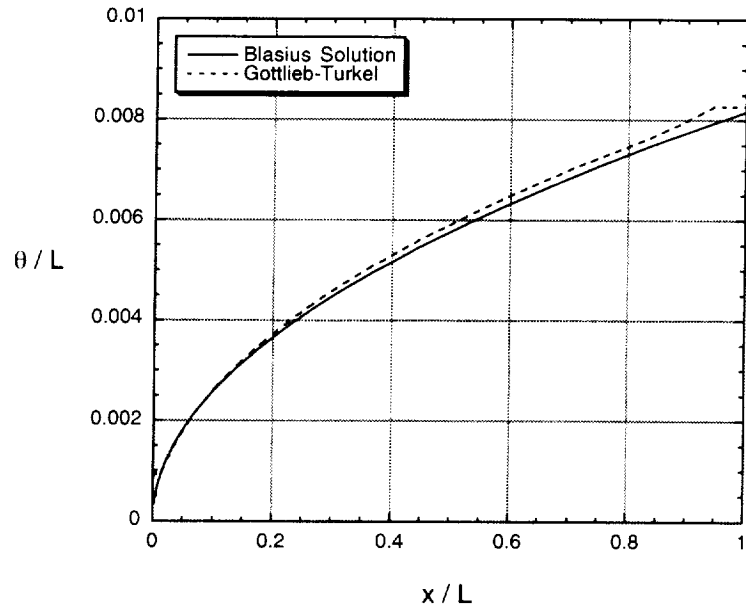


Figure 4.7: Momentum thickness for incompressible laminar boundary layer

figure 4.3, this is due to the outflow boundary condition which extrapolates the velocity components from one point interior to the computational grid.

4.2 Incompressible Turbulent Boundary Layer

The second boundary layer case examined was an incompressible turbulent flow over a flat plate at Mach 0.2. A computational grid having 71 axial points by 71 vertical points was examined with the two-dimensional flow solver. The computational domain extended to a position corresponding to a Reynolds number of 2,000,000. The vertical dimension was equal to 40 percent of the axial dimension. The computational grid, shown in figure 4.8, was packed to the flat plate surface such that the average y^+ of the first point off the wall was set to 2.5. This average y^+

that was employed to construct the computational grid was determined by the following procedure:

The definition of the wall normal coordinate y^+ is:

$$y^+ = \frac{yu_\tau}{\mu_w/\rho_w} \quad (4.8)$$

Expanding the expression for the shear velocity:

$$u_\tau = \sqrt{\frac{\tau_w}{\rho_w}} = \sqrt{\frac{C_f \frac{1}{2} \rho_\infty u_\infty^2}{\rho_w}} \quad (4.9)$$

The expression for (y^+) in equation 4.8 can be rewritten in terms of the local skin friction coefficient and flow properties at the wall and in the freestream:

$$y^+ = \sqrt{\frac{C_f}{2}} \frac{\rho_\infty U_\infty y}{\mu_\infty} \left(\sqrt{\frac{\rho_w}{\rho_\infty}} \frac{\mu_\infty}{\mu_w} \right) \quad (4.10)$$

For this incompressible flat plate boundary layer case, the flow properties are constant through the flow such that $\rho_w = \rho_\infty$ and $\mu_w = \mu_\infty$. Using a skin friction coefficient that is characteristic of the flow, in this case $C_f \approx 0.003$, and the freestream conditions, equation (4.10) can be used to calculate a characteristic or “average” y^+ for the grid spacing at the wall. In the axial direction, the computational grid was packed to the leading edge such that the initial spacing was $\Delta x^+ = 75$ using the same method used to calculate the average y^+ . A hyperbolic tangent stretching function was used to stretch the grid both in the axial and vertical directions, as was done for the laminar flat plate case.

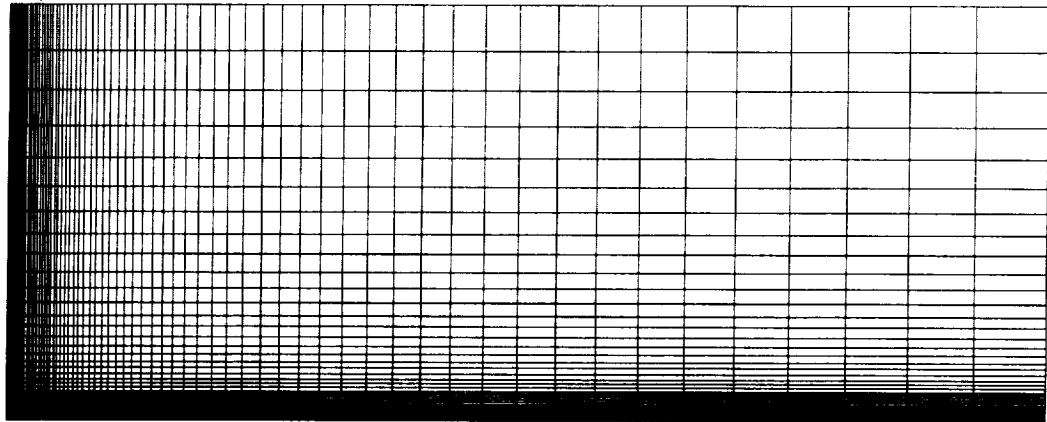


Figure 4.8: Computational grid for the incompressible turbulent flat plate case

This incompressible turbulent boundary layer flow was calculated using the same RANS approach as that for the laminar boundary layer, with identical boundary conditions, except that the Cebeci-Smith turbulence model was also employed. The wall function approach was not used here. With the grid packed tightly to the plate surface and the first point off the wall placed well within the laminar sublayer, the Cebeci-Smith turbulence model was integrated to the wall.

Unlike the laminar boundary layer, an exact solution is not available for this turbulent flow. As a result, the computed results are compared to a benchmark experimental data set of Wieghardt and Tillman [112] for the wall skin friction coefficient and velocity profiles. Correlations for the boundary layer, displacement and momentum thicknesses obtained by Schlichting [90] are used for comparison to the computed results.

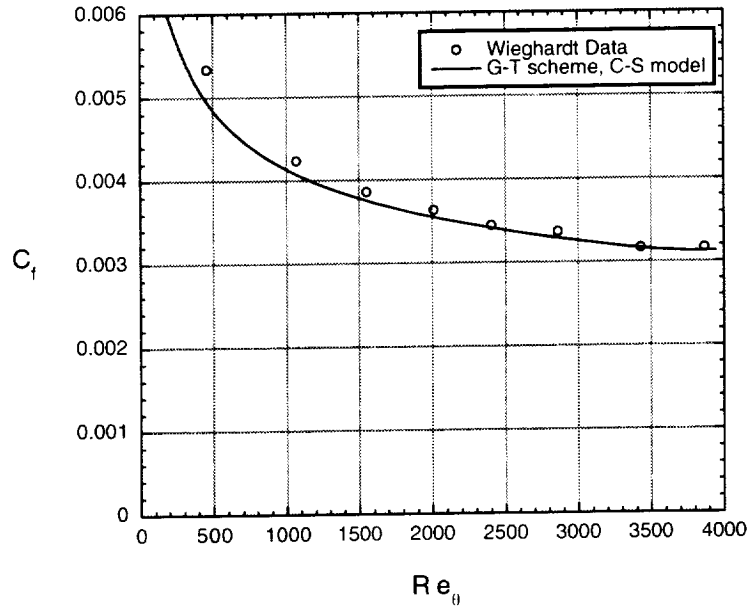


Figure 4.9: Skin friction for the incompressible turbulent boundary layer

A comparison of the calculated skin friction with the data of Wiegardt and Tillman is provided in figure 4.9. The calculated velocity profile at a location along the plate corresponding to a Reynolds number based on axial position of 1,050,000 is compared to experimental measurements in figure 4.10. Figure 4.11 provides a comparison of the same results for the velocity profile using wall coordinates. Overall, the agreement between the calculated boundary layer results and the experimental data of Wiegardt and Tillman is very close.

A comparison of the calculated boundary layer, displacement, and momentum thicknesses to correlations provided by Schlichting [90] are shown in figures 4.12, 4.13, and 4.14 respectively. The correlations for these thicknesses are as follows:

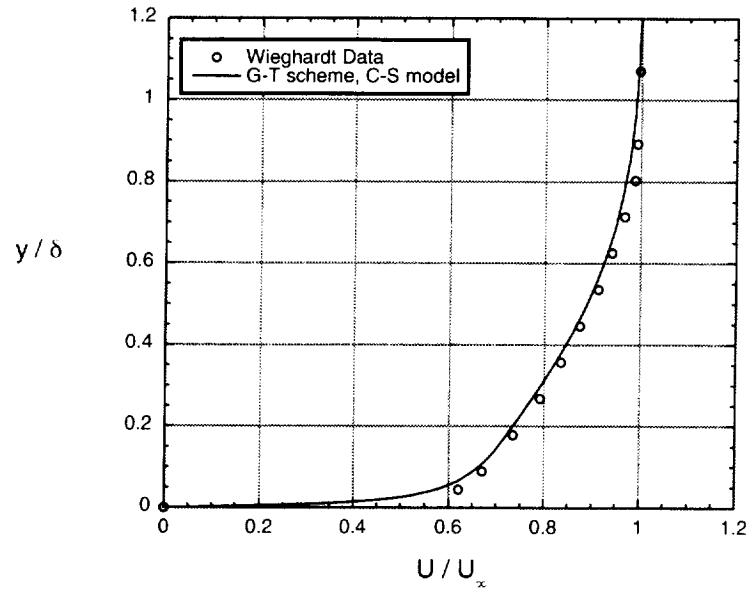


Figure 4.10: Velocity profile for the incompressible turbulent boundary layer at $Re_x = 1,050,000$

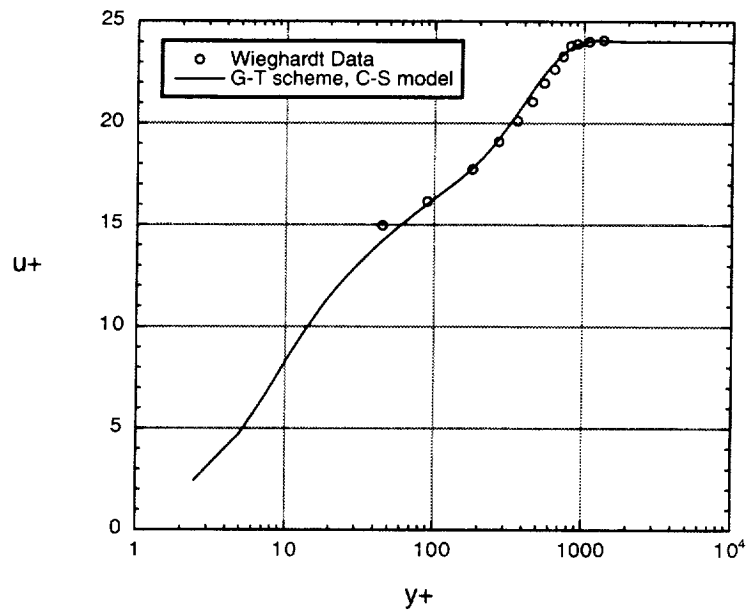


Figure 4.11: Velocity profile for the incompressible turbulent boundary layer at $Re_x = 1,050,000$ using wall coordinates

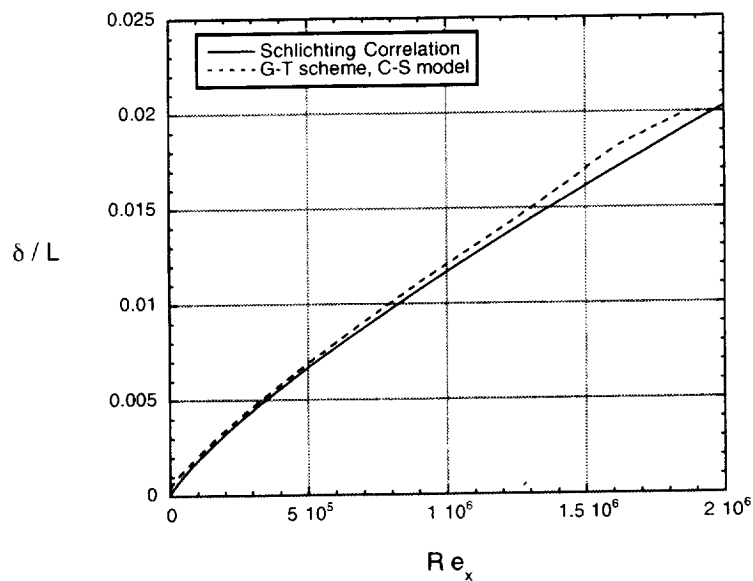


Figure 4.12: Boundary layer thickness for incompressible turbulent boundary layer

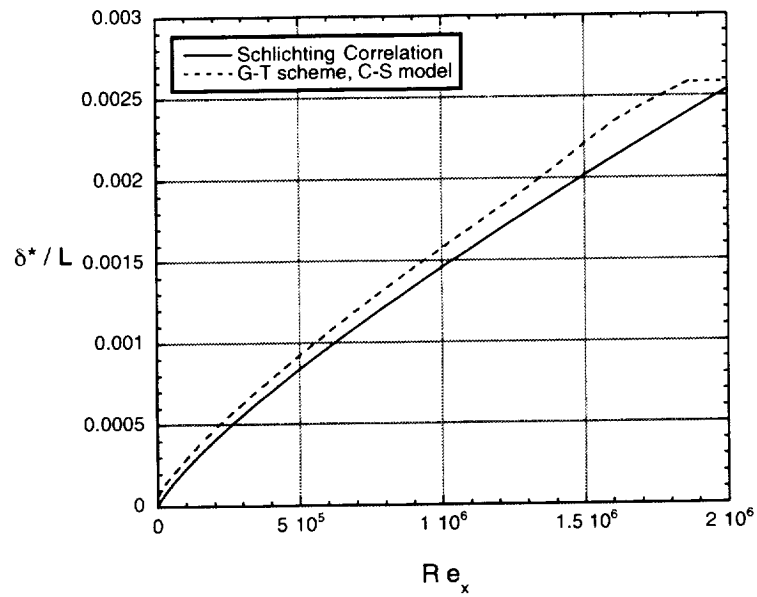


Figure 4.13: Displacement thickness for the incompressible turbulent boundary layer

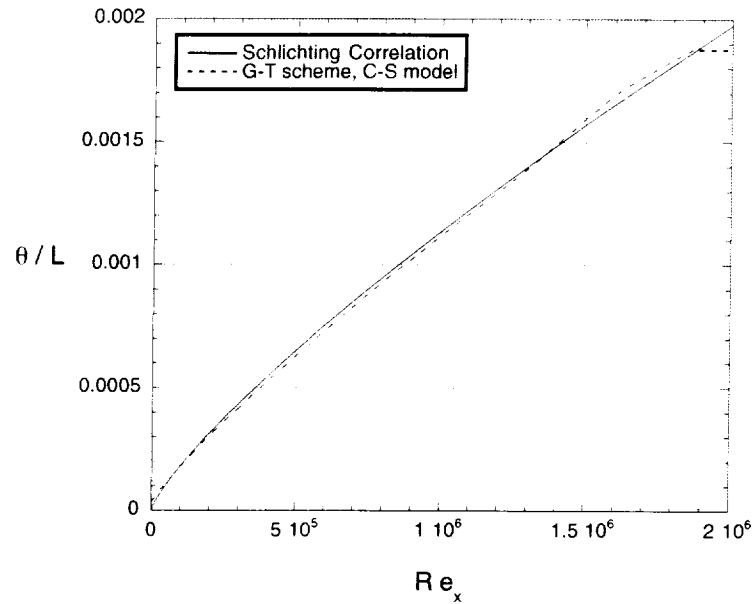


Figure 4.14: Momentum thickness for the incompressible turbulent boundary layer

Boundary layer thickness:

$$\frac{\delta}{x} = 0.37 Re_x^{-\frac{1}{5}} \quad (4.11)$$

Displacement thickness:

$$\delta^* = \frac{1}{8} \delta \quad (4.12)$$

Momentum thickness:

$$\theta = \frac{7}{72} \delta \quad (4.13)$$

The correlations provided in equations (4.11 - 4.13) are derived assuming the velocity profile for an incompressible turbulent flow over a smooth surface can be represented by a $\frac{1}{7}$ -th power law profile. That is:

$$\frac{u}{U_\infty} = \left(\frac{y}{\delta}\right)^{\frac{1}{7}} \quad (4.14)$$

The agreement between the correlations and the computed solutions obtained with the Gottlieb-Turkel scheme and Cebeci-Smith turbulence model is good. Again near the end of the plate, the outflow boundary condition extrapolates the components of the velocities such that the three thicknesses flatten between the next to last grid point in the axial direction and the outflow boundary. This behavior does not adversely affect the rest of the boundary layer development upstream of the outflow boundary as indicated by figures 4.12 - 4.14.

4.3 Compressible Turbulent Boundary Layers

In this section, two compressible supersonic boundary layers are investigated to further validate the RANS approach. The two boundary layers selected were the two flows entering the mixing layer to be examined with the hybrid RANS/LES method. The particular mixing layer is one of the experiments of Goebel and Dutton [34–36] referred to as Case 2 in these references. Their experimental configuration is depicted by the schematic shown in figure 1.1. Upstream of the mixing layer, the flow on the top half of the splitter plate is for a Mach 1.91 stream and a total temperature of 578 K. On the bottom half of the splitter plate, a boundary layer grows for a Mach 1.36 stream at a total temperature of 295 K. The Goebel-Dutton experiments provide details of the boundary layer entering the

mixing region including measurements of the boundary layer, displacement, and momentum thicknesses. More details of the experimental configuration, flow conditions, and data collection, particularly regarding the mixing section, will be provided in chapter 5.

For each of the supersonic boundary layers, both the wall-integration and wall-function approaches are investigated. As mentioned in chapter 2, the motivation for employing the wall function approach in conjunction with the Cebeci-Smith turbulence model was to enable a continuous computational grid from the wall bounded RANS regions into the mixing layer that is then calculated using the LES part of the hybrid approach. Comparison of the wall-function approach to the more standard wall-integration approach and the compressible boundary layer correlations determines the capability of the wall-function implementation to accurately provide the mean flow characteristics of the incoming boundary layer.

In the previous section, calculated results were compared to benchmark experimental data for the incompressible turbulent boundary layer. Although the measurements of the boundary layer, displacement thickness, and momentum thicknesses at the trailing edge of the wall bounded regions in the Goebel-Dutton experiments make them one of the better documented mixing layer data sets, other details of the boundary layer developments are not provided.

As a result, well established correlations for the skin friction coefficient, velocity profiles, boundary layer thickness, and integral thicknesses are used to investigate the details of the boundary layer development for the two particular supersonic

flows here. The calculated skin friction coefficient is compared to a combined correlation, that is referred to here as the Mager-Schlichting correlation. In reference [90], Schlichting provided the following expression for the skin friction coefficient for an incompressible flat plate with turbulent flow from the leading edge:

$$C_f = .0592 Re_x^{-\frac{1}{5}} \quad (4.15)$$

In reference [63], Mager provides a correction to equation (4.15) for the skin friction coefficient in compressible turbulent flow:

$$\frac{C_f}{C_f^{inc.}} = \left(\frac{T_\infty}{T_t} \right)^{.456} \quad (4.16)$$

To evaluate the other boundary layer characteristics such as velocity profiles, boundary layer thickness, and the integral thicknesses, the method developed by Tucker [105] is used here. Tucker provides a power-law relationship for the velocity profile in turbulent compressible flow that is similar to the incompressible form given in equation 4.14. Unlike the incompressible form which assumes a constant exponent of 7, the compressible form uses a variable exponent:

$$\frac{u}{U_\infty} = \left(\frac{y}{\delta} \right)^{\frac{1}{N}} \quad (4.17)$$

where the exponent N is given by:

$$N = (Re_{am})^{\frac{1}{14}} \quad (4.18)$$

The Reynolds number Re_{am} is based on the length of the boundary layer development. The subscript *am* refers to the procedure of evaluating all fluid properties at the arithmetic mean of the wall temperature and the freestream temperature. Tucker shows that a solution of the Karman momentum equation results in:

$$\theta = \frac{7}{6} K \left[\frac{(1 + m^2)^2}{M \left(1 + \frac{m^2}{2} \right)^5} \right]^{\frac{1}{7}} x^{\frac{6}{7}} \quad (4.19)$$

The parameter K is given by:

$$K = 0.0131 \left(\frac{\mu_o}{\rho_o a_o} \right)^{\frac{1}{7}} \quad (4.20)$$

where μ_o , ρ_o , and a_o are the dynamic viscosity, density, and speed of sound, respectively, all evaluated at the freestream total temperature.

Finally, the Mach number parameter, m^2 , is given by:

$$m^2 = \frac{M^2}{5} \quad (4.21)$$

Tucker provides further integral relationships between the momentum thickness, θ , given by equation 4.19 and the boundary layer thickness, δ , the displacement thickness, δ^* . While the ratios θ/δ and δ^*/δ are assumed to be nearly constant for incompressible flows, as indicated by equations 4.12 and 4.13, Tucker shows them to be a function of the freestream Mach number and the velocity profile parameter, N . Reference [105] provides extensive tables from which δ , δ^* , and θ may be obtained.

Following the validation of the RANS approach for the Mach 1.91 and Mach 1.36 cases, the objectives will be to provide boundary layers to the mixing section in the hybrid RANS/LES calculations that match the mean flow properties measured in the Dutton-Goebel experiment. As a result, physical dimensions will be used to describe the computational grids and the calculated thicknesses δ , δ^* , and θ in the following two sections.

4.3.1 Mach 1.91 Flat Plate Flow

The computational grid for the wall-integration case is shown in figure 4.15 and the grid for the wall function case is shown in figure 4.16. Both grids extended 300 mm in the axial direction and 150 mm in the vertical direction. In addition, both grids used 141 points in the axial direction and 141 points in the vertical direction. The wall-integration grid was packed to the wall such that the first grid spacing was 0.006 mm , corresponding to an average y^+ of 2.5, using equation (4.8). The wall function grid had the first point placed at 0.05 mm , corresponding to an average y^+ of approximately 20. This wall spacing was chosen for use with the wall-function grid so that the initial grid spacing at the wall was exactly 1/10th of the splitter plate thickness in the experiment. This grid spacing could then be continued into the mixing region, with 10 points spaced equally in the vertical direction at the base of the splitter. In the axial direction, both the wall-integration and wall-function grids were packed to leading and trailing edges with spacings at the two ends set to 0.10 mm , corresponding to 1/5th of the splitter base thickness.

The wall boundary condition for the calculations was set to be an adiabatic no-slip surface and the extreme vertical boundary was set as a slip surface, as was done for

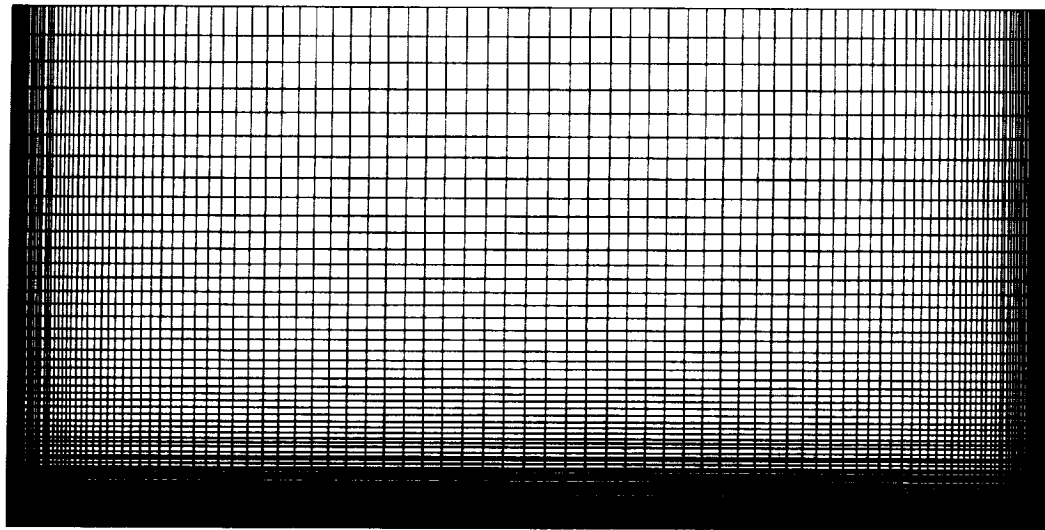


Figure 4.15: Computational grid for the Mach 1.91 turbulent flat plate case using the wall-integration method

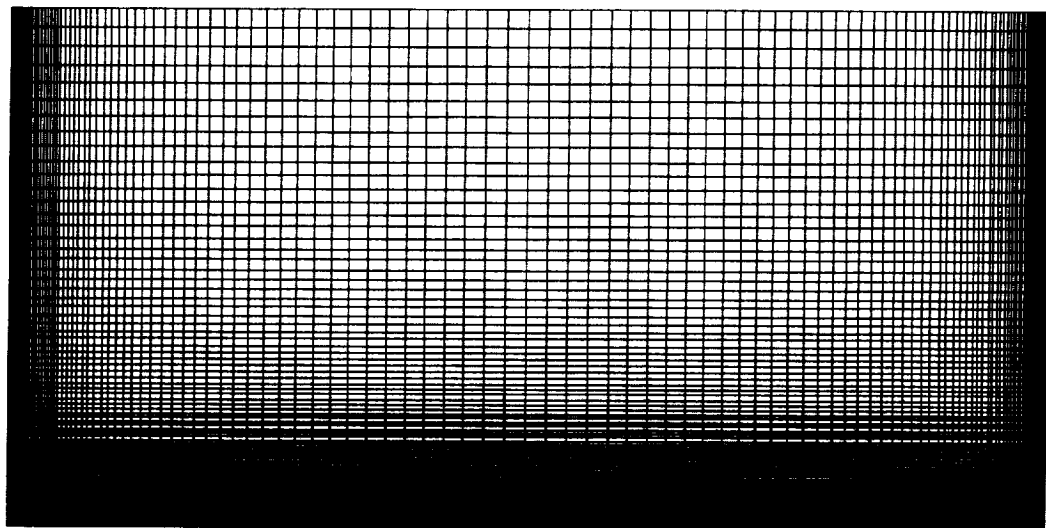


Figure 4.16: Computational grid for the turbulent Mach 1.91 flat plate case using the Ota-Goldberg wall function

the incompressible turbulent boundary layer. For this supersonic boundary layer, however, the inflow condition was fixed and the outflow condition extrapolated quantities.

The skin friction coefficient along the flat plate obtained from the two computed solutions is compared to the Mager-Schlichting correlation in figure 4.17. The wall-integration skin friction results were obtained by directly evaluating the shear stress at the wall, since the grid was packed to the wall surface with the first point off the wall placed in the laminar sublayer. For the wall-function case, however, the shear velocity that is solved with an iterative procedure within the Ota-Goldberg wall-function was used to calculate the skin friction coefficient along the flat plate. The agreement of the two solutions with the Mager-Schlichting correlation is good, with the wall-integration approach providing closer agreement.

The calculated velocity profiles at a location along the plate corresponding to a Reynolds number based on axial position of 4,000,000 is compared to results of the Tucker method in figure 4.18. The profile obtained with the Tucker correlation was obtained by using equation (4.17) with the exponent N given in equation (4.18) evaluated to be 6.275 at this axial position. In figure 4.19 the velocity profile at the same location expressed in wall coordinates, u^+ and y^+ is compared to the White-Christoph compressible law of the wall given in equation (2.88). Figures 4.18 and 4.19 indicate that both the wall-integration and wall-function calculations provide good agreement with analytical expressions developed to evaluate compressible turbulent boundary layer characteristics.

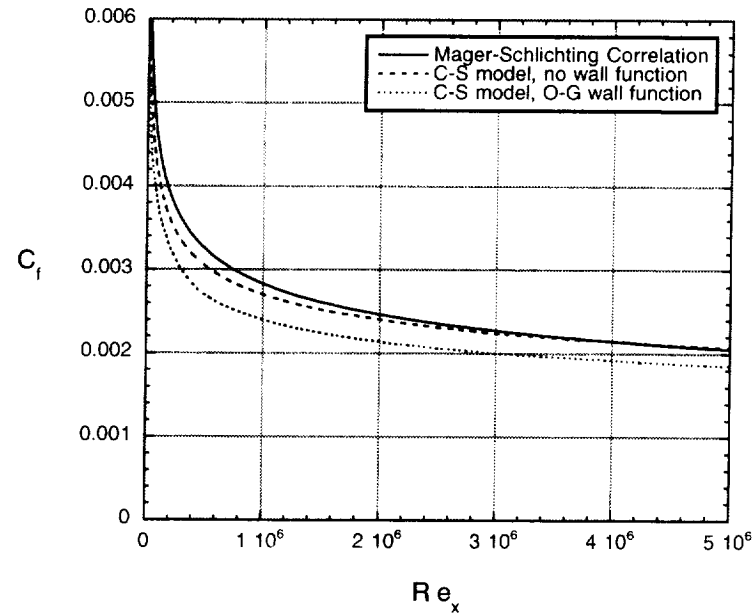


Figure 4.17: Skin friction for the Mach 1.91 turbulent boundary layer

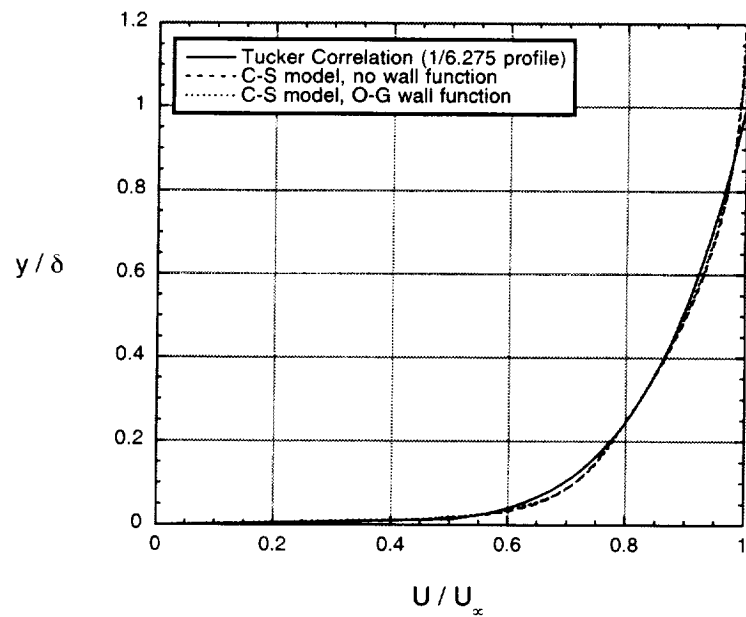


Figure 4.18: Velocity profile for the Mach 1.91 turbulent boundary layer at $Re_x = 4,000,000$

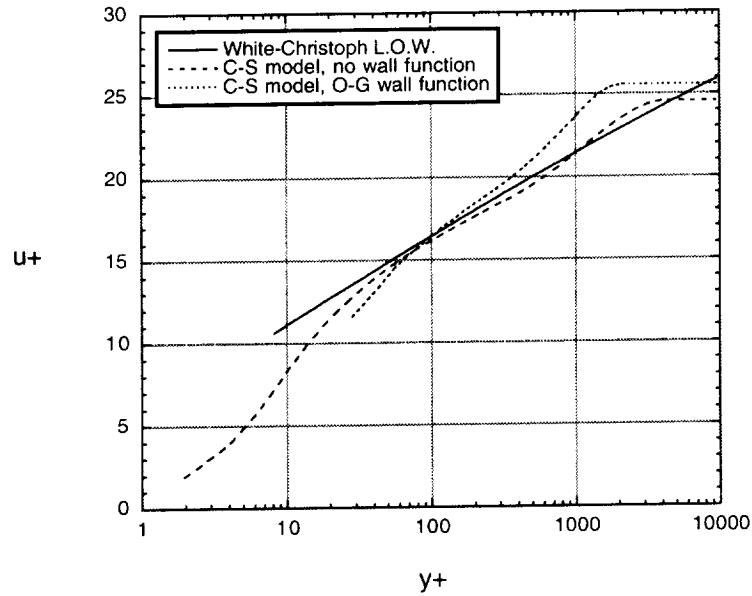


Figure 4.19: Velocity profile for the Mach 1.91 turbulent boundary layer at $Re_x = 4,000,000$ using wall coordinates

The calculated boundary layer, displacement, and momentum thicknesses are compared to results obtained using the Tucker method in figures 4.20, 4.21, and 4.22 respectively. The boundary layer thickness along the turbulent compressible flat plate was determined in the same manner used for the incompressible turbulent case, by finding the distance from the wall where the local axial velocity became 99 percent of the freestream velocity. The displacement and momentum thicknesses for the compressible case differ from the incompressible case in that the density is involved in the integral expressions. These two integral quantities are defined for the compressible case in equations (4.22) and (4.23):

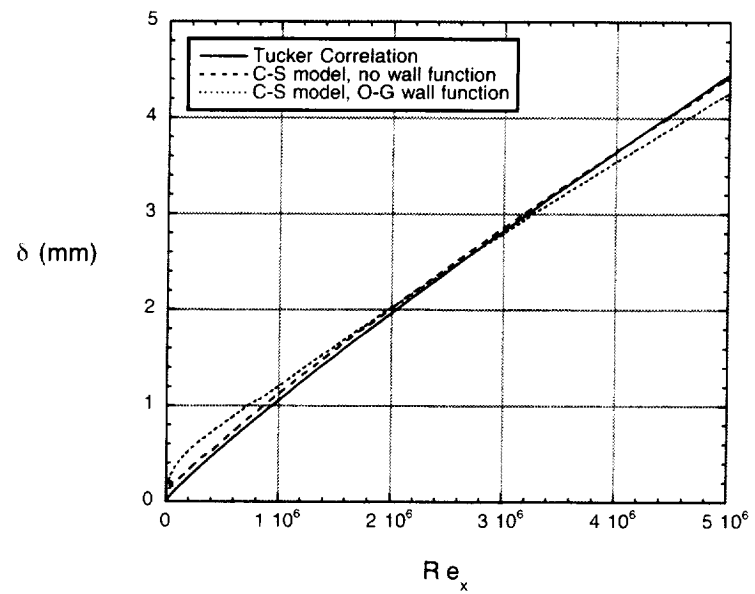


Figure 4.20: Boundary layer thickness for the Mach 1.91 turbulent boundary layer

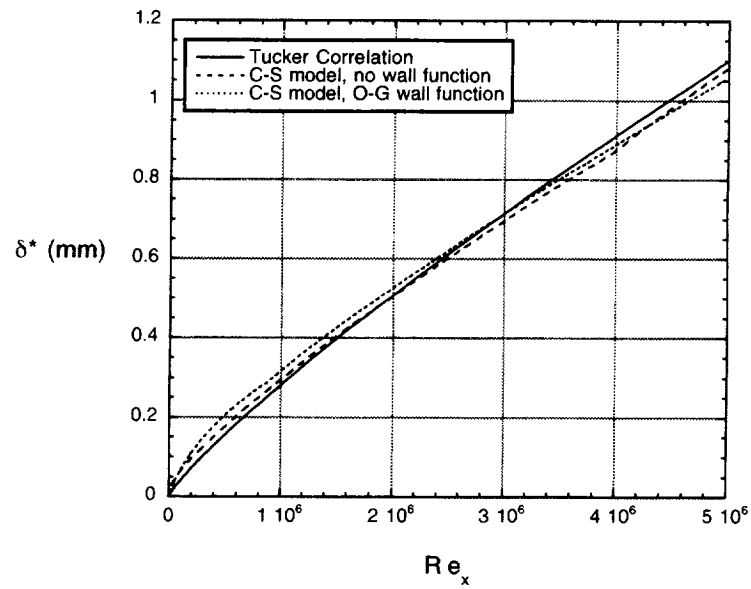


Figure 4.21: Displacement thickness for the Mach 1.91 turbulent boundary layer

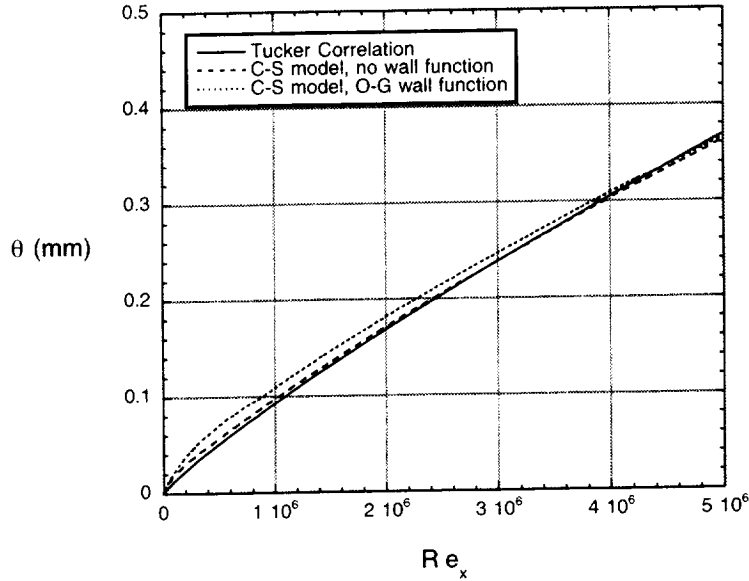


Figure 4.22: Momentum thickness for the Mach 1.91 turbulent boundary layer

$$\delta^* = \int_{y=0}^{\infty} \left(1 - \frac{\rho u}{\rho_{\infty} U_{\infty}} \right) dy \quad (4.22)$$

$$\theta = \int_{y=0}^{\infty} \frac{\rho u}{\rho_{\infty} U_{\infty}} \left(1 - \frac{u}{U_{\infty}} \right) dy \quad (4.23)$$

The three measures of the boundary layer growth shown in figures 4.20 - 4.22 again indicate close agreement with results obtained using the Tucker analysis. The greatest discrepancy in these results is for the wall-function solution near the leading edge of the plate. This is a result of the wall-function grid having significantly fewer points than the wall-integration grid near the wall to resolve the thin boundary layer at the leading edge. Further downstream, however, the wall-function approach provides similar agreement to the Tucker correlation.

4.3.2 Mach 1.36 Flat Plate Flow

The computational grids used for the wall-integration and wall function cases are shown in figures 4.23 and 4.24 respectively. The construction of these grids was similar to that performed for the Mach 1.91 calculations, with the exception of the axial dimension being shorter for these Mach 1.36 calculations. This was done because the Mach 1.36 boundary layer thickness in the Dutton-Goebel experiment measured at the beginning of the mixing section was smaller than the Mach 1.91 boundary layer, as will be discussed in the next chapter. The grids extended 200 mm in the axial direction and 150 mm in the vertical direction. Both grids used 141 points in the axial direction by 141 points in the vertical direction. The grid for the wall-integration case was packed to the wall such that the first grid spacing was 0.006 mm , corresponding to an average y^+ of approximately 3.0, again using equation (4.8). The wall function grid had the first point placed at 0.05 mm , corresponding to an average y^+ of approximately 25. Both grids were packed in the axial direction to leading and trailing edges with spacings at the two ends set to 0.10 mm , corresponding to 1/5th of the splitter base thickness. The boundary conditions used for these Mach 1.36 cases were the same as those used for the Mach 1.91 case, with the only difference being that a Mach 1.36 flow was fixed at the inflow here.

The skin friction coefficient obtained from the two computed solutions is compared to the Mager-Schlichting correlation in figure 4.25. The agreement of the two solutions with the correlation is nearly as close as that for the Mach 1.91 case, with the directly calculated shear stress from the wall-integration approach providing

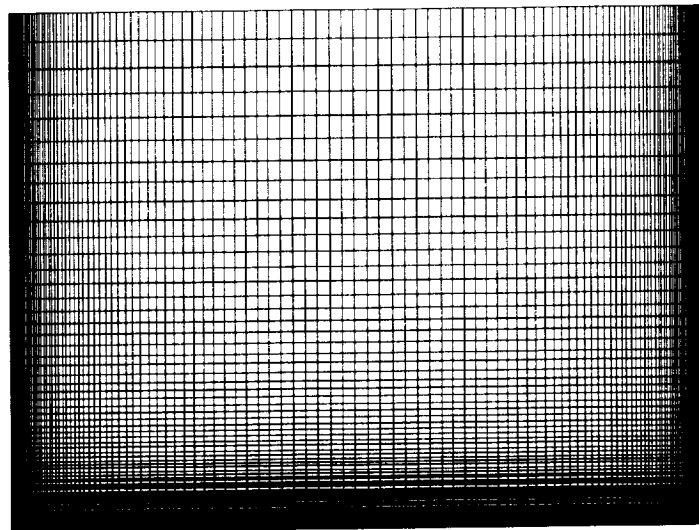


Figure 4.23: Computational grid for the turbulent Mach 1.36 flat plate case using the wall-integration method

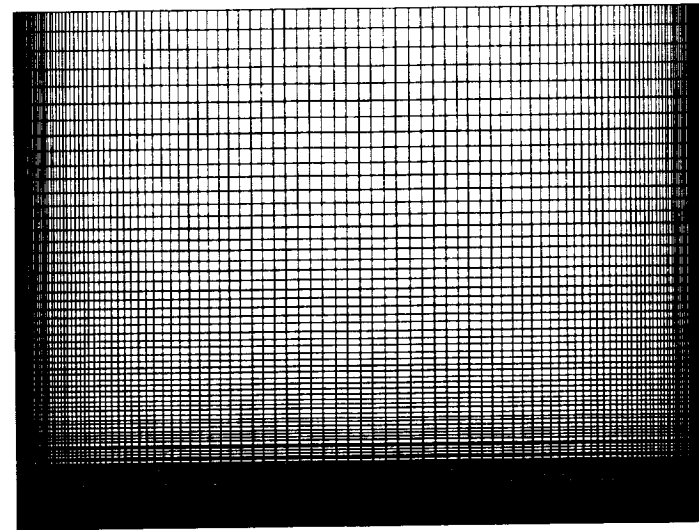


Figure 4.24: Computational grid for the turbulent Mach 1.36 flat plate case using the Ota-Goldberg wall function

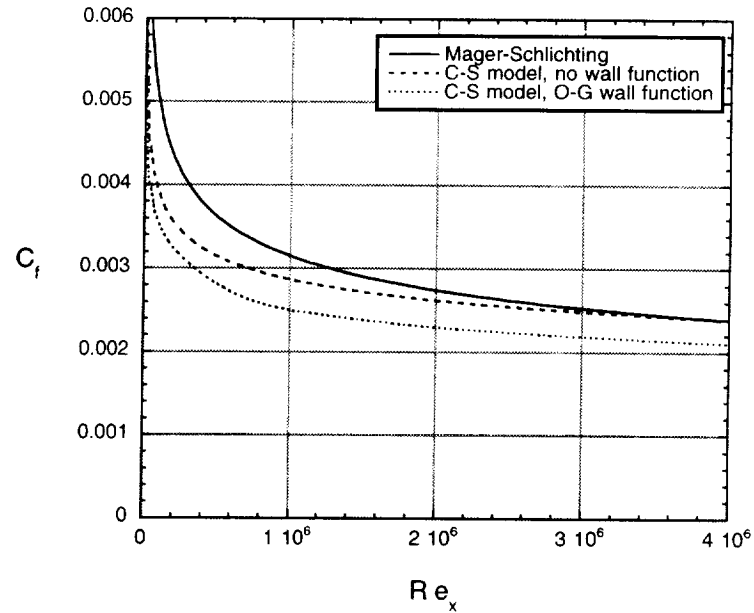


Figure 4.25: Skin friction for the Mach 1.36 turbulent boundary layer

closer agreement to the correlation than the wall-function approach. The calculated velocity profiles at a location along the plate corresponding to a Reynolds number based on axial position of 4,000,000 is compared to results of the Tucker method in figure 4.26. For the Mach 1.36 boundary layer at this location, the Tucker analysis indicates that the velocity profile exponent is 6.370. In figure 4.27 the velocity profile expressed in wall coordinates, u^+ and y^+ is compared to the White-Christoph compressible law of the wall profile. In figures 4.26 and 4.27, both the wall-integration and wall-function calculations indicate acceptable agreement with the analytical expressions.

Finally, the calculated boundary layer, displacement, and momentum thicknesses are compared to the Tucker method in figures 4.28, 4.29, and 4.30 respectively. The

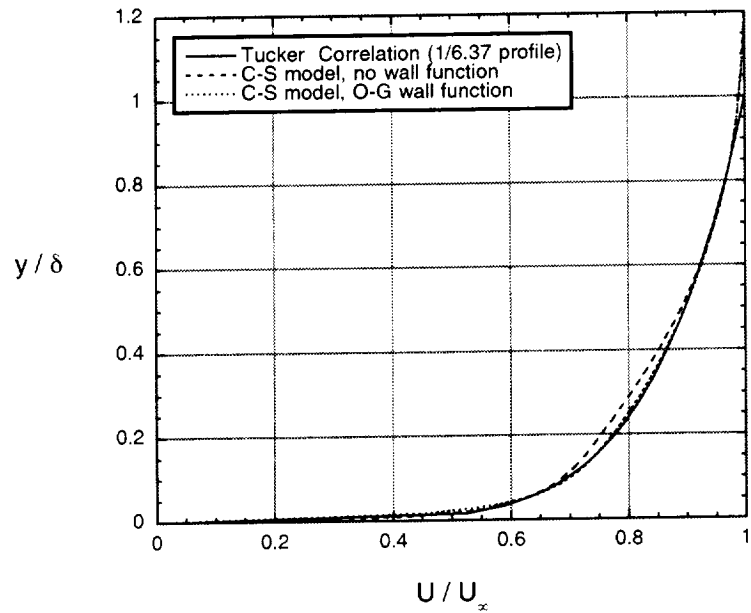


Figure 4.26: Velocity profile for the Mach 1.36 turbulent boundary layer at $Re_x = 4,000,000$

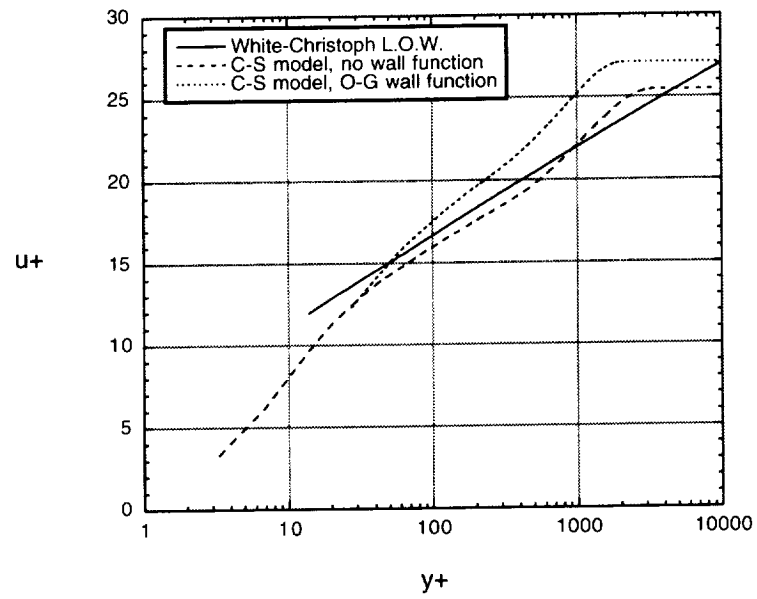


Figure 4.27: Velocity profile for the Mach 1.36 turbulent boundary layer at $Re_x = 4,000,000$ using wall coordinates

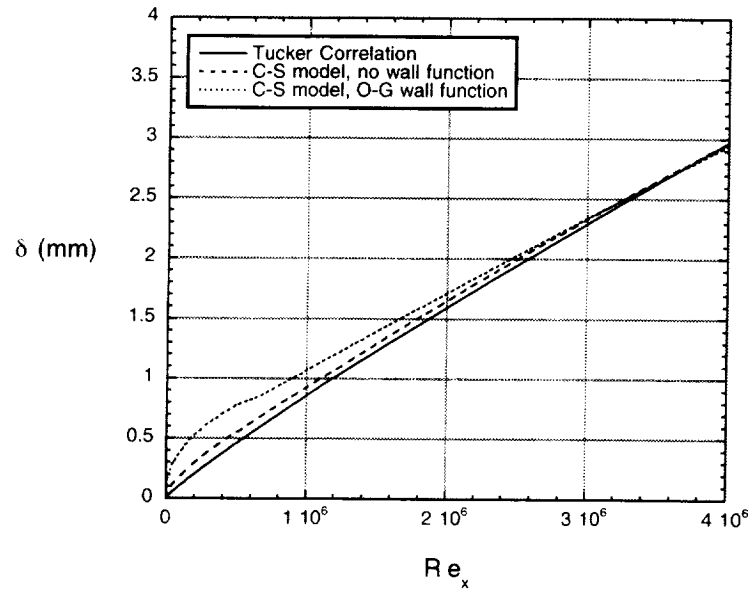


Figure 4.28: Boundary layer thickness for the Mach 1.36 turbulent boundary layer

agreement of the solutions with the Tucker correlation is good, although the agreement is not as close as for the Mach 1.91 case. The wall-function solution again indicates the largest discrepancy near the leading edge of the plate where the number of grid points available to resolve the thin boundary layer is low. The discrepancy is minimized further downstream, where the boundary layer becomes thicker.

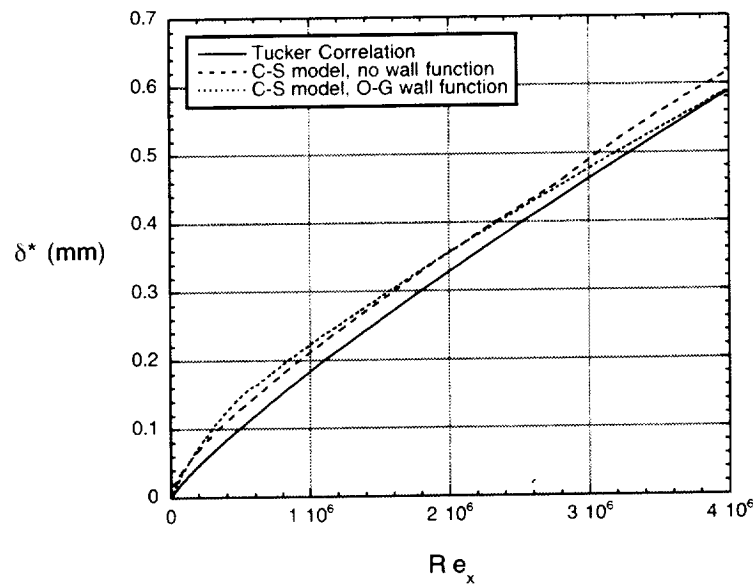


Figure 4.29: Displacement thickness for the Mach 1.36 turbulent boundary layer

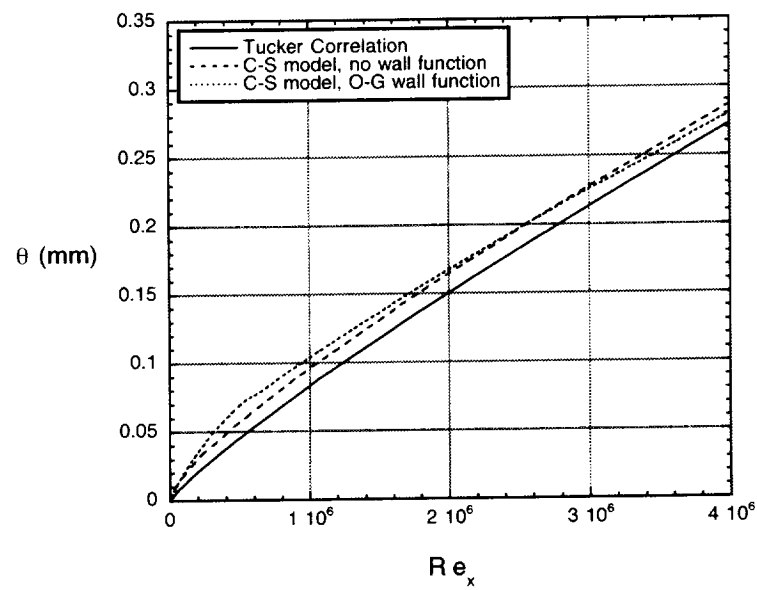


Figure 4.30: Momentum thickness for the Mach 1.36 turbulent boundary layer

CHAPTER 5

TWO DIMENSIONAL MIXING LAYER CALCULATIONS

Two dimensional calculations with the hybrid RANS-LES method were performed for a benchmark compressible mixing layer experiment and the results are described in this chapter. While true LES simulations require computations in three spatial directions, it is useful to compare two dimensional calculations to investigate effects of the RANS-LES interface region, axial grid resolution, and boundary conditions. The results of three dimensional calculations are presented in chapter 6 for the same experimental configuration.

In this chapter, details of the experimental configuration and operating conditions are provided in section 5.1. Construction of the computational model is provided in 5.2. Two-dimensional calculations investigating axial grid density effects are presented in section 5.3. Finally, calculations which investigate the splitter plate thickness and mixing section wall placement are presented in section 5.4.

5.1 Experimental Configuration

The flow that is the focus of the hybrid method calculations is a two-stream, turbulent planar mixing layer that was examined in the experiments of Goebel and

Dutton [34-36]. A simplified schematic of their experimental configuration provided in figure 5.1 shows that two isolated air streams, in which boundary layers develop over a splitter plate surface, are brought together into a constant area mixing section. In all of their experiments, the higher speed primary stream occurred over the top surface of the splitter plate. The top stream enters the mixing section axially, while the bottom stream enters the mixing section at an angle of 2.5 degrees. The splitter plate thickness has a base height of 0.5 mm at the trailing edge. Upstream of the straight sections for the two isolated flows shown in figure 5.1, contoured nozzle blocks were used to provide the supersonic flows with nearly uniform exit flow conditions.

The mixing section height was 48 mm, and the overall length of the mixing section available for flowfield measurements was 500 mm. The width of the mixing section was 96 mm, and as a result, the mean flow development could be considered two-dimensional. This was also verified in the experiment. The divergence angle of the lower and upper walls of the mixing section were adjusted in each experiment with two incoming supersonic flows, to account for boundary layer growth along these two surfaces and to effectively remove any streamwise pressure gradient.

Single component LDV measurements of turbulence intensities in the upstream flows taken 2 mm upstream of the splitter plate trailing edge indicated that incoming boundary layers were turbulent for all cases. These LDV measurements were also used to calculate the boundary layer, displacement, and momentum thicknesses of the two streams as they enter the mixing section. This makes the Goebel-Dutton experiments one of the more thoroughly documented benchmark

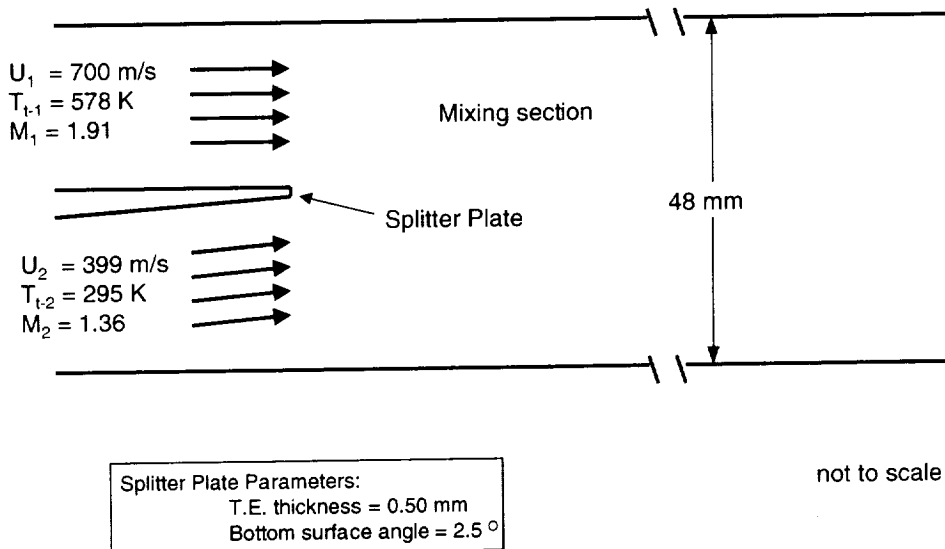


Figure 5.1: Schematic of Goebel-Dutton mixing layer experiment

data sets available for compressible mixing layers. In the mixing region, a two-component LDV system was used to measure the axial and transverse velocities. In addition, a Schlieren system with a 20 ns pulse duration was used to obtain nearly instantaneous snapshots of the mixing layer.

Goebel and Dutton examined seven cases using this experimental configuration. This work investigates their case 2 experiment. The operating conditions of the two streams in case 2 are provided in table 5.1. The two supersonic flows were matched in static pressure at the beginning of the mixing section (end of the splitter plate).

	top flow	bottom flow
<i>Mach No.</i>	1.91	1.36
$U(m/s)$	700	399
$T_t(K)$	578	295
$T(K)$	334	215
$a(m/s)$	366	293
$P(kPa)$	49	49
$\rho(kg/m^3)$	0.51	0.79
$\delta(mm)$	2.9	2.5
$\delta^*(mm)$	0.90	0.44
$\theta(mm)$	0.29	0.21

Table 5.1: Flow conditions for case 2 of the Goebel-Dutton experiments

5.2 Two Dimensional Computational Modeling

The development of the computational model began by using the results of the Mach 1.91 and Mach 1.36 boundary layer simulations discussed in chapter 4. Specifically, the wall-function solutions were examined, because the computational grids utilized in conjunction with the wall-function approach were constructed to enable a continuous grid into the mixing region for use with the hybrid RANS-LES solver. The objective was to construct two RANS regions that would provide boundary layer quantities δ , δ^* , and θ that nearly matched those measured in the experiment, and shown in table 5.1. Because it would be virtually impossible to match all of three quantities exactly, the momentum thickness θ was chosen as the key boundary layer parameter to match the computations with the experiment. The momentum thickness represents the mean momentum deficit entering the mixing section and is fundamental to the downstream mixing layer behavior.

	Goebel-Dutton Experiment	Wall-Function Calculations
$\delta_{1.91}(mm)$	2.9	3.2
$\delta_{1.91}^*(mm)$	0.90	0.82
$\theta_{1.91}(mm)$	0.29	0.29
$\delta_{1.36}(mm)$	2.5	2.3
$\delta_{1.36}^*(mm)$	0.44	0.44
$\theta_{1.36}(mm)$	0.21	0.21

Table 5.2: Comparison of boundary layer quantities at splitter plate trailing edge

While the comparison of calculated quantities to the Tucker theory in section 4.3 was performed to verify the RANS method against well established correlations, the objective here was to determine the axial length of plate needed for the Mach 1.91 and Mach 1.36 boundary layers to reach the same state as those measured in the Goebel-Dutton experiment. Examining the Mach 1.91 boundary layer first, table 5.1 indicates that the momentum thickness for this stream was measured as 0.29 *mm* at the trailing edge of the splitter plate. For the wall function calculations discussed in section 4.3, the momentum thickness reached 0.29 *mm* at a Reynolds number of 3,540,000 (see figure 4.22), corresponding to an axial position of 198 *mm* from the leading edge of the plate. The other boundary layer quantities obtained from the calculations are also in close agreement with the Goebel-Dutton measurements, as shown in table 5.2.

The next step was to construct a new computational grid. The axial domain was shortened to 198 *mm* while retaining the same number (141) of axial grid points. The grid stretching was modified to accommodate the shorter domain while

maintaining the initial and terminal grid spacings. The vertical domain was reduced to 23.75 mm to exactly match the height of the Mach 1.91 stream in the experiment. The vertical domain of the original grid reached 23.75 mm at the 94th grid point in the vertical direction, so the first 94 points from the original grid were used in the modified grid. Calculations obtained with this 141×94 point, 198 mm by 23.75 mm grid provided boundary layer quantities identical to that of the original 141×141 grid, further validating the grid independent characteristics of the RANS method.

A similar procedure was used for the Mach 1.36 boundary layer. Table 5.1 indicates that the momentum thickness for this stream was 0.21 mm at the splitter trailing edge. Examination of the wall-function solution obtained for the Mach 1.36 boundary layer in section 4.3 revealed that the momentum thickness became 0.21 mm at an axial position of approximately 120 mm , corresponding to a plate Reynolds number of 2,690,000. As was the case for the Mach 1.91 boundary layer, all three measures of the boundary layer development were in close agreement with the experimental measurements for the Mach 1.36 case, as shown in table 5.2.

A modified grid was constructed using 141 axial and 94 vertical points for this Mach 1.36 case, corresponding to a physical domain of 120 mm by 23.75 mm . Calculations with this modified grid provided a solution identical to that obtained with the original 141×141 grid.

The last step before constructing the entire RANS-LES computational grid was to use grid points from the modified wall-function grids just discussed, extending from 81-141 in the axial domain and fix the solutions at the 81st axial station as the

inflow, in order to reduce the grid requirements of the final hybrid RANS-LES grid. Boundary layer calculations subsequently obtained with these two shortened axial grids using 61 axial points and 94 vertical points again returned the same boundary layer quantities and velocity profiles as the other solutions. These were the RANS grids that were used to join with the LES mixing region computational domain.

As will be discussed in section 5.3, three different axial grid spacings were examined in the initial two dimensional hybrid calculations. In all cases, however, the vertical spacing from the two RANS regions was continued throughout the entire LES region. With the tightest vertical spacing of the wall-function boundary layer solutions set to 0.05 mm , 10 grid spacings were used vertically across the splitter base. As a result, all of the hybrid grids used 197 vertical points in the mixing region.

For all of the hybrid calculations discussed in this chapter and in chapter 6, fixed inflow boundary conditions were used at the RANS inflows. The fixed inflow for the Mach 1.91 upper stream was placed at an axial position 67 mm upstream of the splitter plate trailing edge and the Mach 1.36 lower stream inflow was placed 42 mm upstream of splitter tip. Although information regarding the temperature and heat transfer characteristics of the splitter plate walls were not available from the experiment, these surfaces were set as adiabatic no-slip boundaries. At the outflow of the mixing section, corresponding to an axial distance of 300 mm from the trailing edge of the splitter plate, an extrapolation boundary condition was used, which is appropriate for the mixing supersonic flow exiting the axial domain. The top and bottom walls of the mixing section were approximated as slip walls, and no

attempts were made to simulate boundary layers developing on these two surfaces.

The Goebel-Dutton experimental configuration was specifically designed with adjustable divergence angles for these walls to account for boundary layer growth, and to thereby provide experimental data that may be directly compared to calculations which do not include the mixing section boundary layers.

The combined RANS-LES calculations were obtained by marching in time with the Gottlieb-Turkel scheme for the entire computational domain. Although the RANS regions did not change after reaching convergence, calculations were still performed in the RANS regions, in case any large perturbations from the LES region travelled upstream. Because of the zero-pressure gradient nature of these boundary layers, however, no large upstream fluctuations were noted in any of the hybrid calculations. No subgrid scale model was used in any of the two dimensional calculations discussed in this chapter. As a result, the use of a turbulence model terminated at the end of the RANS regions. For the three dimensional calculations of the same configuration discussed in chapter 6, the Smagorinsky subgrid scale model was employed.

For the two-dimensional cases discussed in this chapter and the three-dimensional cases discussed in chapter 6, a series of flowfield contours is shown in the mixing section to illustrate the mixing layer development and to help compare qualitative features of the different modeling approaches. Instantaneous density and entropy contours are presented to show images of the mixing layer at a snapshot in time. For each of these quantities, an image is shown for the first one-third of the mixing duct to provide details of the initial mixing layer development. An image of the

entire computational domain is also shown, extending from the inflow of the two isolated RANS streams to the exit of the mixing section in the LES region.

Density contours are useful for visualizing the flow characteristics in the mixing region. In addition, they provide a computational analogy to the Schlieren photographs that are used to illustrate mixing layer development in experiments. While the strongest gradients of the density will be observed to be in the developing shear layer, gradients are also observed in the regions above and below the mixing layer. These are the result of Mach waves generated by the unsteady mixing layer and their interaction with the two walls of the confined mixing section. Such waves were also evident in the Schlieren photographs of the Goebel-Dutton experiments. A Schlieren image taken of the first 250 *mm* of the mixing section in the Goebel-Dutton case 2 experiments is shown in figure 5.2.

In order to isolate the development of the mixing layer, instantaneous entropy contours are also used in the following discussions. Because the Mach waves occurring between the developing mixing layer and the two mixing section walls are of relatively weak strength, the entropy gradients in these regions are quite small. As a results, entropy contours enable emphasis to be placed on the mixing layer development more clearly than is possible with the density contours. The entropy function of the PLOT3D program [109] is used here, which calculates the entropy in an ideal gas with constant specific heats as:

$$S - S_{ref} = C_v \ln \left(\frac{P}{P_{ref}} \right) + C_P \ln \left(\frac{\rho_{ref}}{\rho} \right) \quad (5.1)$$

Where P_{ref} and ρ_{ref} are reference quantities used to nondimensionalize the entire flow domain.

Time-averaged axial velocity and turbulent intensity profiles obtained from the calculations are compared with experimental measurements. The procedure used to obtain these time averaged quantities is discussed in appendix C.

5.3 Axial Grid Density Effects

Three computational grids are considered initially to examine the effects of axial grid resolution. Because the grid resolution in the vertical direction exceeded that of the axial spacing for even the finest grid examined here, no variation in the vertical spacing was considered and all of the grids had 197 vertical points in the mixing section. The three grids examined have 200, 400, and 800 axial points respectively and all are similar to the domain shown in figure 5.3, which corresponds to the coarsest grid used (200 axial points). The grid detail extending from the end of the RANS regions into the initial portion of the LES region is shown in figure 5.3(a). The entire computational domain is shown in figure 5.3(b). For clarity, only every third grid point is shown in both the axial and vertical directions in figure 5.3(b). Showing every grid point for even the coarsest 200 point grid would obscure the depiction of the grid topology.

Figure 5.4 shows the detail near the trailing edge of the splitter for all three grids. In every case, 10 equal grid spacings are used vertically across the 0.5 mm splitter plate trailing edge. This grid spacing ($\Delta y = 0.05$ mm) matches the initial vertical spacing of the wall boundary layers in the RANS regions. Axially, all three grids are

mixing region size	200 axial pts.	400 axial pts.	800 axial pts.
stretching factor $\frac{\Delta x_{i+1}}{\Delta x_i}$	1.0215	1.0083	1.0029
$\Delta x_1 (mm)$.10	.10	.10
$\Delta x_{last} (mm)$	6.52	2.60	1.06
$\frac{\Delta x_{last}}{\Delta x_1}$	65.2	26.0	10.6

Table 5.3: Comparison of axial grid spacings

packed to the splitter trailing edge such that the initial Δx spacing is twice that of the finest Δy spacing. The only difference between the three grids is the axial stretching factor, which is fastest for the 200 point grid and slowest for the 800 point grid. In all cases a geometric stretching factor was used. Table 5.3 provides a comparison of the axial spacings for the three grids.

The first two dimensional simulation investigating grid density effects was for the coarsest grid using 200 axial points. Figures 5.5 and 5.6 provide instantaneous contours of the density and entropy for this case. In each of these contours, a vortex shedding pattern originates from the trailing edge of the splitter plate due to the separation of the two flows leaving the wall bounded RANS regions and entering the LES mixing section. The vortex shedding quickly dissipates and the flow appears to be laminar until an axial position corresponding to nearly one fourth of the overall duct length. At this position, an instability forms and the flow initiates transition to an unsteady turbulent pattern. The Reynolds number at the instability location is 900,000 using an average value of the viscosity and density from the two streams,

the difference in velocity of the two streams, and the axial position of approximately 80mm.

The turbulent-like behavior quickly dissipates again, however, and the flow returns to a laminar state. For this case, the comparatively coarse grid enables the truncation error of the Gottlieb-Turkel scheme, shown previously in equation (3.24), to damp any oscillations without the use of any turbulence model or artificial dissipation in the mixing region. Because the turbulent behavior for this case was very limited, no turbulent averaging was done for this case. One final observation from this case was the Mach waves originating from the trailing edge of the splitter. These waves, in turn, reflect off of the mixing section walls and back onto the splitter. A qualitatively similar pattern was observed in the Goebel-Dutton Schlieren photographs as shown in figure 5.2.

The second two dimensional simulation was for the computational grid using 400 axial points. The characteristics of this flow were substantially different from those of the 200 grid point case. Instantaneous density and entropy contours are provided in figures 5.7 and 5.8. A stronger vortex shedding is evident for this case, although the vortex strength gradually dissipates back to a laminar state approximately 40 mm downstream of the splitter trailing edge. An instability again forms at an axial position of 80 mm which in turn slightly dissipates before resuming growth at a position 180 mm downstream of the splitter plate trailing edge. A turbulent pattern then grows from this location to the exit at $x = 300$ mm.

The 400 point axial grid examined consisted of smaller axial grid steps than the 200 axial point grid and had a significantly reduced stretching factor relative to the coarse grid. As a result, the truncation error term in the Gottlieb-Turkel scheme that effectively smooths discontinuities is substantially reduced for the 400 axial point grid, and the capability to resolve unsteady flow behavior is improved.

The third computational grid investigated in this section was for the 800 axial point grid. A substantially different flow behavior is also observed for this case compared to the solutions obtained with 200 and 400 axial points. The density and entropy contours in figures 5.9 and 5.10 again indicate a vortex shedding pattern that originates from the trailing edge of the splitter plate, but unlike the other two cases, the solution does not return to a laminar state before transitioning over to a turbulent-like pattern. The very tight axial spacing for this case is sufficient to minimize the truncation error damping effects on the unsteady flow development. Interestingly, the transition from the organized vortex structure to a more random turbulent structure occurs at nearly the same location as the transition for the other two computational grids, although the flow behavior both upstream and downstream of this point is substantially different.

A somewhat organized coherent structure may be observed from the contours of density and entropy for the 800 axial point case shown in figures 5.9 and 5.10, and near the end of the mixing section for the 400 axial point case shown in figures 5.7 and 5.8. These structures are similar in form to those of the well known Brown and Roshko [16,86] mixing layer studies. The Brown and Roshko investigations of incompressible turbulent mixing layers indicated that the turbulent mixing layer

development was characterized by large coherent structures. As the Reynolds number in their experiments was increased, a fine scale turbulence contained within the larger scale structures was evident. However, the mean flow properties were found to be the same regardless of the Reynolds number, indicating that the mean flow characteristics are dominated by the large scale structure.

The convective Mach number parameter was developed by Bogdanoff [12] and Papamoschou and Roshko [76] for use in characterizing the compressibility characteristics of high speed turbulent mixing layers. For a planar mixing layer with equal specific heat ratios, the convective Mach number is defined:

$$M_c = \frac{U_1 - U_2}{a_1 + a_2} \quad (5.2)$$

For the Goebel-Dutton case 2 experiment investigated here, the convective Mach number was 0.455. Clemens and Mungal [21] conducted experiments of planar turbulent mixing layers with convective Mach number from 0.28 to 0.79. They found that as the convective Mach number is increased, the characteristics of the mixing layer changed from an organized two-dimensional Brown-Roshko structure to a three-dimensional structure with less evidence of large scale organization.

Direct simulations of compressible shear layers conducted by Sandham and Reynolds [87] also indicated that three-dimensional instability modes become dominant at convective Mach numbers greater than 0.6. Their simulations also indicated reduced mixing layer growth rate with increasing convective Mach number.

The mean axial velocity profiles obtained from the two-dimensional solutions using 400 and 800 axial grid points are compared to the measurements of Goebel and Dutton in figure 5.11. Because the calculations discussed in this chapter are only two-dimensional, and do not use a true LES approach in the mixing region, only qualitative comparisons with the data will be emphasized here. The comparisons are made at four axial stations in the mixing layer, $x = 50, 100, 150$, and 200 mm , with $x = 0$ representing the beginning of the mixing section. As mentioned previously, $x = 0$ is also the axial position at which the switch from the RANS regions to the the LES region occurs. Comparisons of the two turbulence intensities u_{rms} and v_{rms} are shown in figures 5.12 and 5.13 respectively.

The mean axial velocities are plotted versus vertical position normalized by the mixing section height, 48 mm , in order to give an indication of the shear layer spreading through the mixing section. In addition, the vertical positions were adjusted so that $y/H = 0$ represented the location where the local axial velocity was the mean of the two freestream velocities. The adjustment was also made in the experimental data as reported by Goebel and Dutton [36]. The turbulence intensities are plotted versus vertical position normalized by the local shear layer width, defined by Goebel and Dutton as the distance between vertical positions where $U = U_1 - 0.1\Delta U$ and $U = U_2 + 0.1\Delta U$. The two velocities U_1 and U_2 are the upper and lower stream velocities, respectively.

The computed axial velocity contours indicate a much larger wake region than found in the experiments, and a greater discrepancy is observed for the 400 axial point case. At the $x = 200\text{ mm}$ axial station, both solutions have returned to agree

moderately well with the data. The comparisons of streamwise and transverse turbulence intensities in figures 5.12 and 5.13 indicate substantial differences between the solutions and data. Both solutions, and especially the 400 axial point solution, show low levels of u_{rms} and v_{rms} at the $x = 50$ mm station. For the 400 point case, this corresponds to the nearly laminar like state indicated by the contours shown in figures 5.7 and 5.8. Further downstream the intensities of the two solutions grow substantially and by the $x = 200$ mm station, the transverse turbulence intensities from the solutions is substantially larger than those from the experiment. The profiles of u_{rms} obtained from the calculations demonstrates a double peak, particularly at $x = 100$ mm. This appears to be an indication that the velocity fluctuations are influenced more by the organized vortical structure early in the mixing section than by the formation of turbulence.

Despite the significant differences among the solutions obtained with the three computational grids discussed here, the vortex shedding from the trailing edge of the splitter and the appearance of waves originating from the splitter plate and reflecting off the mixing section walls were common to the three solutions. In the next section, the influence of the splitter base region and the mixing section walls are investigated. A final note from this section is that while grid refinement in RANS calculations is performed to achieve grid independence, and major changes in flow solutions when using two different grid resolutions usually indicates a modeling problem, this is not the case in LES computations. Grid refinement in LES enables more and more of the unsteady turbulent spectrum to be resolved, until the limit of DNS is reached. The purpose of a subgrid scale model in LES computations is to

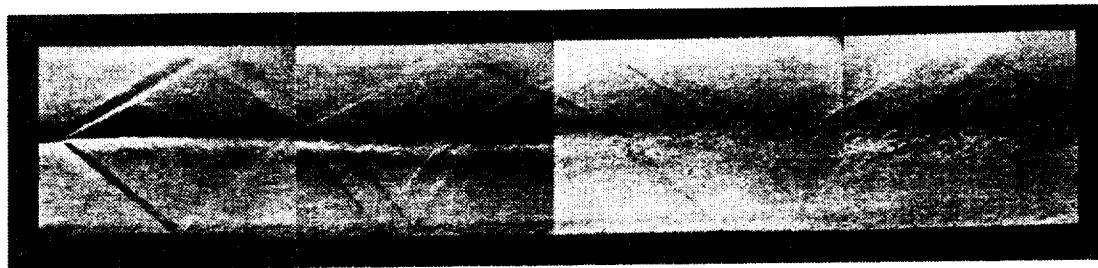
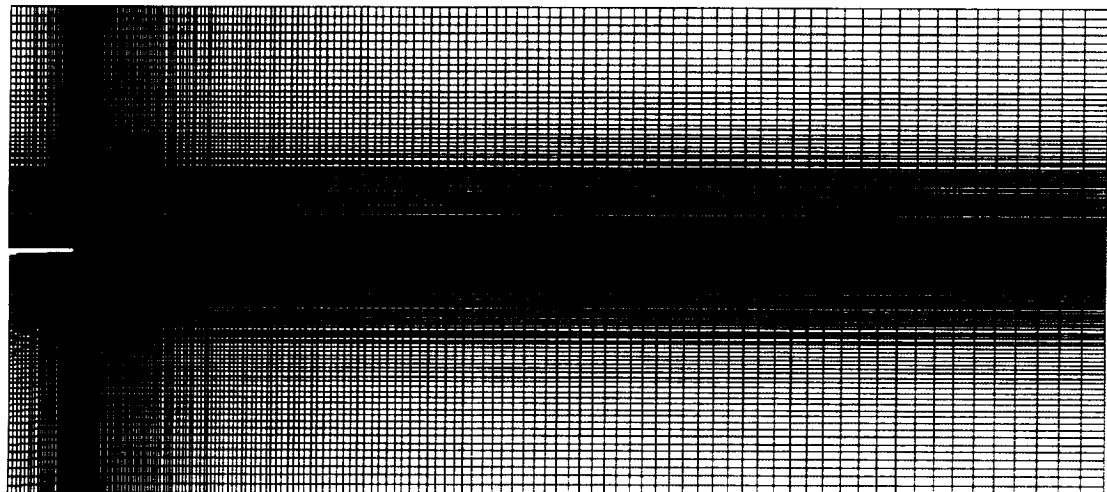


Figure 5.2: Schlieren photograph of the Goebel-Dutton mixing layer (from Ref. 34, used with permission)

effectively represent the turbulent motion that is too small to be resolved by the computational grid.

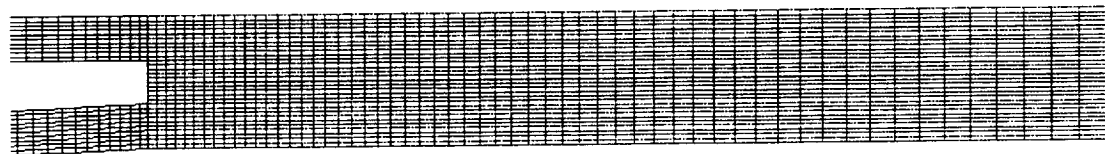


(a) Beginning of mixing section

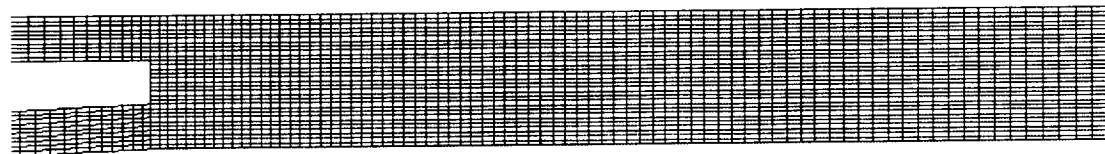


(b) Entire computational domain (every third grid point in each direction shown)

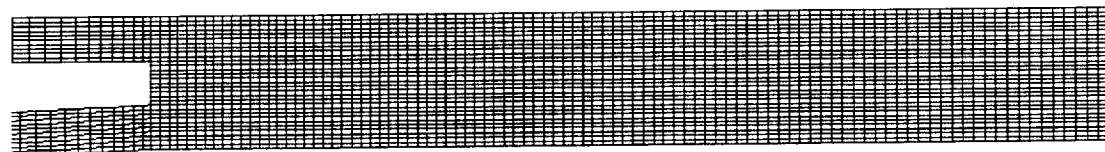
Figure 5.3: Computational grid for the 200 axial grid point case



(a) 200 axial points in mixing section

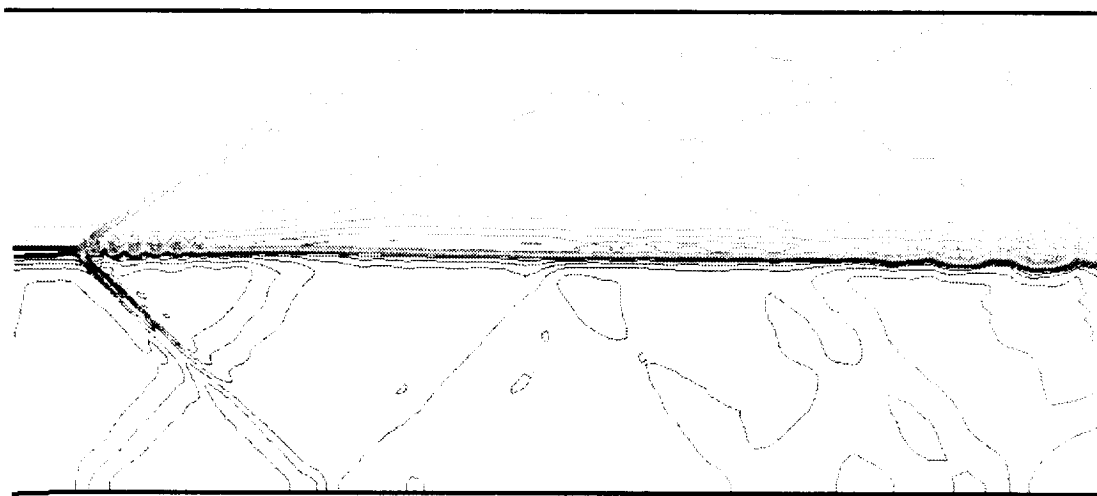


(b) 400 axial points in mixing section



(c) 800 axial points in mixing section

Figure 5.4: Comparison of computational grids near the splitter plate trailing edge

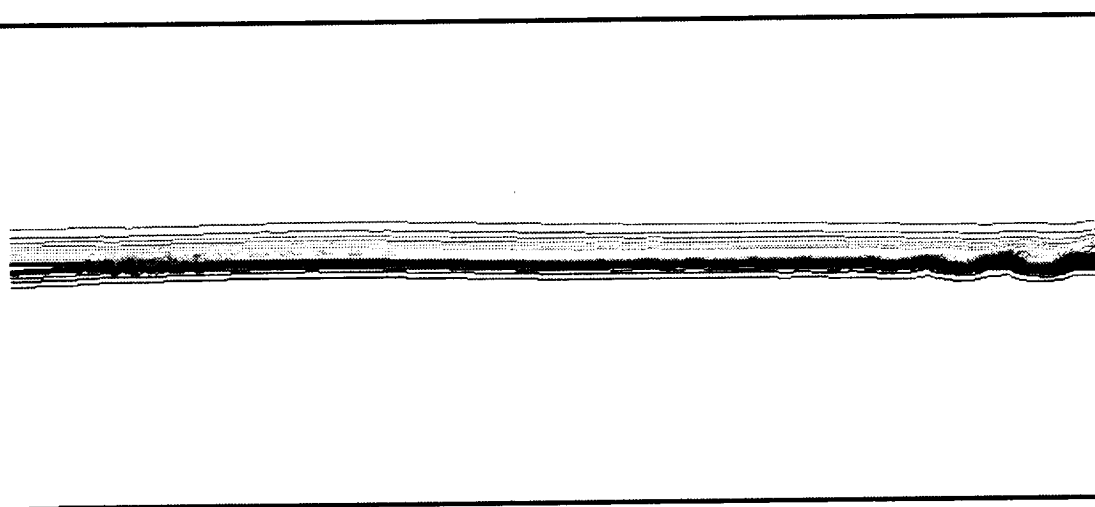


(a) Beginning of mixing section

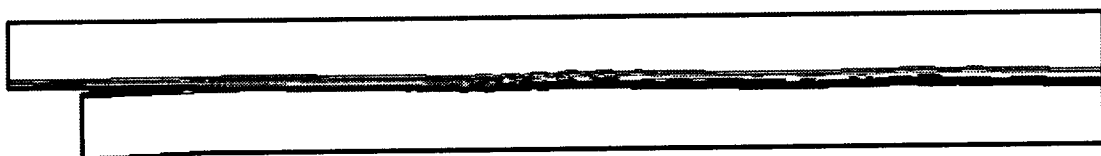


(b) Entire mixing section

Figure 5.5: Instantaneous density contours for the 200 axial grid point case

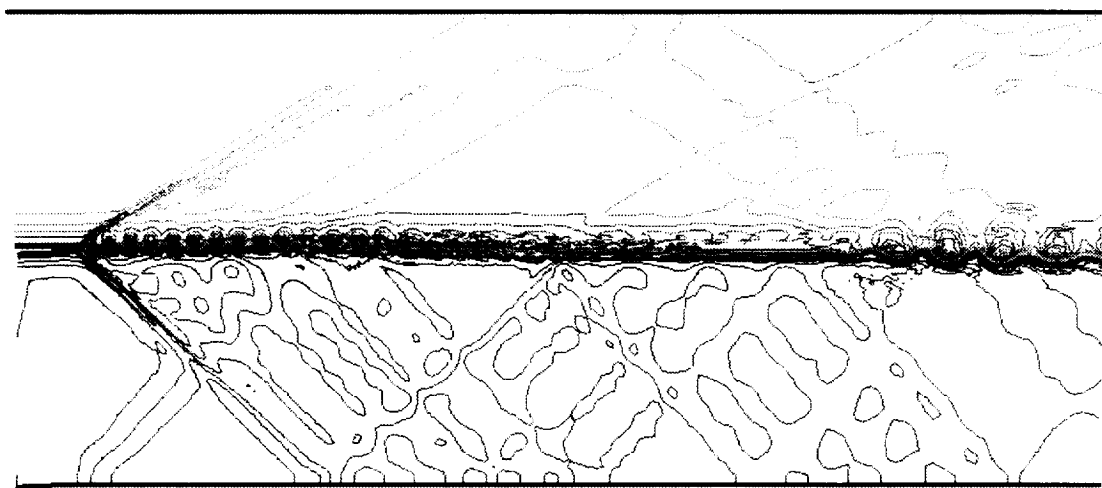


(a) Beginning of mixing section



(b) Entire mixing section

Figure 5.6: Instantaneous entropy contours for the 200 axial grid point case

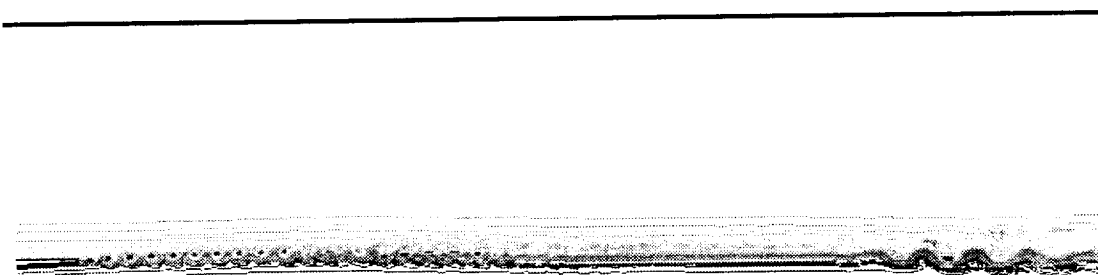


(a) Beginning of mixing section

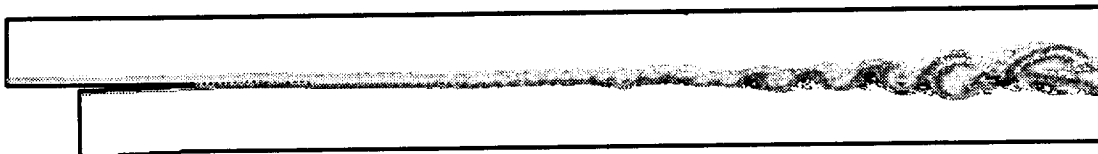


(b) Entire mixing section

Figure 5.7: Instantaneous density contours for the 400 axial grid point case

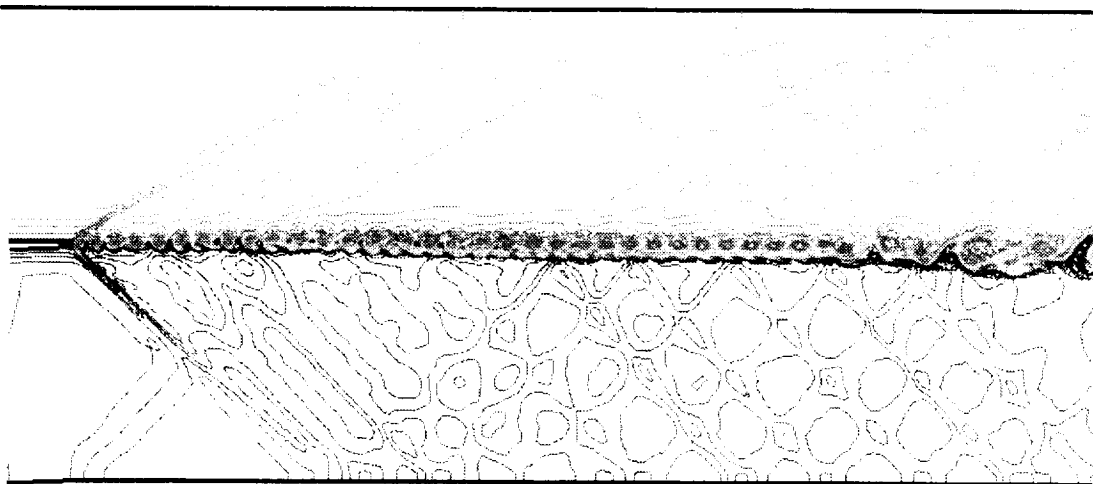


(a) Beginning of mixing section

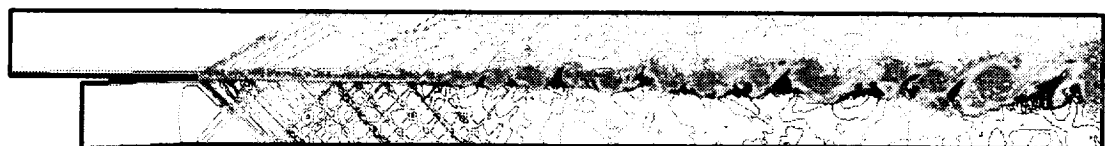


(b) Entire mixing section

Figure 5.8: Instantaneous entropy contours for the 400 axial grid point case

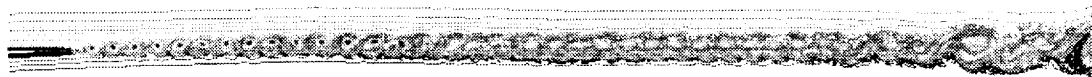


(a) Beginning of mixing section



(b) Entire mixing section

Figure 5.9: Instantaneous density contours for the baseline 800 axial grid point case

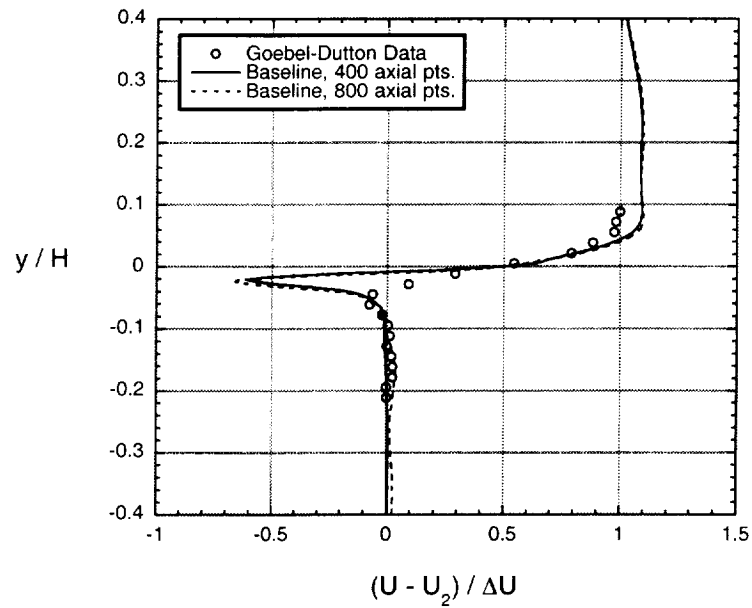


(a) Beginning of mixing section

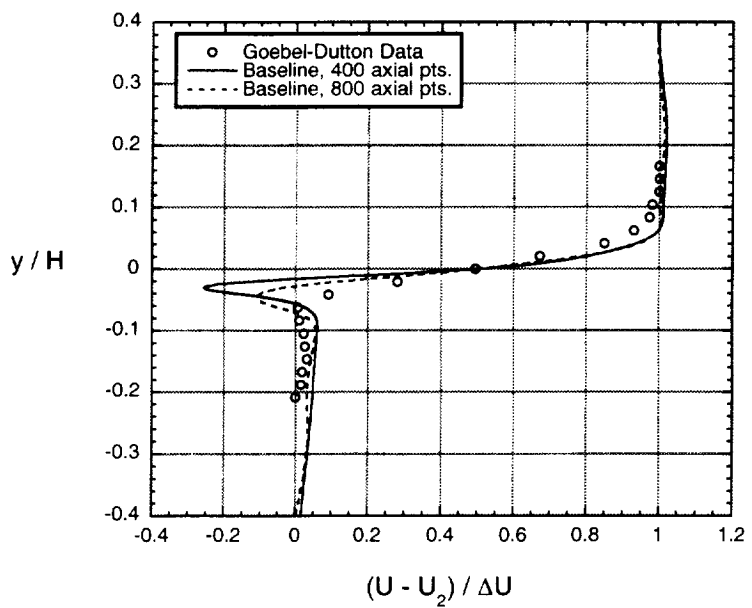


(b) Entire mixing section

Figure 5.10: Instantaneous entropy contours for the baseline 800 axial grid point case

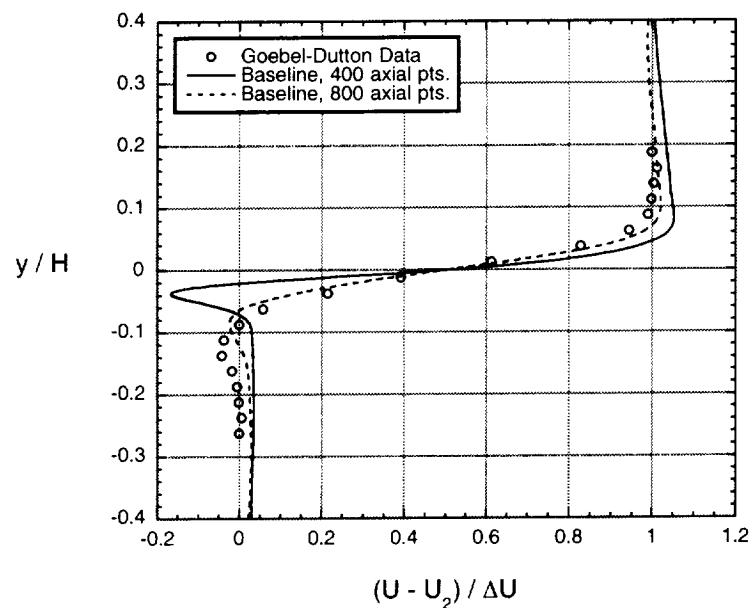


(a) $X = 50 \text{ mm}$

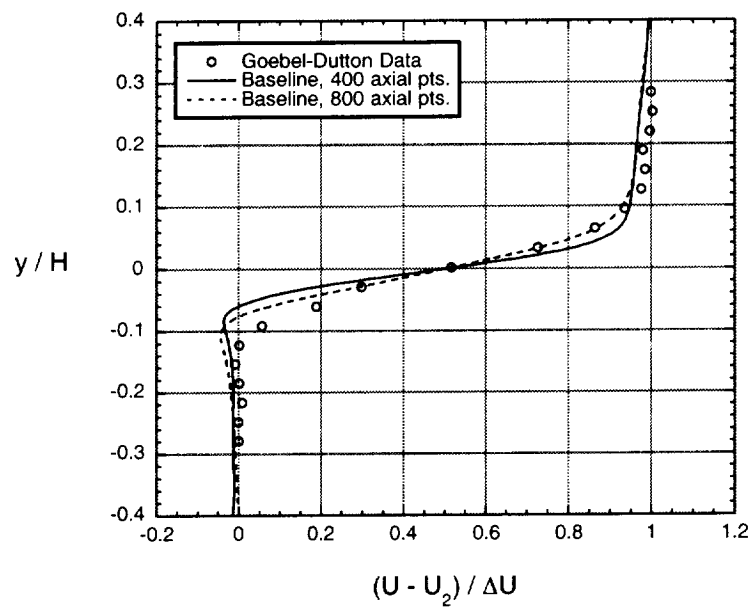


(b) $X = 100 \text{ mm}$

Figure 5.11: Time-averaged axial velocity profiles for 2D hybrid calculations investigating axial grid density effects

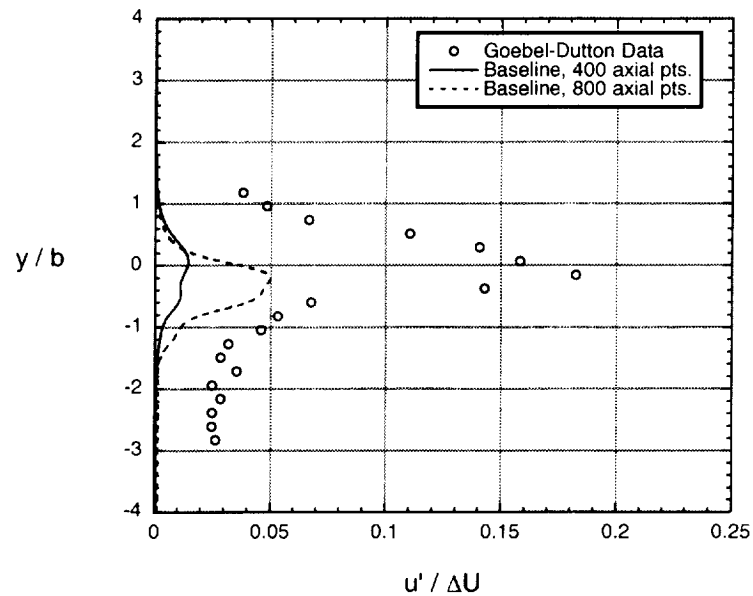


(c) $X = 150 \text{ mm}$

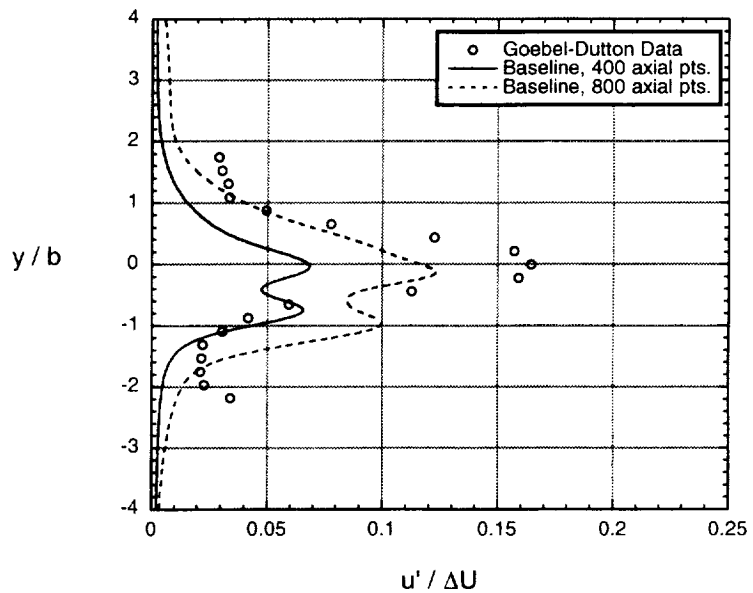


(d) $X = 200 \text{ mm}$

Figure 5.11: Concluded.

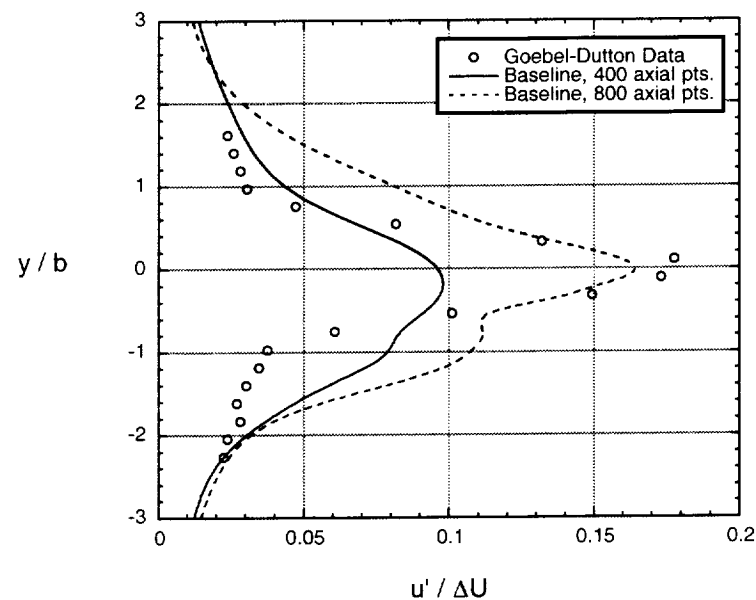


(a) $X = 50 \text{ mm}$

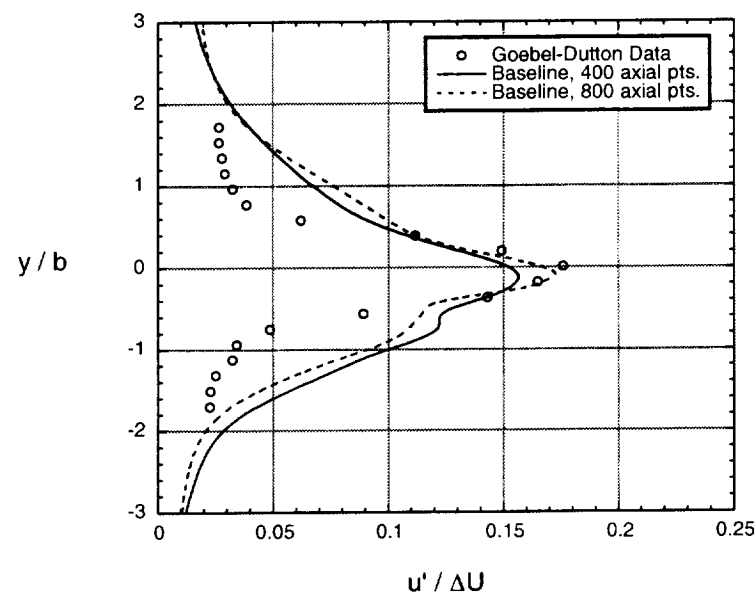


(b) $X = 100 \text{ mm}$

Figure 5.12: Profiles of u_{rms} for 2D hybrid calculations investigating axial grid density effects

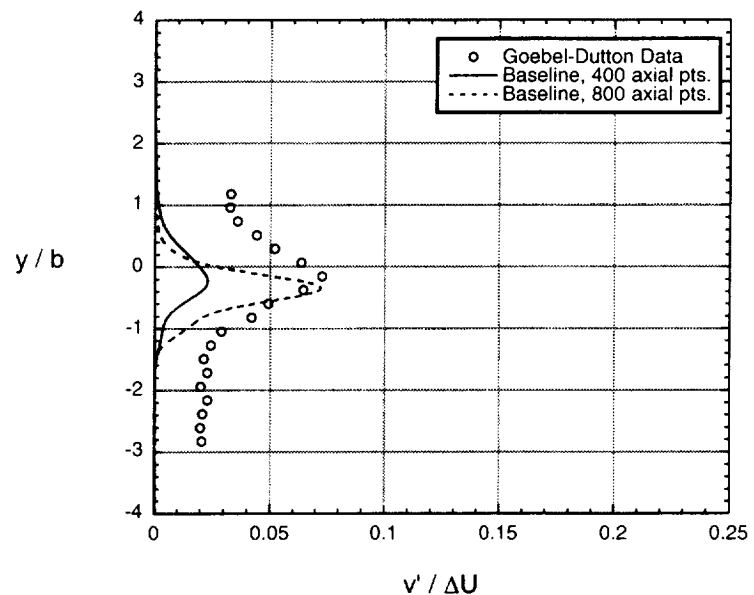


(c) $X = 150 \text{ mm}$

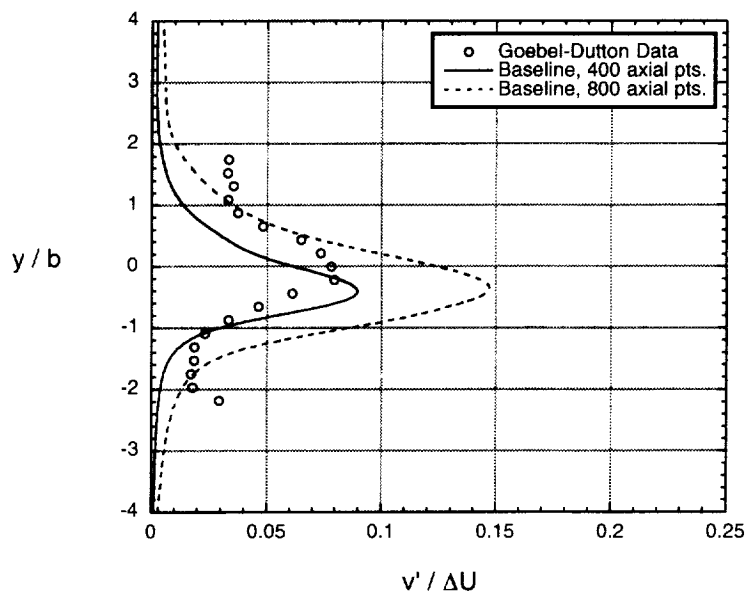


(d) $X = 200 \text{ mm}$

Figure 5.12: Concluded.

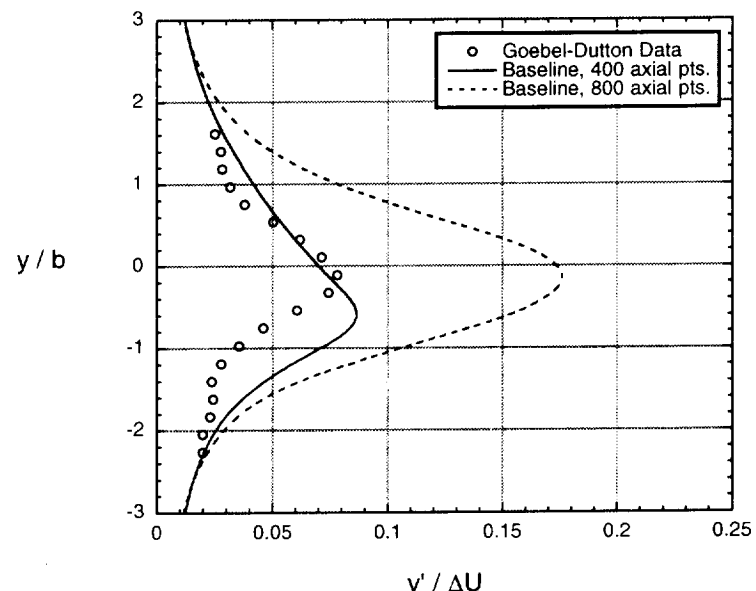


(a) $X = 50 \text{ mm}$

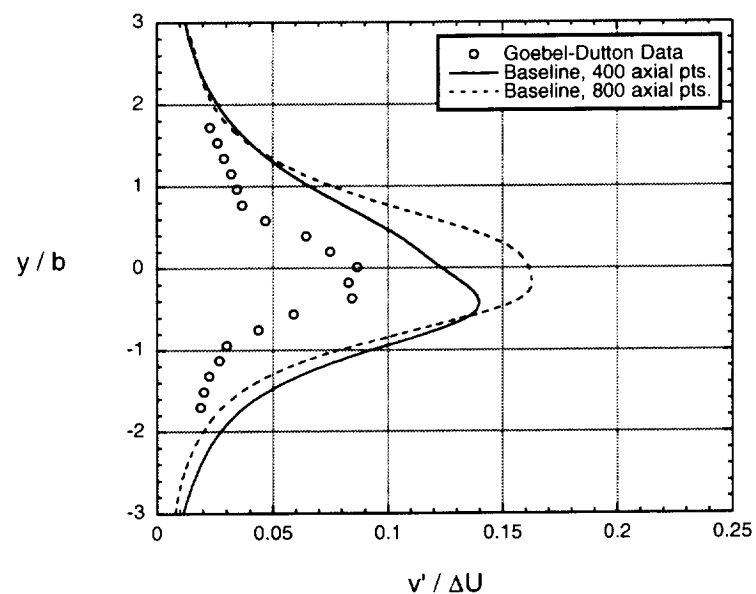


(b) $X = 100 \text{ mm}$

Figure 5.13: Profiles of v_{rms} for 2D hybrid calculations investigating axial grid density effects



(c) $X = 150 \text{ mm}$



(d) $X = 200 \text{ mm}$

Figure 5.13: Concluded.

5.4 Boundary Condition Effects

In this section, results obtained for the baseline case with 800 axial points are compared to two additional solutions obtained with 800 axial points. The first of these considers a modified splitter geometry in which the splitter trailing edge is reduced to a sharp tip, and as a result, the flow separation and vortex shedding is removed. The second additional case is obtained for a modified mixing section in which the mixing section walls are moved very far vertically from the mixing layer. This is done so that any waves originating from the trailing edge of the splitter plate or the mixing layer do not have the opportunity to reflect off the mixing section walls and back to the mixing layer.

The overall grid structure for the case with a sharp trailing edge is identical to that of the baseline 800 axial grid point case, except for the treatment of the splitter plate trailing edge. A comparison of the grid detail around this region for the baseline geometry and the current case with a sharp trailing edge for the splitter is shown in figure 5.14. In the baseline geometry, 10 grid spacings are used in the axial direction at the base of the splitter, equally spaced at 0.05 mm , to resolve the flow region just downstream of the 0.5 mm thick splitter trailing edge. The modified geometry shown in figure 5.14(b), removes all but one grid spacing, such that the confined flows from the RANS regions will meet directly at the beginning of the LES region. The grid stretching in the vertical dimension was performed in the same manner as that used for the baseline 800 point grid, and reduced the vertical domain from 197 points to 188. The placement of the axial grid points was identical to that of the baseline grid.

In the Goebel-Dutton experiment and in all of the computations discussed in the previous section, the height of the mixing section was 48 mm. The density contours shown in the previous section for the cases with 400 and 800 axial grid points, as well as Schlieren photographs taken in the experiment, revealed a series of Mach waves that reflected off of the top and bottom walls of the mixing section and back onto the mixing layer. The strongest of these waves originated from the trailing edge of the splitter plate.

To determine if these wave reflections influenced the instability formation in the shear layer where the simulations appeared to become turbulent, at $x = 80\text{mm}$ for both the 400 and 800 grid point cases, a modified grid was generated which moved each wall far from the mixing layer such the effective mixing section height became 900 mm. This extreme spacing resulted in all waves generated from the splitter trailing edge or mixing layer to pass out of the outflow boundary at $x = 300\text{mm}$ without the opportunity to reflect back onto the mixing layer. This computational grid, which had 800 axial points positioned the same as for the baseline 800 point case, is shown in figure 5.15. For clarity, only every fourth point is shown in each direction. In addition, the 197 points forming the vertical domain in the baseline grid were also used in this modified grid. The extra points needed to extend the vertical dimension to a total of 900 mm were added on to each side of the mixing section, such that the total number of points in the vertical dimension for this modified grid was increased to 347.

Figures 5.16 and 5.17 provide instantaneous density and entropy contours for the case with a sharp trailing edge. As expected, the vortex shedding evident in the

baseline case was removed in the current case with the sharp tip. The lack of a separation region results in an initially laminar mixing layer through the beginning of the mixing section. Interestingly, the laminar flow begins to transition to a more turbulent structure at nearly the same position observed for the baseline case, at approximately $x = 80 \text{ mm}$. The structures remain relatively small until approximately $x = 150 \text{ mm}$ where large scale turbulence forms. These structures are more similar to the Brown-Roshko organized structures than were those of the baseline case with 800 axial points. Because the flows leaving the wall bounded regions experience a less rapid geometry change at the beginning of the mixing section for the sharp tip case, the strength of the initial waves off the splitter tip are reduced relative to the baseline case.

For the second modified case with mixing section walls moved away from any region of influence on the mixing layer, the same set of instantaneous contours are provided in figures 5.18 and 5.19. Two thin lines are drawn on each of the contour plots to indicate where the mixing section walls were placed in the baseline case, however, the density contours for entire mixing section shown in figure 5.16(b) indicate that the flow domain extended beyond these thin lines. With the very large vertical domain indicated by the computational grid shown in figure 5.15, only a portion of the vertical domain is displayed in the contour plots. Several waves beyond those originating from the splitter tip are found to originate from the unsteady vortex shedding, but they do not reflect back to the mixing layer.

As for the baseline 800 point case and the case with the sharp trailing edge, the transition location occurs at approximately $x = 80 \text{ mm}$ for this case, even without

the influence of Mach wave reflection onto the shear layer. The downstream turbulent eddy structure is qualitatively similar to that for the baseline case, although the height of some of the structures is greater than that for the baseline case. This is likely the result of the lack of mixing section walls to confine the mixing layer for the modified case. One noticeable difference between the contours shown in figures 5.18 and 5.19 for the modified mixing section and those of the baseline case in figures 5.9 and 5.10 is that the mixing layer grows at a slightly upward angle without the presence of the mixing section walls. For the comparison of mean axial velocities and turbulence intensities discussed next, an adjustment for the true mixing layer centerline will be employed, as was done in the previous section for the axial grid studies.

In figure 5.20, mean axial velocity profiles obtained from the two-dimensional solutions investigating the different boundary treatments obtained with 800 axial grid points are compared to the Goebel-Dutton measurements. In addition, comparisons of the turbulence intensities u_{rms} and v_{rms} are made in figures 5.21 and 5.22 respectively. As in the previous section, the primary objective here is to compare the different modeling approaches. Because these calculations were two dimensional only, and did not employ a subgrid scale model in the LES region, strict comparisons with the data are not emphasized.

The mean axial velocity profiles at $x = 50$ mm indicate that the solution obtained with a sharp trailing edge had the smallest wake, which was expected because this case did not have the large separation and vortex shedding of the other two cases. Further down in the mixing section, all of the solutions are in reasonable agreement

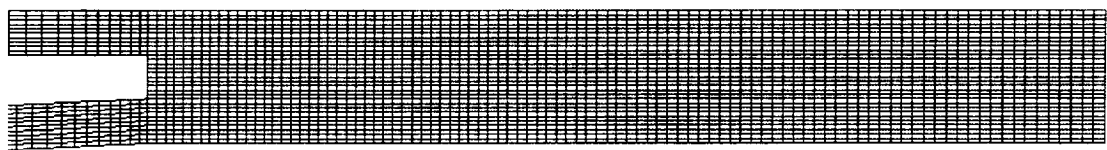
with the data. The baseline case and the solution obtained with mixing section walls removed are in particularly close agreement with each other by the end of the mixing duct.

All of the streamwise turbulence intensities are lower in peak magnitude than indicated by the Goebel-Dutton data at $x = 50 \text{ mm}$. Further downstream in the duct, the magnitudes increase to be more in line with the data, and the two solutions obtained with the standard height for the splitter base exhibit a double peak. As discussed in the section 5.3, this is believed to due to the influence of the upstream organized vortical behavior of the initial mixing layer. In figure 5.22, the solution obtained with a sharp trailing edge demonstrates significantly lower peak magnitudes in v_{rms} at $x = 50 \text{ mm}$ and $x = 100 \text{ mm}$. Further downstream in duct, all of the solutions indicate similar profiles of v_{rms} , and all have significantly larger peaks than the experimental data. Liou et al. [59] and Inoue [45] also reported large overpredictions in the streamwise and transverse turbulence intensities for two dimensional mixing layer computations and attributed the discrepancies to the lack of a third computational direction.

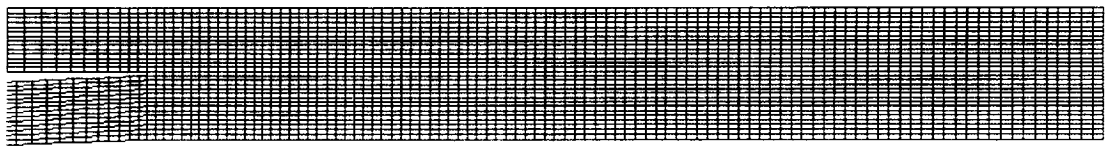
The results of this section indicate that the geometry of the splitter plate trailing edge has a significant effect on the initial shear layer formation. The unsteady vortex shedding is fundamental to the formulation of the hybrid RANS-LES method because although the mean flow properties of the incoming boundary layers are provided by the RANS regions, no turbulent oscillations are imposed that may initiate the instability of the mixing layer. Investigations of the splitter base region conducted by Clemens and Mungal [21] for an experimental configuration very

similar to that considered here also indicated an initial vortex structure that transitions into turbulence. This transition, however, occurred significantly closer to the splitter plate trailing edge in the experiments than indicated by these two dimensional calculations. The three dimensional calculations discussed in the next chapter investigate this transition position further.

Comparing the solution obtained with the standard placement of the mixing section walls to the solution obtained with the walls moved vertically to prevent any Mach wave reflection back onto the shear layer, some minor differences were noted. However, there was little effect on the transition location from the organized vortex structure to turbulence. Because the Mach wave behavior observed in the baseline calculations was very similar to that indicated by the Schlieren photographs taken from the experiment, the standard placement of the mixing section walls will be investigated for the three dimensional calculations discussed in chapter 6.



(a) baseline grid



(b) modified grid with sharp trailing edge for the splitter

Figure 5.14: Comparison of computational grids using 800 axial points, near the splitter plate trailing edge

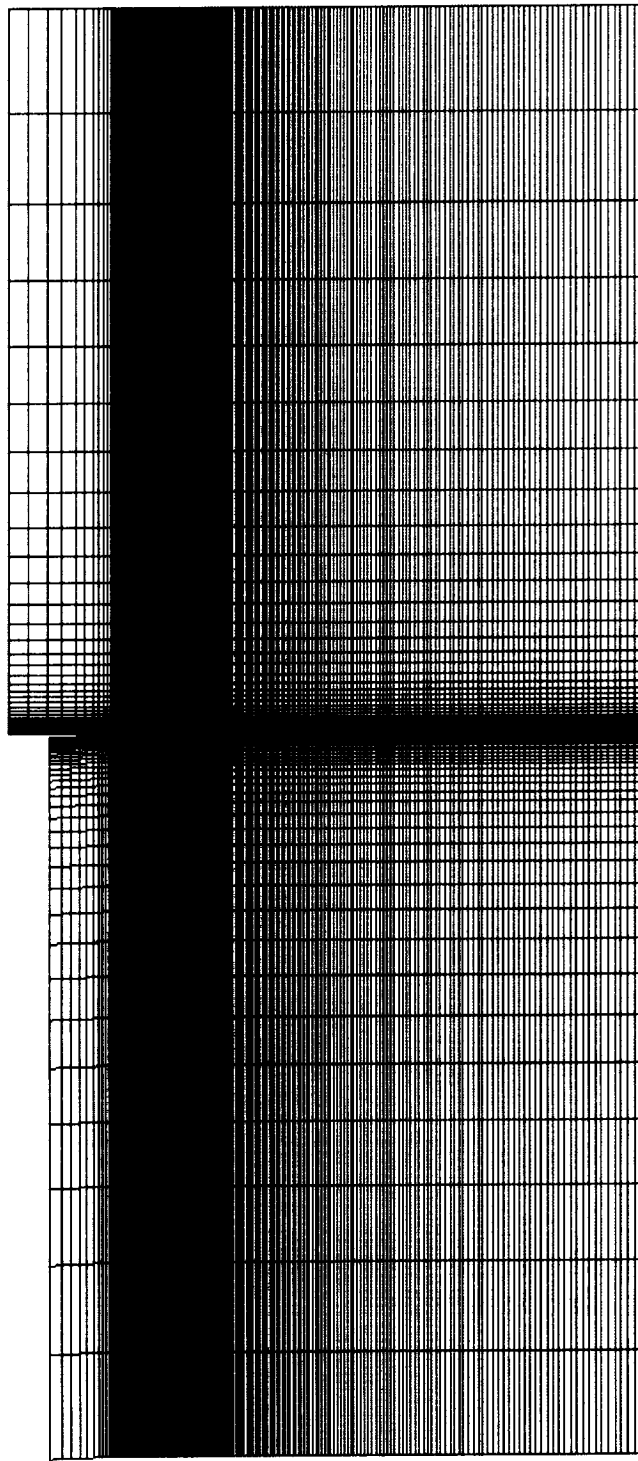
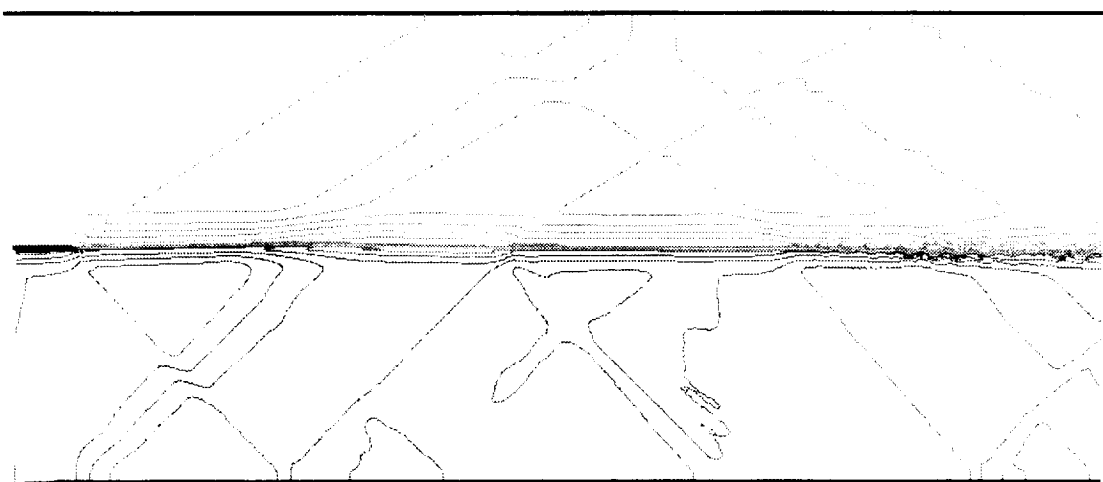
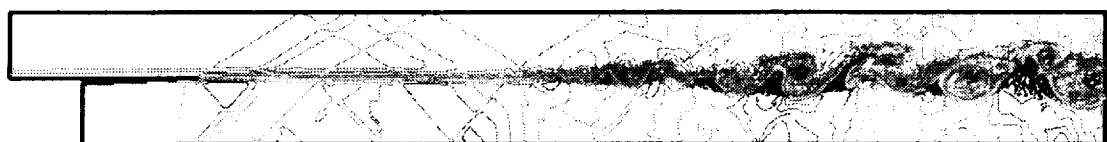


Figure 5.15: Computational grid for the 800 axial grid point case with the mixing section walls removed (every fourth point shown in each direction)

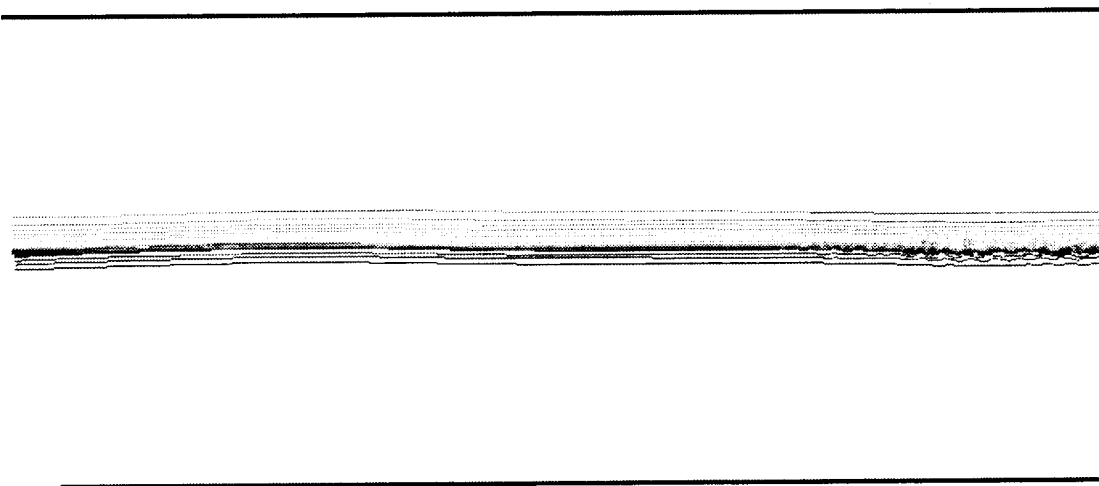


(a) Beginning of mixing section

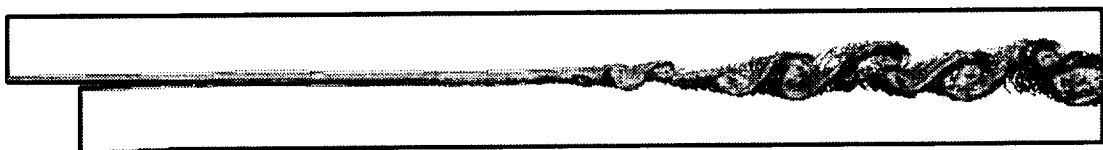


(b) Entire mixing section

Figure 5.16: Instantaneous density contours for the 800 axial grid point case with a sharp trailing edge for the splitter

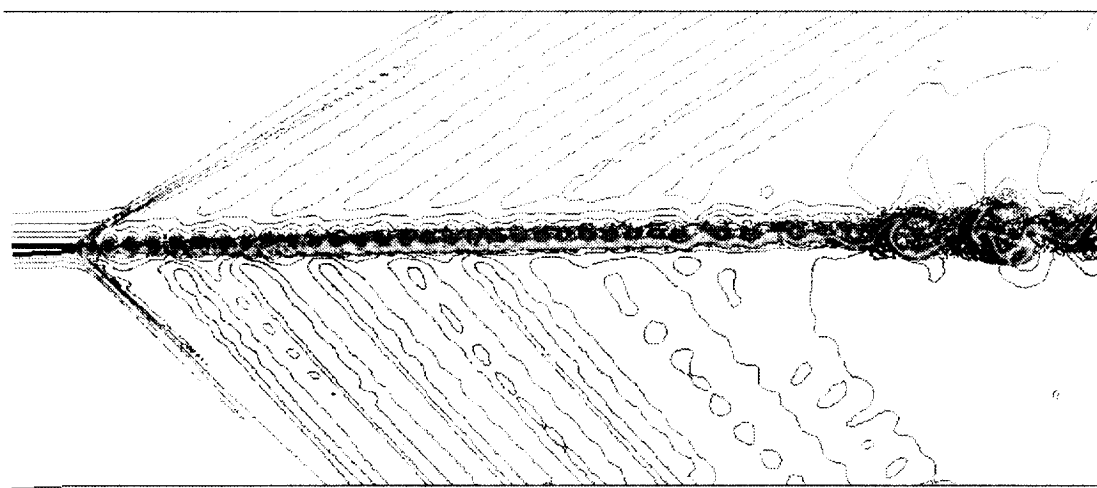


(a) Beginning of mixing section

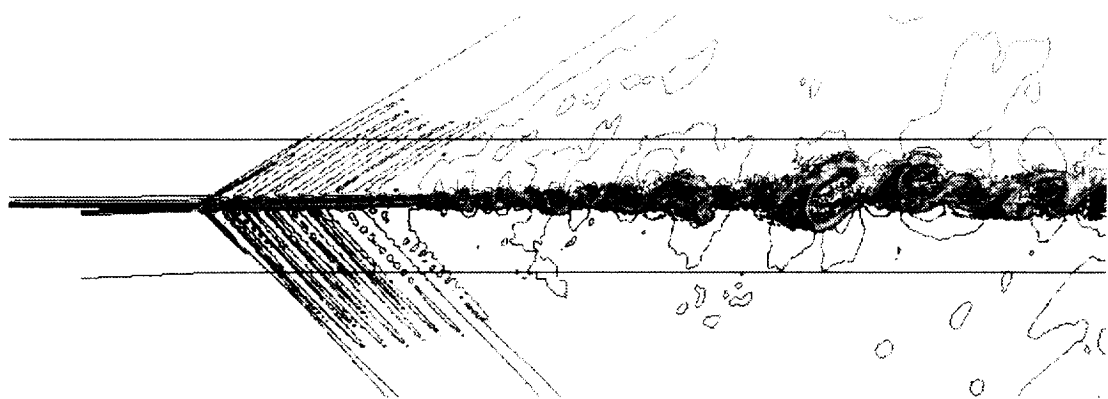


(b) Entire mixing section

Figure 5.17: Instantaneous entropy contours for the 800 axial grid point case with a sharp trailing edge for the splitter



(a) Beginning of mixing section

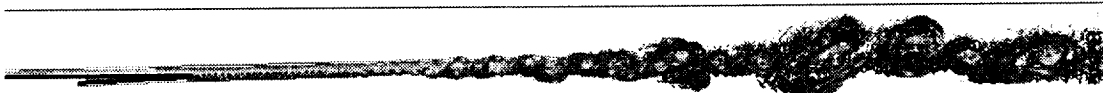


(b) Entire mixing section length only, entire vertical domain is not shown

Figure 5.18: Instantaneous density contours for the 800 axial grid point case with mixing section walls removed

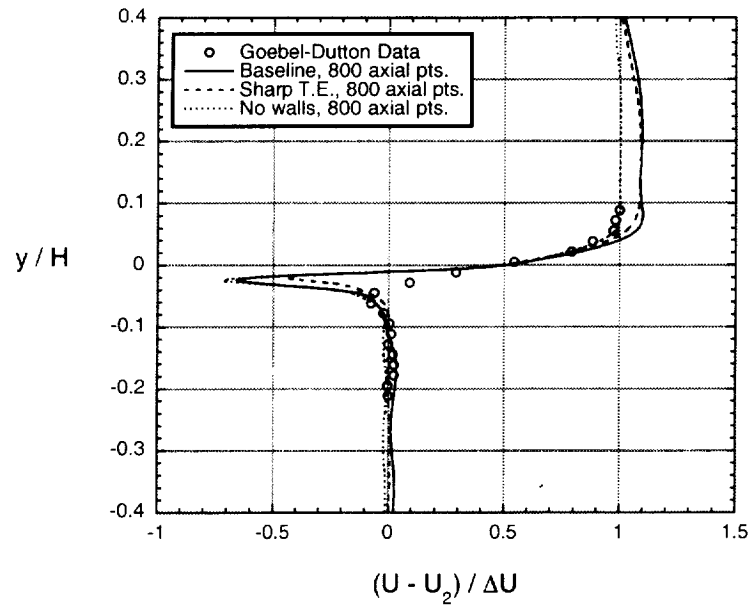


(a) Beginning of mixing section

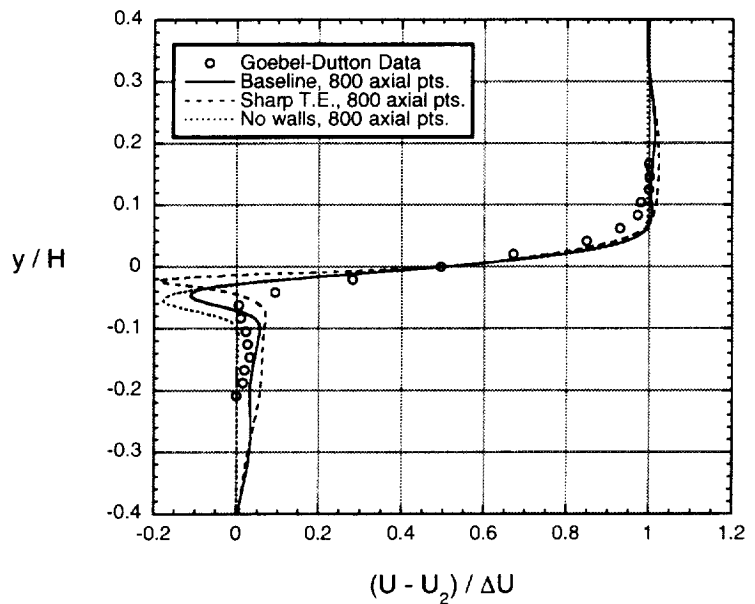


(b) Entire mixing section length only, entire vertical domain is not shown

Figure 5.19: Instantaneous entropy contours for the 800 axial grid point case with mixing section walls removed

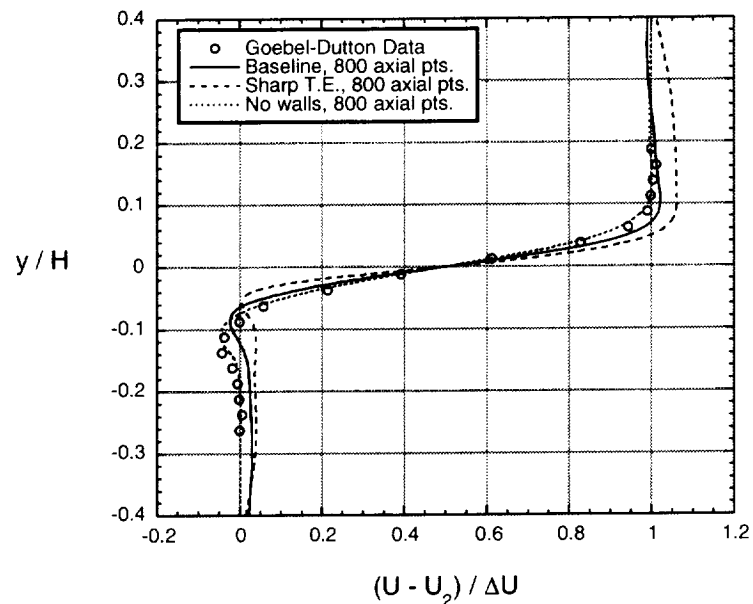


(a) $X = 50 \text{ mm}$

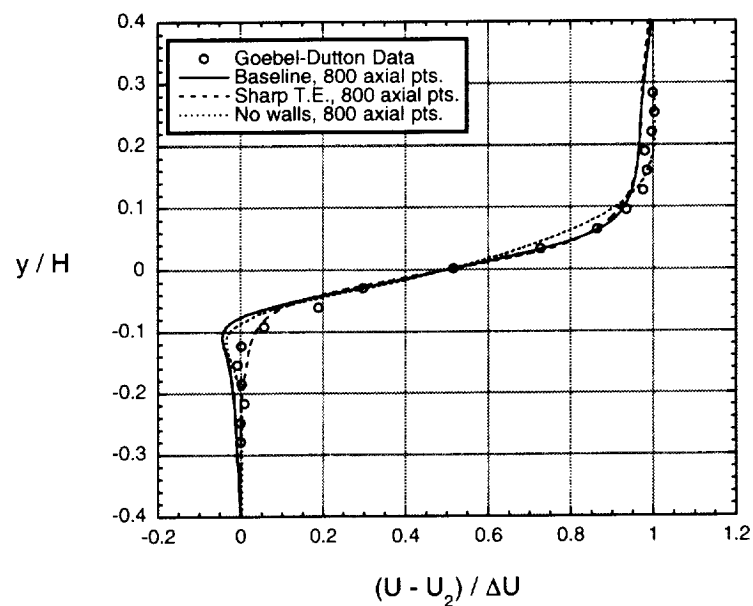


(b) $X = 100 \text{ mm}$

Figure 5.20: Time-averaged axial velocity profiles for 2D hybrid calculations investigating boundary condition effects

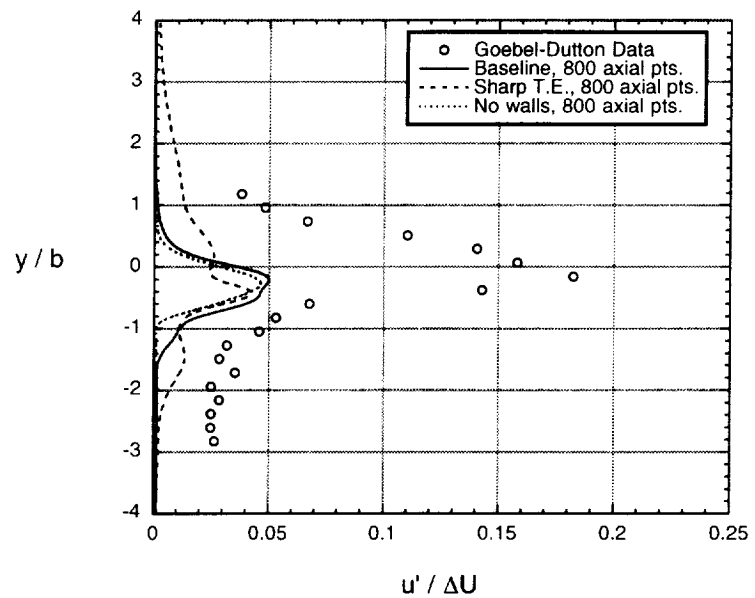


(c) $X = 150 \text{ mm}$

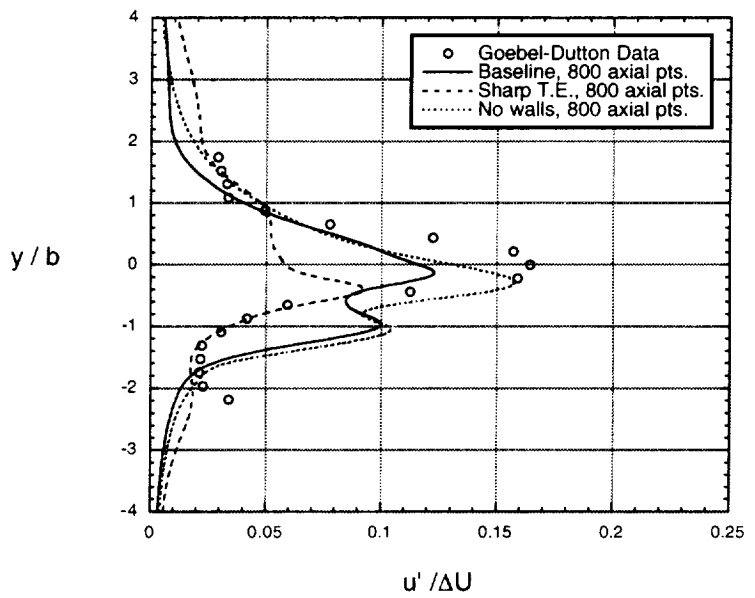


(d) $X = 200 \text{ mm}$

Figure 5.20: Concluded.

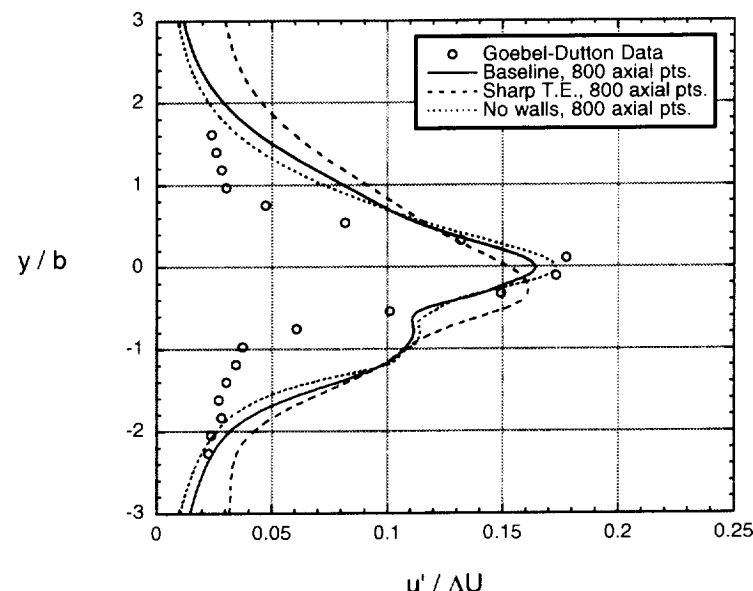


(a) $X = 50 \text{ mm}$

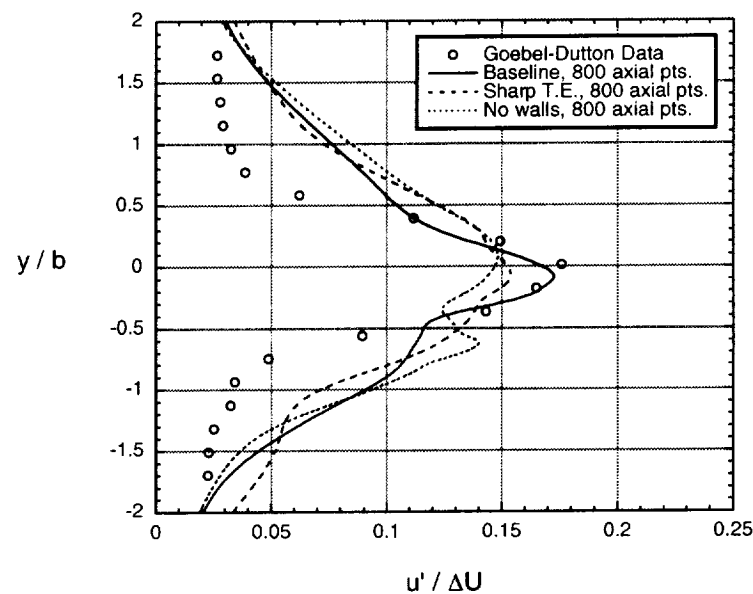


(b) $X = 100 \text{ mm}$

Figure 5.21: Profiles of u_{rms} for 2D hybrid calculations investigating boundary condition effects

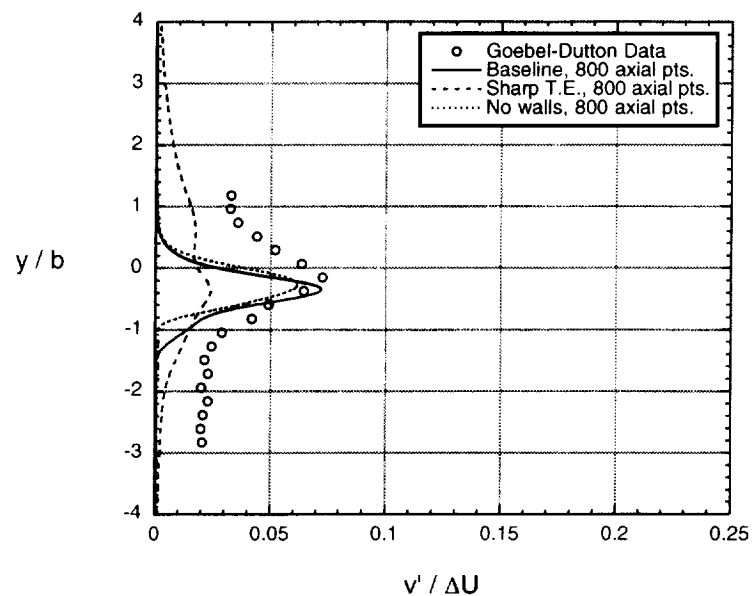


(c) $X = 150 \text{ mm}$

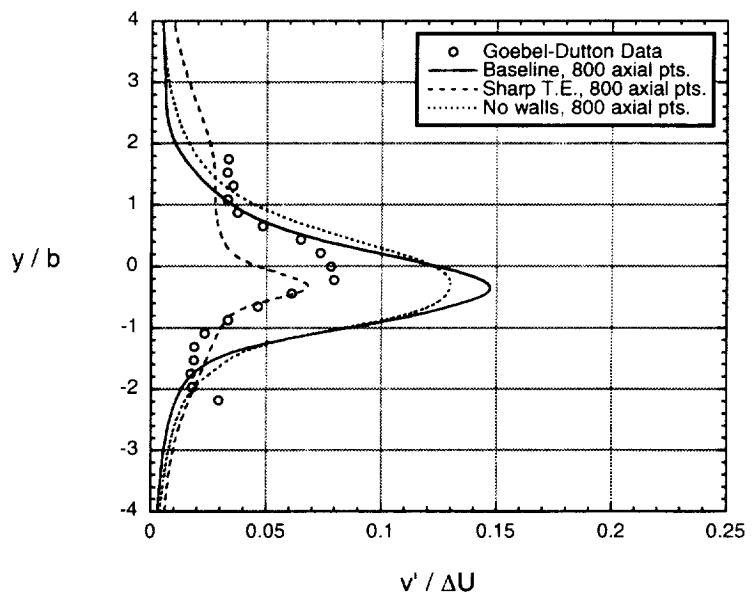


(d) $X = 200 \text{ mm}$

Figure 5.21: Concluded.

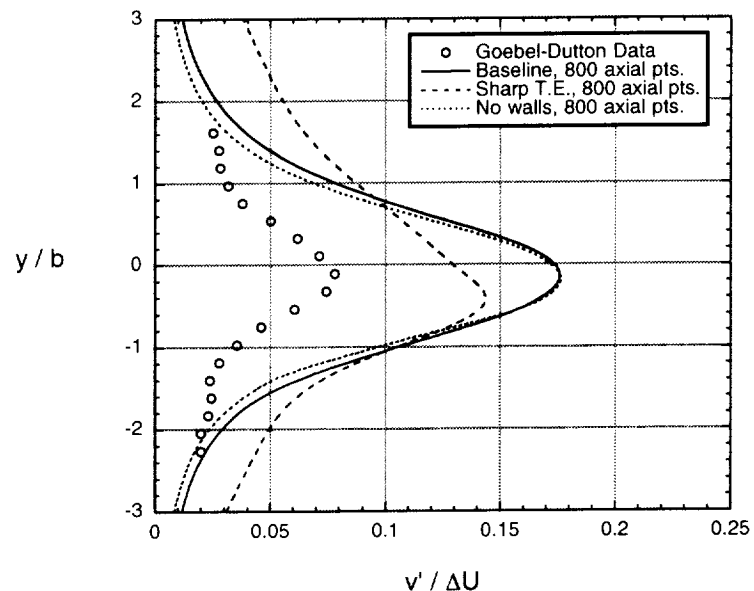


(a) $X = 50 \text{ mm}$

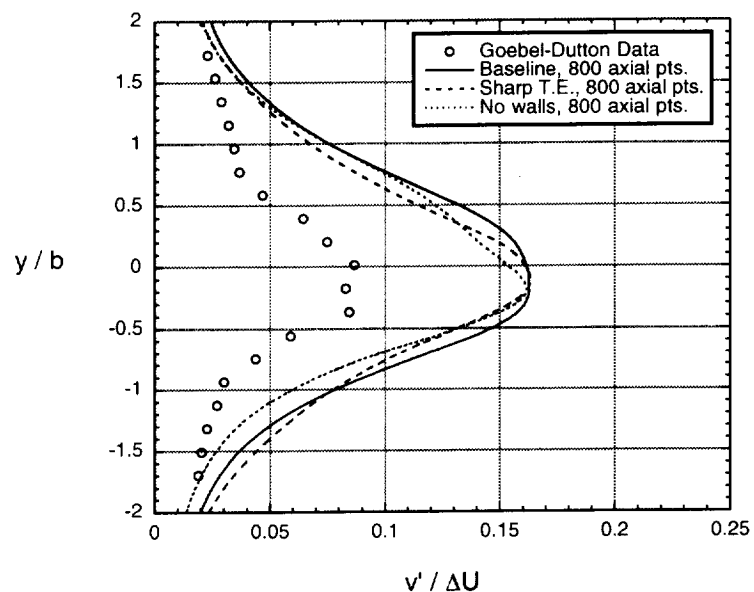


(b) $X = 100 \text{ mm}$

Figure 5.22: Profiles of v_{rms} for 2D hybrid calculations investigating boundary condition effects



(c) $X = 150 \text{ mm}$



(d) $X = 200 \text{ mm}$

Figure 5.22: Concluded.

CHAPTER 6

THREE DIMENSIONAL MIXING LAYER CALCULATIONS

In the previous chapter, the two-dimensional calculations were used to construct the initial computational model of the mixing layer and to examine preliminary effects of grid resolution and boundary condition treatment. To correctly investigate the capability of the hybrid method, however, LES calculations obtained in three spatial directions with the use of a subgrid scale model are required. These calculations are the focus of this chapter. The procedure used to extend the two-dimensional computational model described previously in section 5.2 to three dimensions is presented first in section 6.1. The results of three dimensional calculations obtained with the hybrid RANS-LES method are presented in section 6.2.

6.1 Three Dimensional Computational Modeling

The grid topologies and boundary conditions used for the three dimensional simulations were very similar to those used for the two-dimensional simulations discussed in chapter 5. The three computational grids with 200, 400, and 800 axial point grids described in chapter 5 were used to construct the three dimensional grids used here. To add the third computational direction in each case, the two

dimensional planar grid was copied to provide 11 points in the third (or z) direction. As a result, a side view of the three dimensional grids is represented by figure 5.3. The grid spacing in the z direction was uniform and set equal to the axial spacing at the splitter trailing edge, or $\Delta z = \Delta x_1 = 0.10\text{ mm}$. Because of the very small number of grid points used in the z direction and the small physical space that is represented, only very small wave components in this direction could be simulated. and a periodic flow is assumed in this direction.

The periodic boundary condition used in the z direction allows waves passing through one side of the z domain to enter the other side. Because the Gottlieb-Turkel predictor corrector scheme uses a five point centered stencil in each direction, points along each boundary and one point interior to each boundary must be obtained when periodic boundary conditions are used. The solution vectors \mathbf{Q} shown for the RANS and LES equation sets in equations 3.8 and 3.14 respectively are updated along the boundary corresponding to $k = 1$ in computational coordinates (i, j, k) as:

$$\begin{aligned}\mathbf{Q}_{i,j,1} &= \mathbf{Q}_{i,j,kmax-3} \\ \mathbf{Q}_{i,j,2} &= \mathbf{Q}_{i,j,kmax-2}\end{aligned}\tag{6.1}$$

Similarly, along the other extreme boundary, corresponding to $k = kmax$, the solution vectors \mathbf{Q} are updated using:

$$\begin{aligned}\mathbf{Q}_{i,j,kmax-1} &= \mathbf{Q}_{i,j,3} \\ \mathbf{Q}_{i,j,kmax} &= \mathbf{Q}_{i,j,4}\end{aligned}\tag{6.2}$$

All of the other boundary conditions and the solution procedure are identical to that used for the two dimensional mixing layer calculations discussed in chapter 5, with the one exception being that the Smagorinsky subgrid scale model was used in these three dimensional simulations. As discussed in section 5.2, no subgrid model was used in the two dimensional mixing layer calculations.

The switch from the RANS regions to the LES region at the mixing plane (corresponding to a vertical plane drawn through the trailing edge of the splitter plate) is accomplished by changing the eddy viscosity used in the flow solver from the Cebeci-Smith turbulence model to the Smagorinsky subgrid scale model. As a result, the effect of the eddy viscosity changes from that of replacing all of the turbulent stresses in the RANS regions to that of only replacing the subgrid stresses in the LES regions.

6.2 Three Dimensional Simulations

The first three dimensional simulation was obtained using the computational grid with 200 axial points. The Smagorinsky subgrid scale model used the coefficient $C_s = 0.1$ and the standard expression for the subgrid length scale indicated previously in chapter 2 is repeated here:

$$\Delta = (\Delta x \Delta y \Delta z)^{\frac{1}{3}} \quad (6.3)$$

Figures 6.1 and 6.2 show instantaneous density and entropy contours at the middle plane in the z direction for these initial three dimensional simulations. With the very small domain in the z direction, the contours on all of the two-dimensional

$x - y$ planes are very similar in appearance. The behavior of the flow just downstream of the splitter trailing edge is very similar to that obtained for the two dimensional calculations shown in figures 5.5 and 5.6. The lack of adequate axial grid resolution results in a rapid dissipation of the initial vortex pattern, and is even more rapid in the three dimensional case due to the dissipative nature of the Smagorinsky subgrid scale model. Further out in the mixing section, the three dimensional calculations show no evidence of a secondary unsteadiness that was evident in the two-dimensional calculations, which is also due to the dissipation of the subgrid scale model. The shear layer appears to be effectively laminar downstream of the initial vortex region. Because no turbulent behavior was observed in the mixing section, no turbulent averaging was performed for this case.

The three-dimensional grid using 400 axial points was utilized next, with substantially different flow development observed than that for the 200 axial point grid. As a result, three computations were performed in which the Smagorinsky constant and the subgrid model length scale were varied. The first two cases used the standard length scale expression given in equation (6.3) and investigated the two quoted extreme values for the Smagorinsky constant, $C_s = 0.10$ and $C_s = 0.24$. The third case set C_s to 0.24 but used the modified length scale expression previously shown in chapter 2, and repeated here:

$$\Delta = \left[\frac{(\Delta x)^2 + (\Delta y)^2 + (\Delta z)^2}{3} \right]^{\frac{1}{2}} \quad (6.4)$$

For a computational grid with $\Delta x = \Delta y = \Delta z$, equations (6.3) and (6.4) will return the same value for the Smagorinsky model length scale. The motivation for using

the modified expression was for the case of significant grid stretching, as occurs in both the axial and vertical directions away from the splitter plate trailing edge.

Instantaneous contours of density and entropy at the middle plane in the z direction are provided in figures 6.3 and 6.4 for the first case with the standard length scale expression and $C_s = 0.10$. These contours indicate a fundamentally different flow structure than that observed for the two dimensional cases. In particular, the vortex shedding is observed to disintegrate into a random turbulent pattern much closer to the trailing edge. While the Schlieren photographs taken in the Goebel-Dutton experiments did not probe the flow details near the splitter plate trailing edge, such details were examined by Clemens and Mungal [21] for a very similar experiment configuration and flow operating conditions. The Schlieren image shown in figure 6.5 indicates an initial flow structure similar to that observed in the calculation with an initial vortex shedding from the trailing edge of a splitter plate followed by a transition into turbulence. The turbulent structure in the experiment is also observed to be of primarily small scales, while the LES calculations, by definition, only capture the large scale structures. While the length of the organized vortex structure in the calculations does not exactly match that of the Clemens-Mungal experiment, qualitatively the three dimensional calculations are in much closer agreement than the previous two dimensional results. In addition, the splitter plate thickness was 0.8 mm in the experiment of Clemens and Mungal, while that modeled in the calculations was 0.5 mm , which may be responsible for the precise differences between the experiment and calculations.

The spreading of the turbulent shear layer is observed to be greater in this three dimensional case than in any of the two dimensional cases. This may be observed in the instantaneous contours. A direct comparison of the density contours for the two and three dimensional cases obtained with 400 axial points is provided in figure 6.6 near the splitter tip. This comparison clearly shows the very different flow structure revealed by the three dimensional computations. Although the extent of the z domain is very small compared to the height of the mixing section, and cannot capture large structures in this direction, an unsteady mechanism in which disturbances may develop in all three directions and result in the rapid transition to turbulence is enabled by these three dimensional calculations. The two dimensional calculations, by their very nature, do not allow for such three dimensional disturbances to develop. These results verify that LES calculations must be run in three dimensions in order to properly describe the initial turbulent flow structure.

Time series snapshots of density contours and entropy contours immediately downstream of the splitter plate trailing edge are provided for this initial three dimensional case with 400 axial points in appendix D. The breakdown of the organized vortical structure originating from the splitter plate wake into a turbulent structure is demonstrated in these time series. As mentioned previously, the transitional behavior near the trailing edge of the splitter was not evident with the two dimensional calculations. The frequency of the vortex shedding was the same for the two and three dimensional cases. An analysis of this shedding frequency, also provided in appendix D, shows that a Strouhal number calculated using the splitter

base height and difference in velocities of the two streams is 0.225, which is very close to the Strouhal number range characteristic of flow past cylinders, 0.20 - 0.21.

Examining the other two solutions for the three dimensional approach with 400 axial grid points next, the instantaneous density and entropy contours for the case using the standard length scale and $C_s = 0.24$ are provided in figures 6.7 and 6.8. The same contours for the case using the modified length scale expression and $C_s = 0.24$ are shown in figures 6.9 and 6.10. Although the instantaneous contours for these two cases and the initial 400 point case differ in exact structure in the snapshots shown, overall the turbulent structures are qualitatively the same for the three cases. In addition, the number of organized vortices before breakdown to turbulence may be observed to differ for these three cases at the particular instants in time shown, but in examining each of the solutions over development in time, each of the solutions oscillated in having between 5 and 10 organized vortices.

The mean axial velocity profiles obtained from the three dimensional hybrid RANS-LES calculations using 400 axial grid points in which the subgrid model parameters were varied are compared to the Goebel-Dutton data in figure 6.11. A comparison of the two turbulence intensities is made in figures 6.12 and 6.13 respectively. Examining the mean axial velocities first, all of the three dimensional solutions exhibit a larger wake at $x = 50 \text{ mm}$ than that of the experiment, but compared to the two dimensional solutions, the three dimensional wakes are significantly smaller. This improvement is the result of the more turbulent behavior for the three dimensional cases in the beginning of the mixing section. Further downstream, the three dimensional solutions indicate reasonable agreement with the

data, although all of the solutions appear to mix more rapidly than indicated by the experimental data.

The profiles of u_{rms} in figure 6.12 generally indicate overpredictions from the calculations, which corresponds to the wider axial velocity profiles in figure 6.11. At $x = 50 \text{ mm}$, a double peak in the calculated intensities is somewhat evident, although the effect is much less pronounced for these three dimensional calculations than for the two dimensional calculations in chapter 5. Further downstream, the three dimensional solution obtained with the modified length scale demonstrates generally lower levels of u_{rms} than the other solutions. The modified length scale expression results in larger values of the subgrid model eddy viscosity, which in turn damps more of the small scale unsteadiness. Although increasing the Smagorinsky constant C_s also tends to result in more damping, the effect of changing C_s from 0.10 to 0.24 does not seem to have as large an effect as the subgrid scale length expression.

The computed profiles of v_{rms} , shown in figure 6.13 are also overpredicted relative to the data, with the lowest levels of v_{rms} predicted with the modified length scale and $C_s = 0.24$. As mentioned previously, Liou et al. [59] and Inoue [45] also reported large overpredictions in the turbulence intensities for planar mixing layers. With the confinement of the current three dimensional calculations to a very small domain in the z direction, the inability to calculate large scale fluctuations in this direction may be responsible for the overpredictions of u_{rms} and v_{rms} . In addition, the Schlieren photographs taken in the Goebel-Dutton experiment indicated a very fine

turbulent structure contained within the larger scale development, while the LES calculations inherently can resolve only the larger turbulent scales.

A final three dimensional case was run using 800 axial points in the mixing section. The modified length scale expression and $C_s = 0.24$ was used for the subgrid model. The finer grid used here reduced the permissible time step by nearly a factor of two relative to the 400 axial point cases. This reduced time step and doubling the number of grid points in the mixing section would require a factor of four increase in the computer CPU time requirements to run this case to completion, relative to the cases with 400 axial points. Considering that each of the 400 axial point cases required 500 CPU hours on a Cray C90 computer, 2000 Cray C90 hours would be required to complete the case with 800 axial grid points. As a result, this last three dimensional case was run long enough to allow the flow to fully develop in the mixing section, but not long enough to enable time averaging of the turbulent statistics.

In contrast to the grid refinement studies performed for the two dimensional cases, the large scale turbulent development did not change significantly when increasing the number of axial points in the three dimensional computations from 400 to 800. The instantaneous density and entropy contours in figures 6.14 and 6.15 indicate a large scale turbulent structure which closely resembles those of the 400 axial grid point case. In particular, the breakdown of the organized vortex structure to turbulence is very similar to those previously shown for the 400 axial grid point case. Within the large scale structures, more fine scale turbulence is evident in the 800 axial point case. This behavior corresponds directly with the philosophy of LES

in that as the computational grid is refined, smaller structures are able to be resolved and the role of the subgrid scale model is reduced. In the idealized limit of an infinitely fine grid, a direct numerical simulation is obtained.

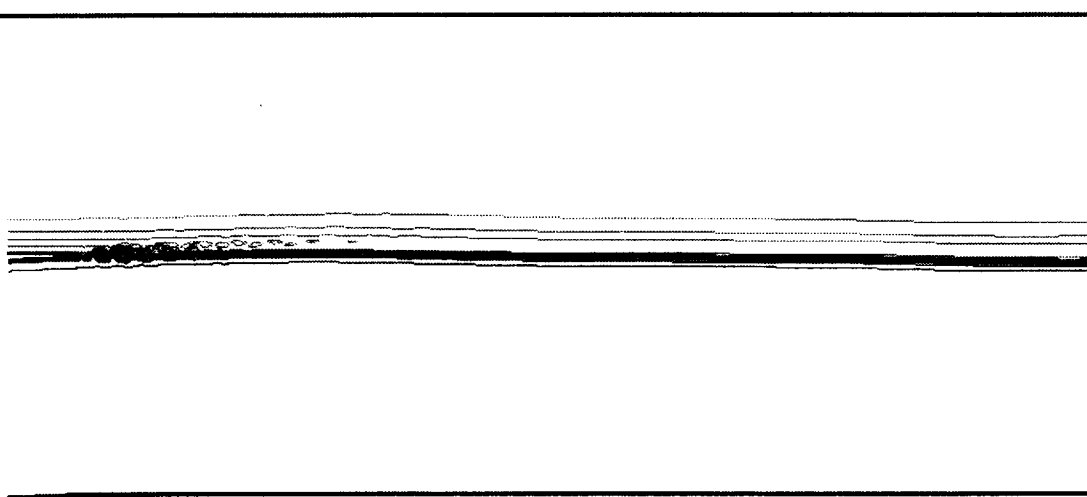


(a) Beginning of mixing section

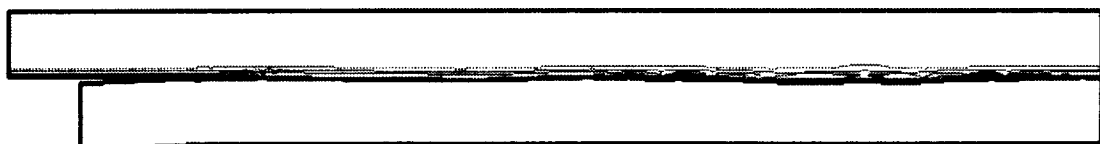


(b) Entire mixing section

Figure 6.1: Instantaneous density contours for the 200 axial grid point case (3D)

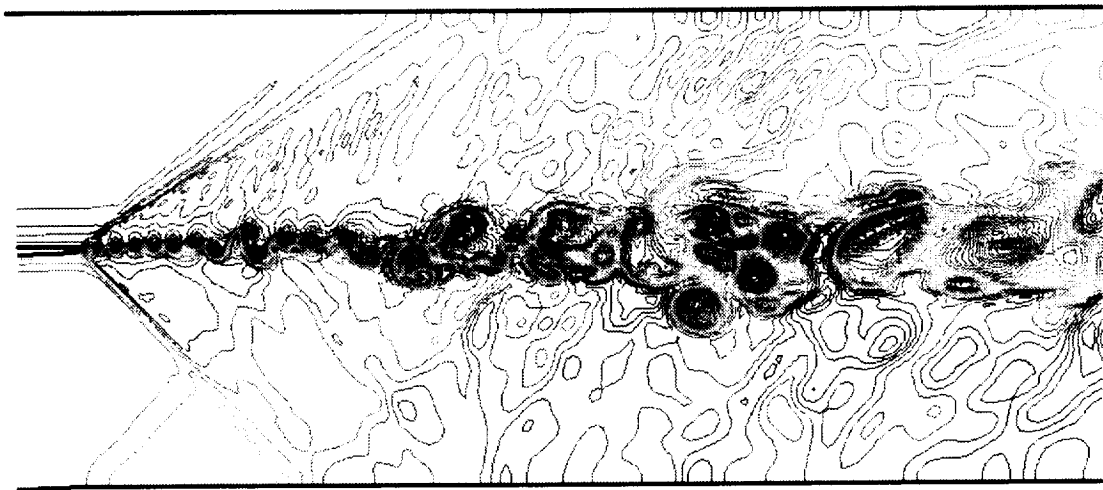


(a) Beginning of mixing section



(b) Entire mixing section

Figure 6.2: Instantaneous entropy contours for the 200 axial grid point case (3D)

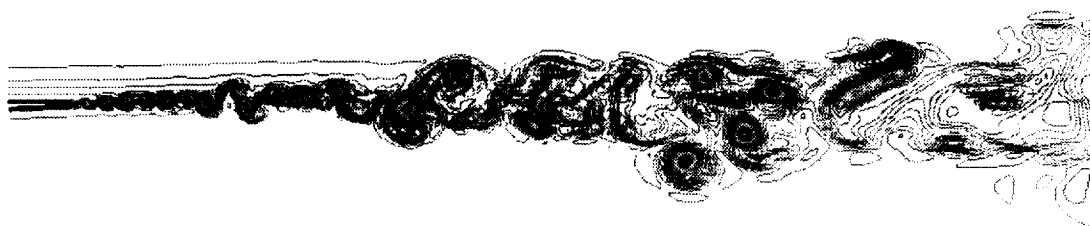


(a) Beginning of mixing section



(b) Entire mixing section

Figure 6.3: Instantaneous density contours for the 400 axial point case using the standard turbulent length scale and $C_s = 0.10$



(a) Beginning of mixing section



(b) Entire mixing section

Figure 6.4: Instantaneous entropy contours for the 400 axial point case using the standard turbulent length scale and $C_s = 0.10$

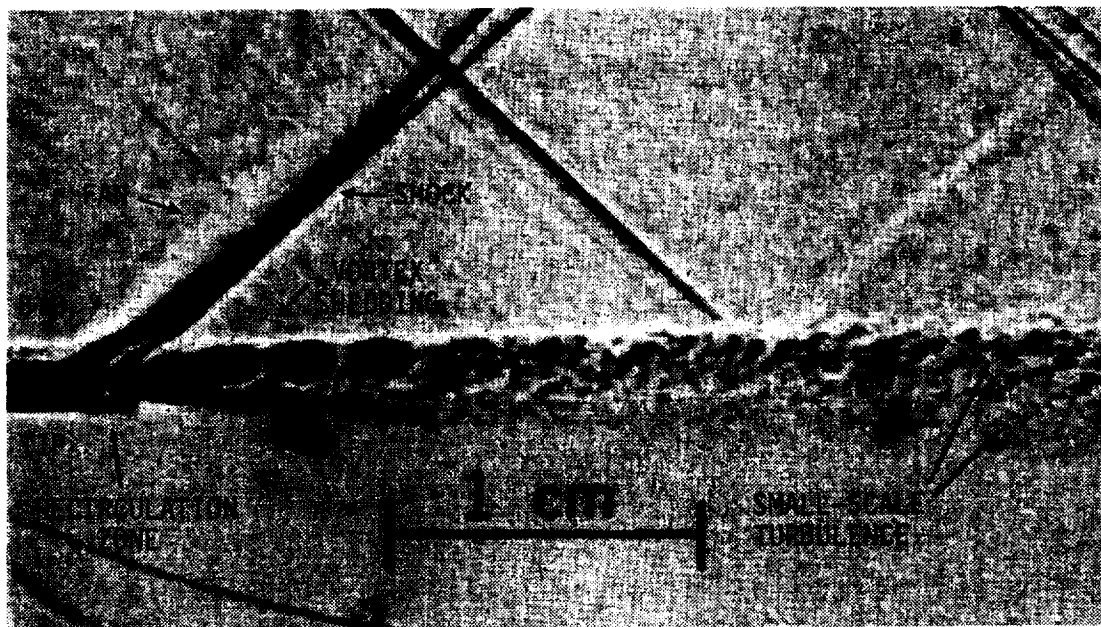
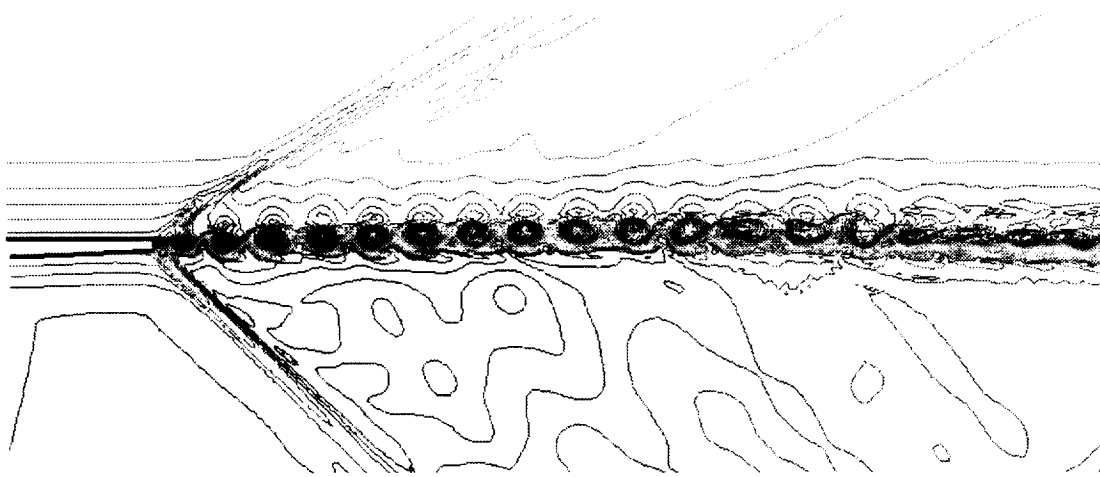
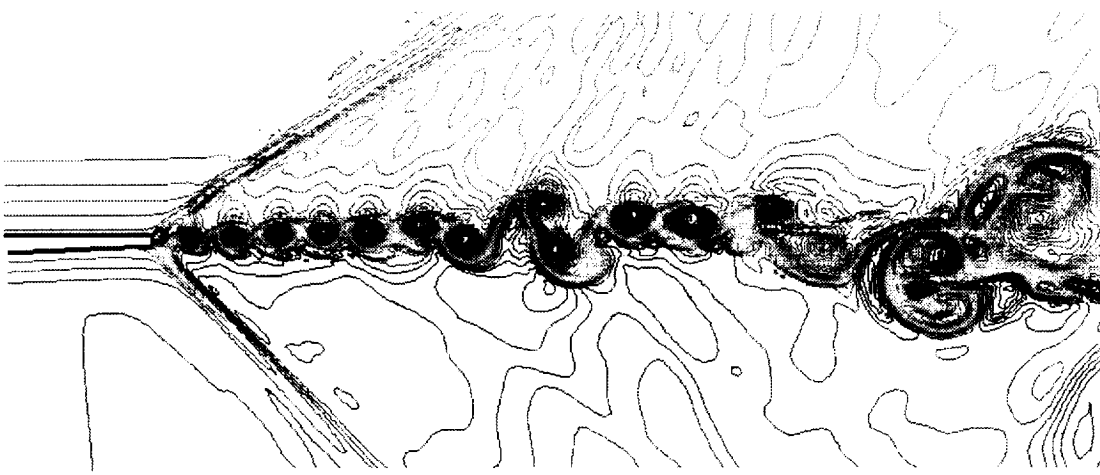


Figure 6.5: Schlieren photograph of the Clemens-Mungal experiment near the trailing edge of the splitter plate, showing vortex shedding followed by a transition to turbulence (from Ref. 21, used with permission)



(a) 2D case with no subgrid model



(b) 3D case with the standard turbulent length scale and $C_s = 0.10$

Figure 6.6: Comparison of density contours near splitter trailing edge



(a) Beginning of mixing section

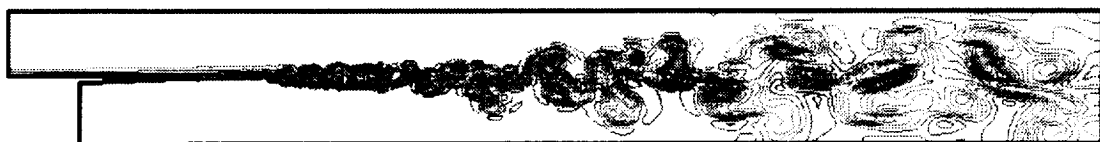


(b) Entire mixing section

Figure 6.7: Instantaneous density contours for the 400 axial point case using the standard turbulent length scale and $C_s = 0.24$

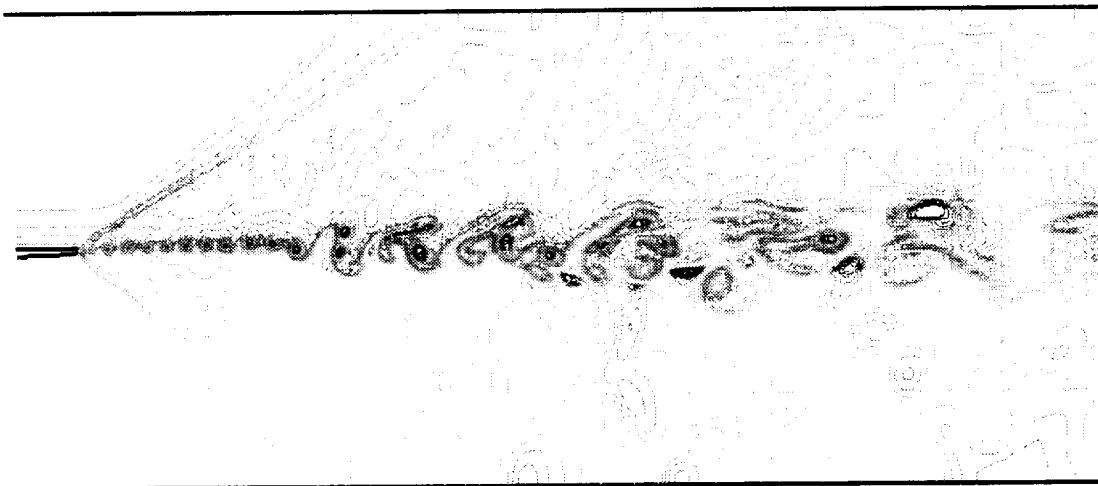


(a) Beginning of mixing section



(b) Entire mixing section

Figure 6.8: Instantaneous entropy contours for the 400 axial point case using the standard turbulent length scale and $C_s = 0.24$



(a) Beginning of mixing section



(b) Entire mixing section

Figure 6.9: Instantaneous density contours for the 400 axial point case using the modified turbulent length scale and $C_s = 0.24$

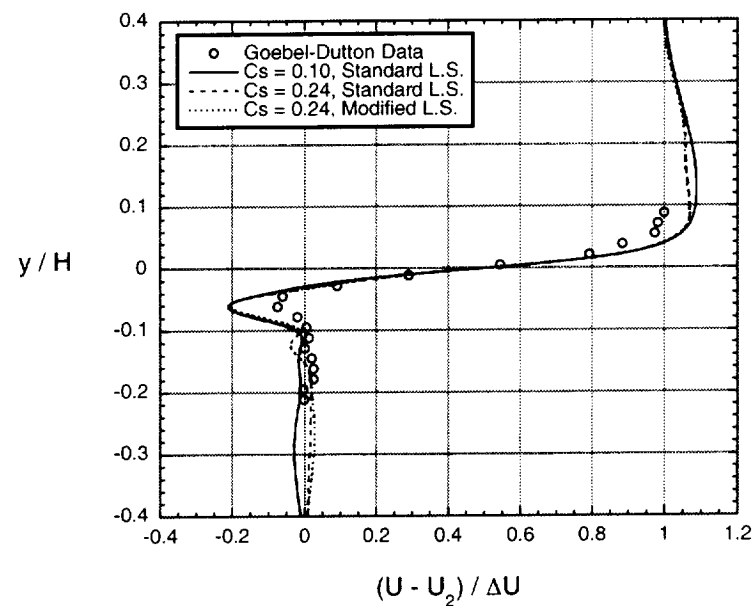


(a) Beginning of mixing section

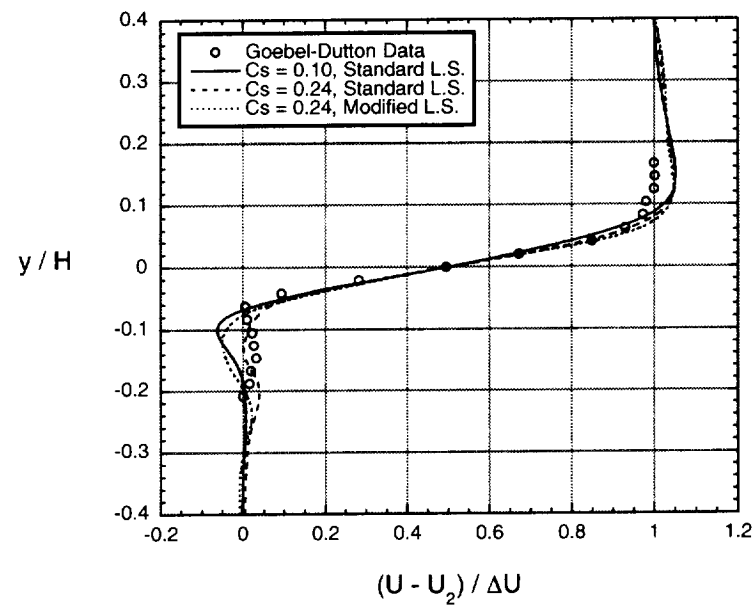


(b) Entire mixing section

Figure 6.10: Instantaneous entropy contours for the 400 axial point case using the modified turbulent length scale and $C_s = 0.24$

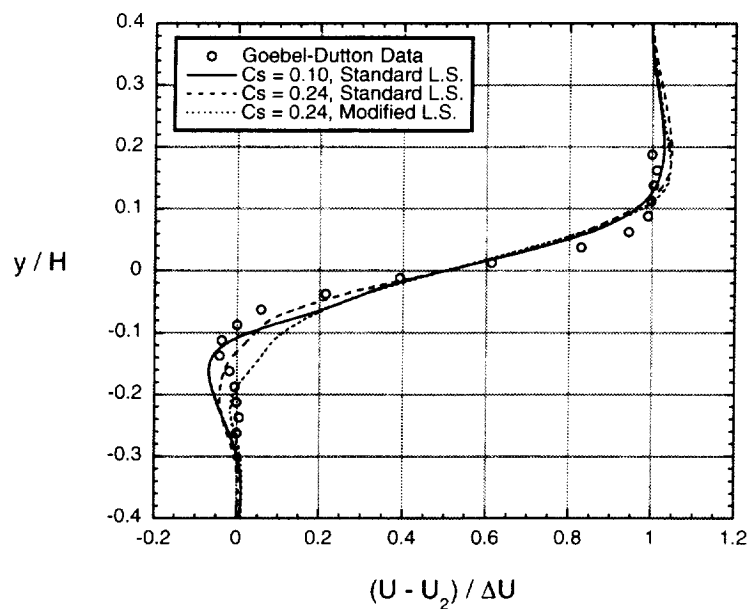


(a) $X = 50 \text{ mm}$

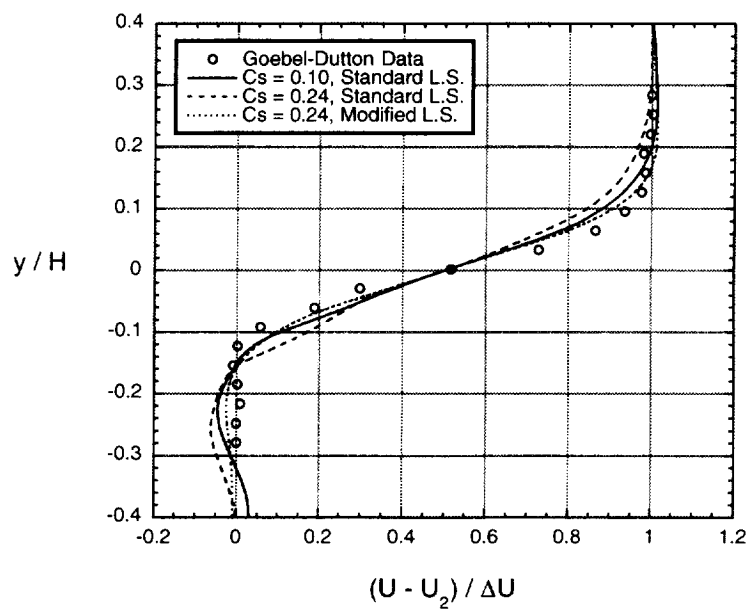


(b) $X = 100 \text{ mm}$

Figure 6.11: Time-averaged axial velocity profiles for 3D hybrid calculations

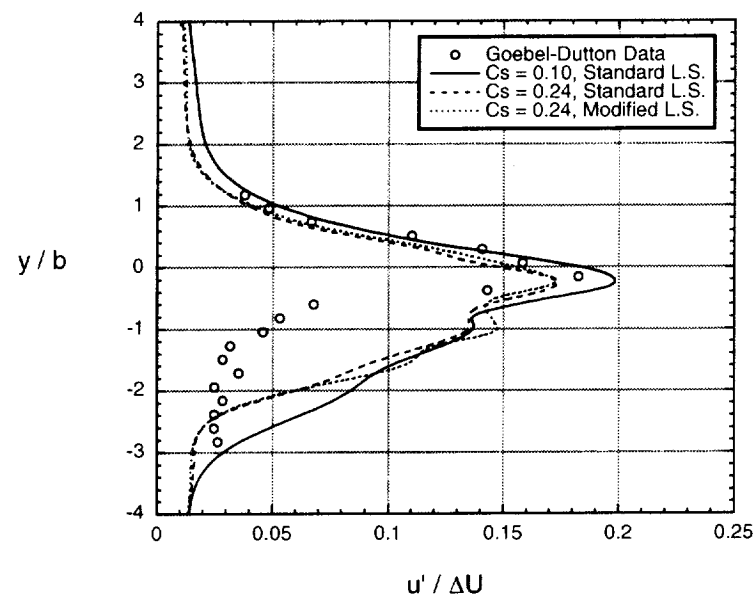


(c) $X = 150 \text{ mm}$

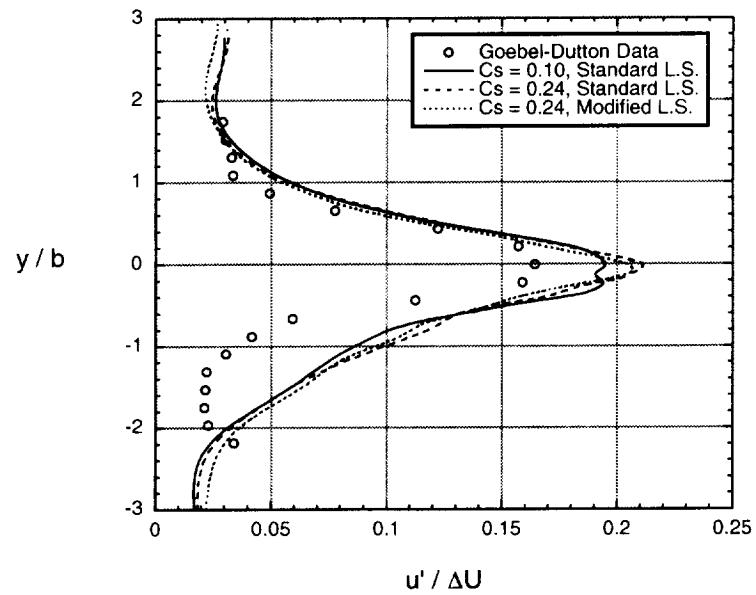


(d) $X = 200 \text{ mm}$

Figure 6.11: Concluded.

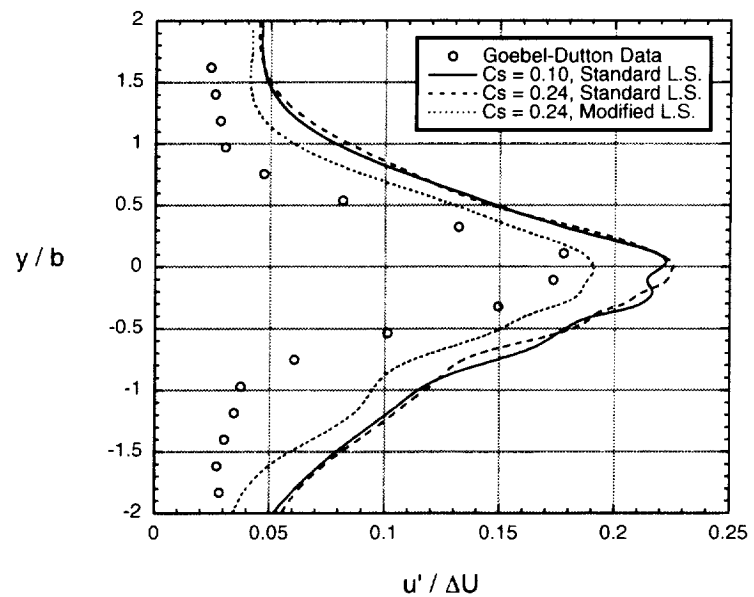


(a) $X = 50 \text{ mm}$

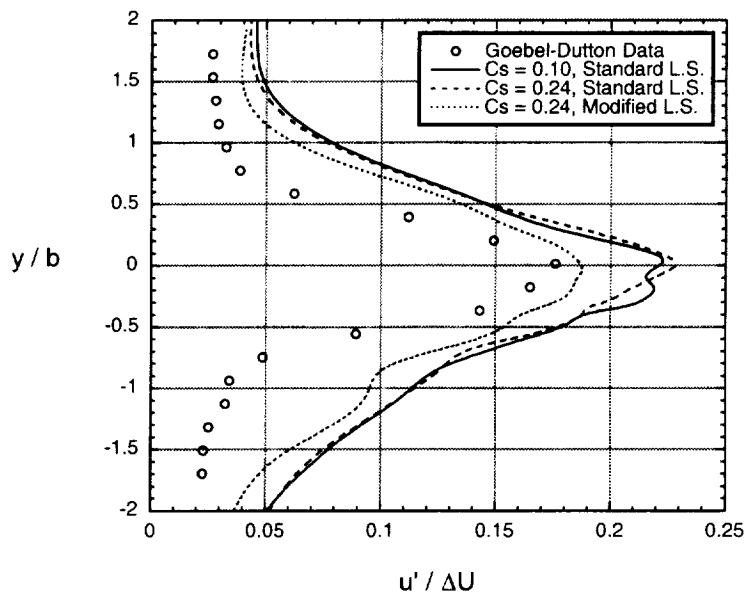


(b) $X = 100 \text{ mm}$

Figure 6.12: Profiles of u_{rms} for 3D hybrid calculations

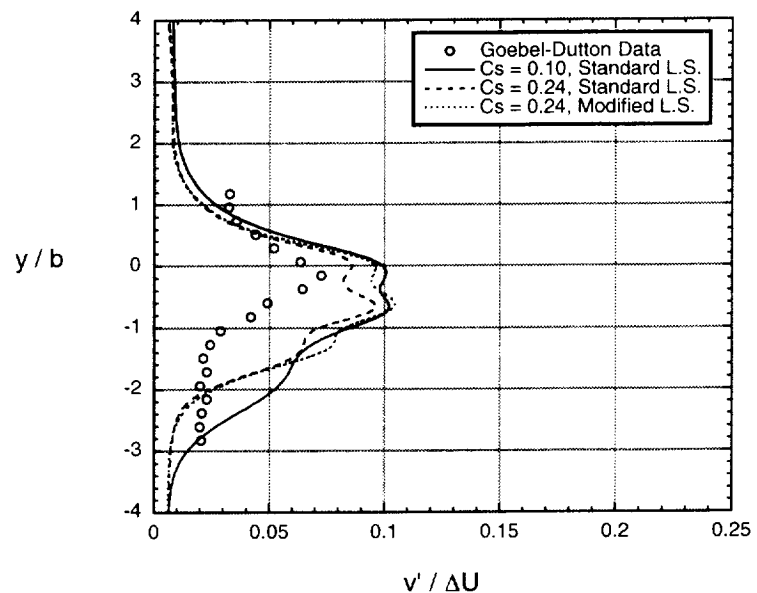


(c) $X = 150 \text{ mm}$

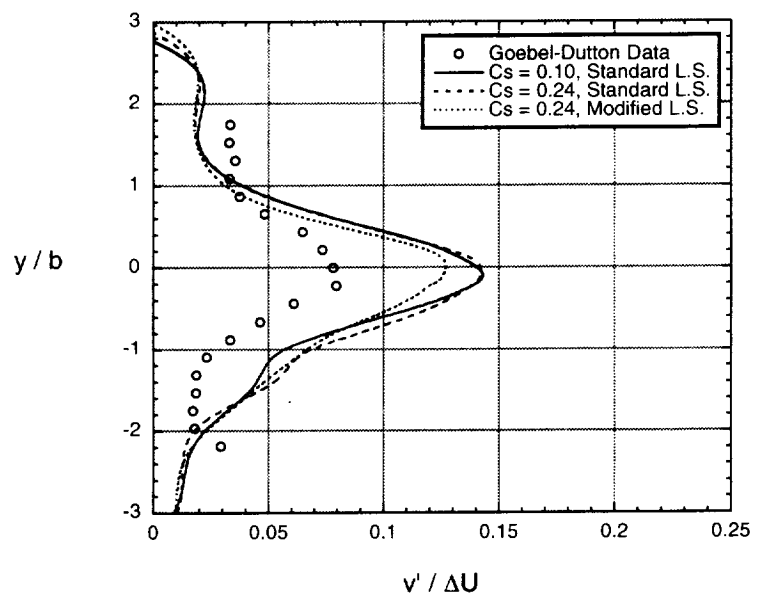


(d) $X = 200 \text{ mm}$

Figure 6.12: Concluded.

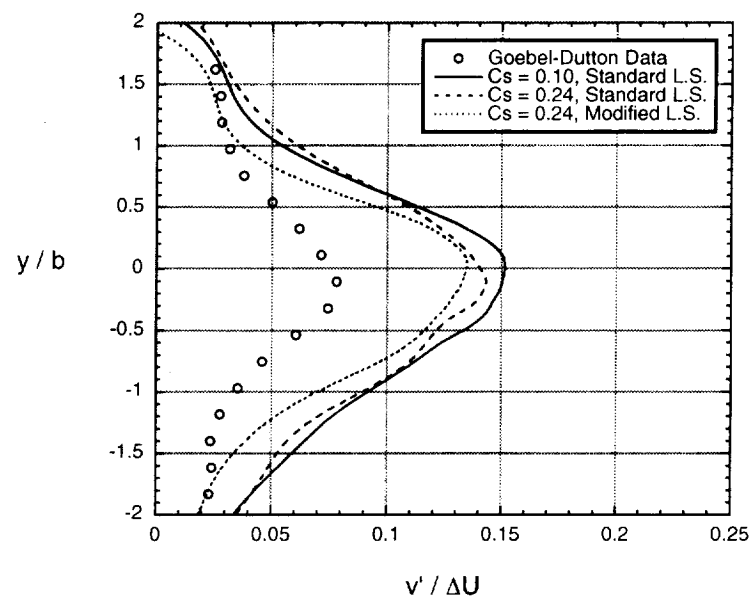


(a) $X = 50 \text{ mm}$

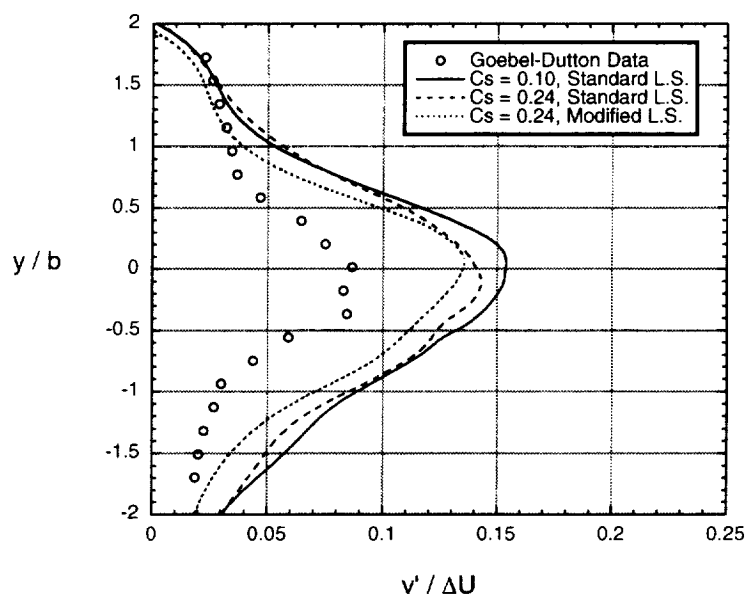


(b) $X = 100 \text{ mm}$

Figure 6.13: Profiles of v_{rms} for 3D hybrid calculations

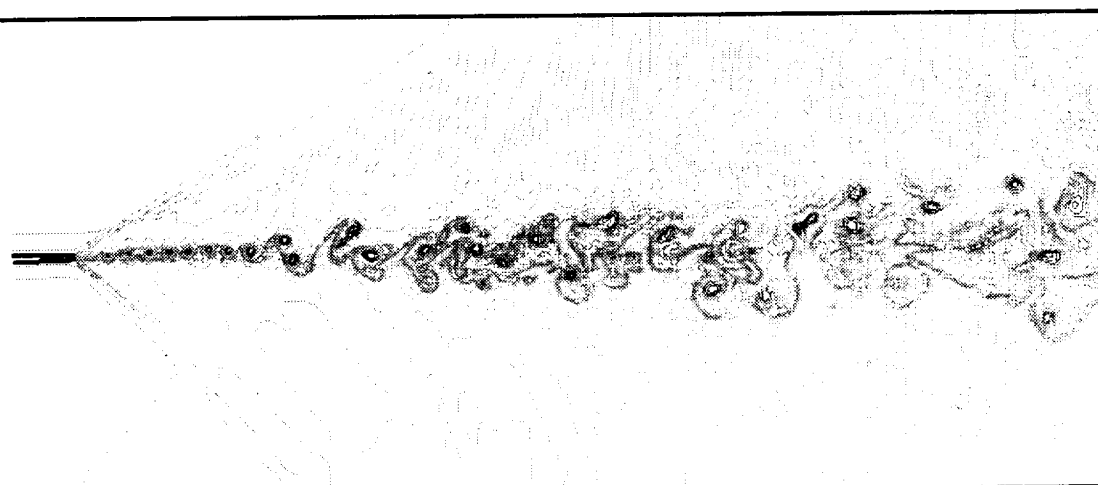


(c) $X = 150 \text{ mm}$



(d) $X = 200 \text{ mm}$

Figure 6.13: Concluded.

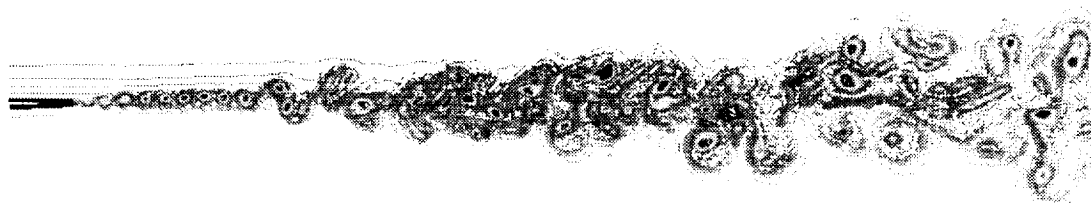


(a) Beginning of mixing section



(b) Entire mixing section

Figure 6.14: Instantaneous density contours for the 800 axial point case using the modified turbulent length scale and $C_s = 0.24$



(a) Beginning of mixing section



(b) Entire mixing section

Figure 6.15: Instantaneous entropy contours for the 800 axial point case using the modified turbulent length scale and $C_s = 0.24$

CHAPTER 7

CONCLUSIONS AND RECOMMENDATIONS

The work described in this dissertation represents the initial efforts to develop and evaluate a hybrid RANS-LES method for compressible mixing layer simulations. Such mixing layers dominate the flows in exhaust systems of commercial and military aircraft in current use and also those of hypersonic vehicles under development for future space transportation use. The hybrid method uses a RANS approach to provide the mean flow characteristics of the wall boundary layers entering the mixing layer and an LES approach for the mixing region. Although the RANS approach does not provide any unsteady turbulent information to the LES region, the mean flow boundary layer characteristics are provided. The hybrid method was developed for the analysis of nozzle and mixing layer configurations in which a dominant structural feature, such as the base region of a nozzle or splitter plate separating the upstream flows, will provide the dominant unsteady mechanism to drive the development of turbulence in the mixing layer.

The hybrid method development was initiated by deriving a set of Reynolds-averaged Navier-Stokes (RANS) equations using density weighting in the averaging process, and a set of spatially-filtered large eddy simulation (LES)

equations which also used density (Favre) weighting. The resulting similar form of the RANS and LES equation sets enabled both to be solved with a single solution scheme. In this dissertation, the Gottlieb-Turkel predictor-corrector scheme was employed. A transformation of the equations to generalized coordinates enabled flow calculations on stretched, non-Cartesian grids. The RANS equations were closed using the Cebeci-Smith algebraic turbulence model, with the option to employ the wall-function technique of Ota and Goldberg. The LES equations were closed using the Smagorinsky subgrid scale model.

The Cebeci-Smith turbulence model, despite its relatively simple form, was demonstrated to provide accurate calculations of boundary layer flows that are free of adverse pressure gradients or separation regions. Further, the use of the Cebeci-Smith model in conjunction with the Ota-Goldberg wall function enabled calculations of supersonic wall boundary layers to nearly the same accuracy as that of the standard approach of integrating the Cebeci-Smith model through the viscous sublayer, while enabling a significantly larger vertical grid spacing near the wall. As a result, the wall function approach enabled a continuous computational grid to be used from the RANS to the LES regions, and the method thereby avoided the use of discontinuous grid zones that would have otherwise required an interpolation scheme between the two regions. In addition, the origins of the Cebeci-Smith RANS turbulence model and the Smagorinsky LES subgrid scale model are both in mixing length theory, and this similar form of the two models assisted in code implementation. As a result, the use of a more sophisticated turbulence model to

close the RANS equations was found to be unnecessary, provided the RANS regions are restricted to attached, zero pressure gradient wall boundary layer regions.

While true LES calculations require computations in three spatial directions, two dimensional simulations of a benchmark mixing layer experiment were considered first to address the effects of axial grid resolution and boundary conditions. The parametric study of axial grid resolution indicated more realistic turbulent development with increasing axial grid density. For the coarsest grid examined, there was almost no evidence of turbulent flow development. For all of the cases examined, a vortex shedding was found to originate from the base region of a splitter plate separating the upstream wall bounded regions. For the finest two dimensional grid examined, the unsteady vortex pattern eventually transitioned to a turbulent structure. The location of this transition, however, was much further downstream than observed in the experiments.

Additional two dimensional calculations were obtained to investigate the boundary treatment of the splitter plate trailing edge and of the mixing section walls. Calculations obtained for a case in which the finite thickness splitter base was changed to a sharp tip indicated that the vortex shedding was removed, but the development of turbulence downstream occurred at nearly the same position as for the case with vortex shedding induced by the splitter base geometry. Computations were also obtained for a modified geometry in which the mixing section walls were effectively removed, to determine if Mach waves reflecting off these walls in the baseline calculations affected the turbulent mixing layer development. These

calculations indicated that removing the mixing section walls did not change the fundamental structure of the flow relative to the baseline case.

Three dimensional calculations were obtained next for grids constructed by copying the two dimensional planar grids to locations in the third computational direction, normal to both the streamwise and transverse directions. Only a small domain was modeled in this third direction, and periodic boundary conditions were employed along the extreme boundaries. For the coarse three dimensional grid, again no turbulent flow development was observed. For the intermediate grid, the vortex shedding found previously in the two dimensional simulations was also observed in the three dimensional calculations. However, the organized vortical structure rapidly disintegrated into a significantly more realistic turbulent flow structure. This rapid transition to turbulent flow was nearly identical to that found in experimental investigations of a similar mixing layer configuration. Although the extent of the third dimension in these calculations was very small, an unsteady mechanism by which disturbances could develop in all three directions and result in a rapid transition to turbulent flow was enabled by the three dimensional calculations. In contrast, a two dimensional approach, by definition, does not allow for such three dimensional disturbances to develop. The results of these calculations verified that LES simulations must be performed in three dimensions.

Parametric studies of the subgrid model length scale and the Smagorinsky model coefficient were examined with this intermediate grid, but no significant differences were noted. Comparisons of time-averaged axial velocities and turbulence intensities from the calculations to experimental data indicated reasonable agreement, with the

solutions indicating somewhat higher levels of turbulent mixing. A major source of discrepancy between the calculations and experiment is believed to be the lack of adequate grid resolution to resolve the small turbulent scales contained within the larger turbulent structures. Another source of discrepancy was the very small domain used in the third computational direction.

Despite these limitations, the three dimensional calculations demonstrated the success of the hybrid method to capture the dominant characteristics of the mixing layer, and in particular, the rapid transition of the organized vortex structure to a turbulent mixing layer structure. It is expected that improvements in the fidelity of the solution scheme, and more importantly, improvements in computing power, will enable better predictions of the turbulent statistics, as will be discussed briefly.

A final three dimensional calculation was investigated using a computational grid constructed from the most densely packed two dimensional grid. Because a prohibitively long run time would be required to complete this solution for turbulent statistics purposes, the calculations were run only long enough to allow the flow to fully develop in the mixing section. The large scale turbulent structures evident for this case were very similar to those for the intermediate three dimensional cases. More resolution of the finer turbulent scales contained within the larger structures was observed for the fine grid case, which is in line with the philosophy of LES to resolve finer scales as the grid density is increased.

The effects of improved subgrid scale models on the quality of LES simulations is an issue of considerable debate. Research into advanced subgrid scale models has

yielded improvements in the accuracy of LES simulations obtained for low Reynolds number wall boundary layer flows. However, authors such as Spalart [96] and Fureby and Grinstein [29] offer the opinion that subgrid scale refinement will offer only small improvements for large eddy simulations of flows away from boundaries and without chemical reactions. Both authors further suggest that it may even be feasible to perform an LES simulation without an explicit subgrid scale model, provided the numerical scheme is sufficient to prevent unresolved wavenumbers from contaminating the solution and that the simulation resolves turbulent scales in the inertial subrange.

Improvements to the numerical method may enable more accurate resolution of the smaller turbulent scales, which appeared to be the greatest limitation of the current method in simulations of the compressible mixing layer experiment. The class of numerical methods known as compact schemes, such as those presented by Lele [55], have been shown to provide higher spatial accuracy and improved capability to resolve higher wave numbers for a given grid size than is possible using MacCormack-type predictor-corrector schemes such as the Gottlieb-Turkel method.

The continuing advances in computing speed and computer memory will also enable calculations of higher fidelity, and eventually to the limit of direct numerical simulations (DNS) where all turbulent scales of importance are resolved. Estimates of Spalart [96], however, suggest that improvements of several orders of magnitude in computer speed and memory will be required to perform full LES or DNS calculations of realistic engineering configurations. His estimates project full LES

simulations requiring $10^{11.5}$ grid points to be possible in the year 2045, and DNS simulations requiring 10^{16} grid points to be possible in the year 2080.

In the interim, RANS and hybrid RANS-LES methods will each be the most appropriate computational tool for certain classes of turbulent flows. For wall bounded turbulent flows without massive separation regions, RANS methods will likely be the most appropriate choice for some time. Hybrid methods, such as that developed in this work, will very possibly become the appropriate tool for flows with significant mixing regions or large scale separation zones. As a result, research to further develop both RANS and hybrid RANS-LES methods will be important to improve the capability to simulate complex turbulent flows.

APPENDIX A

ACCURACY ANALYSIS OF THE GOTTLIEB-TURKEL SCHEME

In this appendix, the temporal and spatial accuracy of the Gottlieb-Turkel scheme are investigated.

The Gottlieb-Turkel scheme is illustrated using a one dimensional problem that is a model for the Navier-Stokes equations written in vector form. This model problem is given as:

$$\frac{\partial q}{\partial t} + \frac{\partial f}{\partial x} = 0 \quad (\text{A.1})$$

The predictor step is:

$$q_i^* = q_i^n - \frac{\Delta t}{6\Delta x} (-7f_i + 8f_{i-1} - f_{i-2}) \quad (\text{A.2})$$

The corrector step is:

$$q_i^{n+1} = \frac{1}{2} \left[q_i^n + q_i^* - \frac{\Delta t}{6\Delta x} (7f_i^* - 8f_{i+1}^* + f_{i+2}^*) \right] \quad (\text{A.3})$$

The time step of the Gottlieb-Turkel predictor-corrector scheme, Δt , is related to the grid spacing, Δx , and the propagation speed, A , through the CFL (Courant-Friedrichs-Lowy) number:

$$\Delta t = CFL \frac{\Delta x}{A} \quad (A.4)$$

Nelson [71] investigated the spatial and temporal accuracy of several predictor-corrector schemes, including the Gottlieb-Turkel scheme, investigated here using a linearization of the model problem shown in equation A.1. This procedure will also be used here. The linearization of equation (A.1) begins by assuming a constant propagation speed, A :

$$f = Aq \quad (A.5)$$

The equation for the predictor step (A.2) can be substituted into the equation for the corrector (A.3), which results in

$$q_i^{n+1} = q_i^n - \frac{\Delta t}{12\Delta x} (-7f_i + 8f_{i+1} - f_{i+2}) - \frac{\Delta t}{12\Delta x} (7f_i^* - 8f_{i-1}^* + f_{i-2}^*) \quad (A.6)$$

The terms in this equation having a superscript (*), which represent the fluxes f after the predictor update, can be rewritten using $f^* = Aq^*$. Equation (A.6) then becomes

$$q_i^{n+1} = q_i^n - \frac{\Delta t}{12\Delta x} (-7f_i + 8f_{i+1} - f_{i+2}) - \frac{A}{12} \frac{\Delta t}{\Delta x} (7q_i^* - 8q_{i-1}^* + q_{i-2}^*) \quad (A.7)$$

The q^* terms are replaced using the predictor expression (A.2). This enables the complete predictor-corrector update to be expressed as function of the original values of q and f :

$$q_i^{n+1} = q_i^n - \frac{\Delta t}{12\Delta x} (-7f_i + 8f_{i+1} - f_{i+2}) - \frac{A}{12} \frac{\Delta t}{\Delta x} (7q_i - 8q_{i-1} + q_{i-2}) + \frac{A}{72} \left(\frac{\Delta t}{\Delta x} \right)^2 [7(-7f_i + 8f_{i+1} - f_{i+2}) - 8(-7f_{i-1} + 8f_i - f_{i+1}) + (-7f_{i-2} + 8f_{i-1} - f_i)] \quad (\text{A.8})$$

Using $f = Aq$ and combining terms results in:

$$q_i^{n+1} = q_i^n - \frac{\Delta t}{12\Delta x} (-f_{i+2} + 8f_{i+1} - 8f_{i-1} + f_{i-2}) + \frac{A}{72} \left(\frac{\Delta t}{\Delta x} \right)^2 (-7f_{i+2} + 64f_{i+1} - 114f_i + 64f_{i-1} - 7f_{i-2}) \quad (\text{A.9})$$

Next, the q_i^n term is moved to the left side of the equation, and the q and f terms are expressed in terms of Taylor series expansions about the points q^n and f_i , respectively:

$$\begin{aligned} \Delta t \frac{\partial q}{\partial t} + \frac{\Delta t^2}{2} \frac{\partial^2 q}{\partial t^2} + \frac{\Delta t^3}{6} \frac{\partial^3 q}{\partial t^3} + \dots &= -\frac{1}{12} \left(12\Delta x \frac{\partial f}{\partial x} - 48 \frac{\Delta x^5}{120} \frac{\partial^5 f}{\partial x^5} + \dots \right) \\ &+ \frac{A}{72} \left(\frac{\Delta t}{\Delta x} \right)^2 \left(36\Delta x^2 \frac{\partial^2 f}{\partial x^2} - 4\Delta x^4 \frac{\partial^4 f}{\partial x^4} + \dots \right) \end{aligned} \quad (\text{A.10})$$

Reorganizing equation (A.10) and dividing all of the terms by Δt results in:

$$\frac{\partial q}{\partial t} + \frac{\partial f}{\partial x} = -\frac{\Delta t}{2} \frac{\partial^2 q}{\partial t^2} - \frac{\Delta t^2}{6} \frac{\partial^3 q}{\partial t^3} + \frac{\Delta x^4}{30} \frac{\partial^5 f}{\partial x^5} - \frac{A\Delta t\Delta x^2}{18} \frac{\partial^4 f}{\partial x^4} + \frac{A\Delta t}{2} \frac{\partial^2 f}{\partial x^2} + \dots \quad (\text{A.11})$$

Finally, the first and fifth terms on the right side of equation (A.11) are removed by taking the second derivative of $f = Aq$, and then recognizing that

$$\frac{\Delta t}{2} \frac{\partial^2 q}{\partial t^2} = \frac{A \Delta t}{2} \frac{\partial^2 f}{\partial x^2} \quad (\text{A.12})$$

The resulting expression is:

$$\frac{\partial q}{\partial t} + \frac{\partial f}{\partial x} = -\frac{\Delta t^2}{6} \frac{\partial^3 q}{\partial t^3} - \frac{A \Delta t \Delta x^2}{18} \frac{\partial^4 f}{\partial x^4} + \frac{\Delta x^4}{30} \frac{\partial^5 f}{\partial x^5} + \dots \quad (\text{A.13})$$

The left side of equation (A.13) is the original model problem given in equation (A.1). As a result, the right side of equation (A.13) is the truncation error resulting from the discretization of the model equation using the Gottlieb-Turkel scheme. The first term on the right side of equation (A.13) indicates that temporal accuracy of the scheme is second order. The second truncation error term involves both Δt and Δx^2 , and we can use relation between the time step, grid size and CFL number shown in equation (A.4) to rewrite this equation (A.13) as:

$$\frac{\partial q}{\partial t} + \frac{\partial f}{\partial x} = -\frac{\Delta t^2}{6} \frac{\partial^3 q}{\partial t^3} - CFL \frac{\Delta x^3}{18} \frac{\partial^4 f}{\partial x^4} + \frac{\Delta x^4}{30} \frac{\partial^5 f}{\partial x^5} + \dots \quad (\text{A.14})$$

The Gottlieb-Turkel explicit scheme is only stable for CFL values smaller than one. For CFL values on the order of one, the spatial accuracy of the scheme is third order. In practice, the maximum CFL number is usually set to a value of 0.5 or less. For stretched grids, the limiting time step is proportional to the smallest grid spacing and then the effective local CFL number is much smaller in regions of the computational domain where the grid spacing is larger. This can be observed by considering equation (A.4) for the case of variable grid spacing, Δx , but a constant time step Δt . As a result, the truncation error term in equation (A.14) becomes

insignificant away from the region of tightest grid spacing. For such regions, the next truncation error term indicates fourth order spatial accuracy. In conclusion, the Gottlieb-Turkel scheme is strictly second order accurate in time and third order accurate in space, but in the case of highly stretched grids, the spatial accuracy is effectively fourth order.

APPENDIX B

TRANSFORMATION METRICS

The metric terms that are required to transform the RANS and LES equations from physical space to computational space are derived in this appendix. The procedure used in this work is the same as that presented in reference [42].

The equations derived in chapter 2 are transformed from physical space (x, y, z) to computational space (ξ, η, ζ) using the relations:

$$\begin{aligned}\xi &= \xi(x, y, z) \\ \eta &= \eta(x, y, z) \\ \zeta &= \zeta(x, y, z)\end{aligned}\tag{B.1}$$

The chain rule of partial differentiation allows the cartesian derivatives to be expressed as:

$$\begin{aligned}\frac{\partial}{\partial x} &= \xi_x \frac{\partial}{\partial \xi} + \eta_x \frac{\partial}{\partial \eta} + \zeta_x \frac{\partial}{\partial \zeta} \\ \frac{\partial}{\partial y} &= \xi_y \frac{\partial}{\partial \xi} + \eta_y \frac{\partial}{\partial \eta} + \zeta_y \frac{\partial}{\partial \zeta} \\ \frac{\partial}{\partial z} &= \xi_z \frac{\partial}{\partial \xi} + \eta_z \frac{\partial}{\partial \eta} + \zeta_z \frac{\partial}{\partial \zeta}\end{aligned}\tag{B.2}$$

In equation (B.2), the terms ξ_x , η_x , ζ_x , ξ_y , η_y , ζ_y , ξ_z , η_z , and ζ_z are the metrics of the transformation. To compute these metric terms, the first step is to compute the derivatives x_ξ , x_η , x_ζ , y_ξ , y_η , y_ζ , z_ξ , z_η , and z_ζ . The stepsizes of these derivatives are equal in computational space and can be obtained using finite difference expressions. To be consistent with the Gottlieb-Turkel scheme, which effectively has fourth order spatial accuracy and uses a five point stencil, these spatial derivatives are also calculated with a five point, fourth order accurate finite difference method.

Derivatives in x:

$$x_\xi = \frac{x_{j-2} - 8x_{j-1} + 8x_{j+1} - x_{j+2}}{12}$$

$$x_\eta = \frac{x_{k-2} - 8x_{k-1} + 8x_{k+1} - x_{k+2}}{12} \quad (B.3)$$

$$x_\zeta = \frac{x_{l-2} - 8x_{l-1} + 8x_{l+1} - x_{l+2}}{12}$$

Derivatives in y:

$$y_\xi = \frac{y_{j-2} - 8y_{j-1} + 8y_{j+1} - y_{j+2}}{12}$$

$$y_\eta = \frac{y_{k-2} - 8y_{k-1} + 8y_{k+1} - y_{k+2}}{12} \quad (B.4)$$

$$y_\zeta = \frac{y_{l-2} - 8y_{l-1} + 8y_{l+1} - y_{l+2}}{12}$$

Derivatives in z:

$$z_\xi = \frac{z_{j-2} - 8z_{j-1} + 8z_{j+1} - z_{j+2}}{12}$$

$$z_\eta = \frac{z_{k-2} - 8z_{k-1} + 8z_{k+1} - z_{k+2}}{12} \quad (B.5)$$

$$z_\zeta = \frac{z_{l-2} - 8z_{l-1} + 8z_{l+1} - z_{l+2}}{12}$$

For grid points that are located at a boundary, a one sided fourth order differenced expression is used, and at grid points one point off of a boundary, a skewed fourth order difference expression is used. Both expressions are obtained in the same manner as the central differenced expressions in equations (B.3 - B.5) through use of the appropriate Taylor's series expansions. As an example, the x_ξ term at a boundary corresponding to ($j = 1$) is:

$$x_\xi = \frac{-25x_j + 48x_{j+1} - 36x_{j+2} + 16x_{j+3} - 3x_{j+4}}{12} \quad (B.6)$$

Similarly, the x_ξ term at ($j = 2$) is

$$x_\xi = \frac{-3x_{j-1} - 10x_j + 18x_{j+2} - 6x_{j+3} + x_{j+4}}{12} \quad (B.7)$$

Once all of these spatial derivatives are obtained, the Jacobian of the transformation, J , is calculated:

$$J = \frac{1}{x_\xi(y_\eta z_\zeta - y_\zeta z_\eta) - x_\eta(y_\xi z_\zeta - y_\zeta z_\xi) + x_\zeta(y_\xi z_\eta - y_\eta z_\xi)} \quad (B.8)$$

Using this expression for the Jacobian, the metric terms are:

$$\xi_x = J(y_\eta z_\zeta - y_\zeta z_\eta)$$

$$\xi_y = J(x_\zeta z_\eta - x_\eta z_\zeta)$$

$$\xi_z = J(x_\eta y_\zeta - x_\zeta y_\eta)$$

$$\eta_x = J(y_\zeta z_\xi - y_\xi z_\zeta)$$

$$\eta_y = J(x_\xi z_\zeta - x_\zeta z_\xi)$$

$$\eta_z = J(x_\zeta y_\xi - x_\xi y_\zeta)$$

$$\zeta_x = J(y_\xi z_\eta - y_\eta z_\xi)$$

$$\zeta_y = J(x_\eta z_\xi - x_\xi z_\eta)$$

$$\zeta_z = J(x_\xi y_\eta - x_\eta y_\xi)$$

APPENDIX C

TURBULENT TIME AVERAGING PROCEDURE

The procedure used to obtain the time-averaged axial velocities and the two turbulent intensities for the LES regions is detailed in this appendix.

As each of the two dimensional calculations discussed in chapter 5 and the three dimensional calculations discussed in chapter 6 progressed in time, quantities were accumulated from the instantaneous velocity fields at each time step. These quantities were then used to calculate the mean axial velocity \bar{u} and the two turbulence intensities u_{rms} and v_{rms} . The mean velocity field is calculated using:

$$\bar{u} = \frac{1}{T} \int_0^T u dt \quad (C.1)$$

While the two turbulence intensities u_{rms} and v_{rms} are obtained from:

$$u_{rms} = \left[\frac{1}{T} \int_0^T (u')^2 dt \right]^{\frac{1}{2}} \quad (C.2)$$

and

$$v_{rms} = \left[\frac{1}{T} \int_0^T (v')^2 dt \right]^{\frac{1}{2}} \quad (C.3)$$

The two quantities u' and v' are not known until \bar{u} is determined, which in turn requires completion of the time averaging period T . As a result, an alternative to equations (C.2) and (C.3) is used to find the turbulence intensities u_{rms} and v_{rms} . Using $u = \bar{u} + u'$ and $v = \bar{v} + v'$, equations (C.2) and (C.3) can be rewritten as:

$$u_{rms} = \left[\frac{1}{T} \int_0^T u^2 dt - \bar{u}^2 \right]^{\frac{1}{2}} \quad (C.4)$$

and

$$v_{rms} = \left[\frac{1}{T} \int_0^T v^2 dt - \bar{v}^2 \right]^{\frac{1}{2}} \quad (C.5)$$

For all of the two and three dimensional mixing layer simulations, a constant time step was used so that equations (C.1), (C.4), and (C.5) can be obtained through a straightforward summation procedure. This procedure consists of storing summations of u , v , u^2 , and v^2 at each grid point from each time step. Equations (C.1), (C.4), and (C.5) then can be replaced with equations (C.6), (C.8), and (C.9).

$$\bar{u} = \frac{1}{N} \sum_{n=1}^N u \quad (C.6)$$

where N is the total number of time steps, corresponding to the total time interval T , which are related through the time step size Δt :

$$T = N \Delta t \quad (C.7)$$

$$u_{rms} = \left[\frac{1}{N} \sum_{n=1}^N u^2 - \bar{u}^2 \right]^{\frac{1}{2}} \quad (C.8)$$

$$v_{rms} = \left[\frac{1}{N} \sum_{n=1}^N v^2 - \bar{v}^2 \right]^{\frac{1}{2}} \quad (C.9)$$

In all of the mixing layer simulations, the initial iterations used to start the flow development were run using a *CFL* number of 0.3 with the Gottlieb-Turkel scheme. As the unsteady flow developed, however, the minimum time step fluctuated in the flow, so that the actual time step given by equation 3.31 also fluctuated, even with the use of a constant *CFL* number. The smallest actual time step observed during these iterations needed to allow the flow to fully develop was monitored, and then this fixed time step was imposed for the iterations in which the turbulent statistics were accumulated.

Each of the two-dimensional calculations were run for approximately three average flow-through periods, once the initial flowfield in the entire domain was established. This number of flow-through periods was sufficient to allow the mean velocity and turbulence statistics to reach converged levels. Due to the larger turbulent unsteadiness that was found in the three dimensional calculations, these calculations were run for approximately four average flow-through periods, once the flowfield in the entire computational domain was fully developed.

APPENDIX D

TIME SERIES OF INITIAL MIXING LAYER DEVELOPMENT

In this appendix, a time series of density and entropy contours are provided to illustrate the initial mixing layer development for a three dimensional hybrid method calculation of the Goebel-Dutton experiment. The computation discussed here used the standard length scale expression and $C_s = 0.1$ with the Smagorinsky subgrid scale model. As discussed in chapter 5, the density contours provide a close analogy to the Schlieren photographic technique used in experiments to illustrate mixing layer development. In addition, entropy contours enable emphasis to be placed on the shear layer alone, and do not show the Mach wave contours between the shear layer and the mixing section walls that are evident in the density contours. These entropy contours are generated using the entropy function of the PLOT3D program. In reference [109] the entropy function is defined as:

$$S - S_{ref} = C_v \ln \left(\frac{P}{P_{ref}} \right) + C_P \ln \left(\frac{\rho_{ref}}{\rho} \right) \quad (D.1)$$

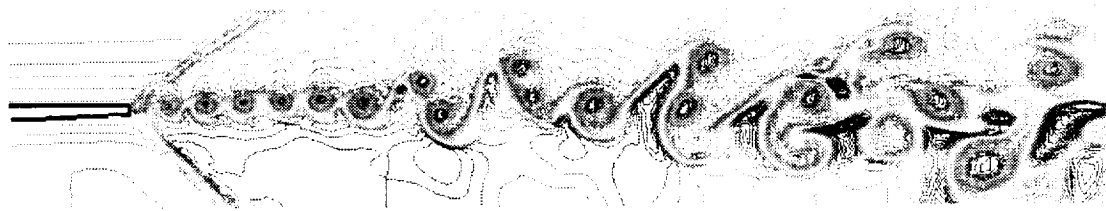
Figures D.1 and D.2 show sixteen snapshots of the density and entropy contours, respectively. Each successive snapshot represents a march forward in time of

3.7×10^{-6} seconds, which corresponds to 250 time steps obtained with the Gottlieb-Turkel predictor-corrector scheme. This time interval was chosen such that in every other snapshot, a new vortex is shed from the trailing edge of the splitter. The initial organized vortex pattern, which very similar to the Karman vortex street characteristic of the separated flow past a cylinder, extends approximately the length of six vortices before the mixing layer disintegrates into a more turbulent pattern.

With the shedding of new vortices occurring approximately every 500 time steps with the numerical scheme, or 7.4×10^{-6} seconds, a Strouhal number may be calculated for further analogy with the separated flow past a cylinder, where in this case of the separated flow past the splitter plate:

$$St = \frac{fH}{\Delta U} \quad (D.2)$$

Using the splitter plate base height of 0.5 mm and the difference in velocities of the two incoming streams equal to 300 m/s, the calculated Strouhal number is 0.225, which is very close to the Strouhal numbers found for flow past cylinders [54, 74] of 0.20 - 0.21.



(a) $t = 1$



(b) $t = 2$



(c) $t = 3$



(d) $t = 4$

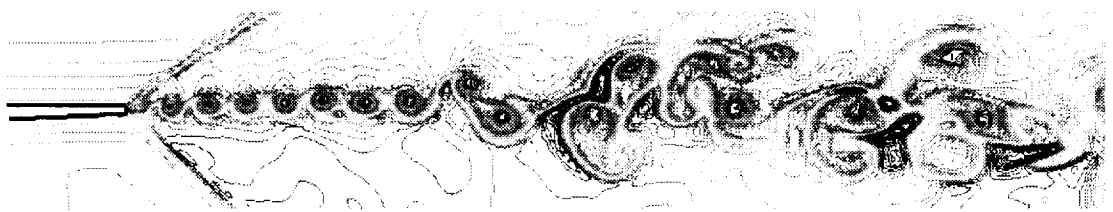
Figure D.1: Time series of density contours for the 3D hybrid calculation using the standard length scale expression and $C_s = 0.10$



(e) $t = 5$



(f) $t = 6$

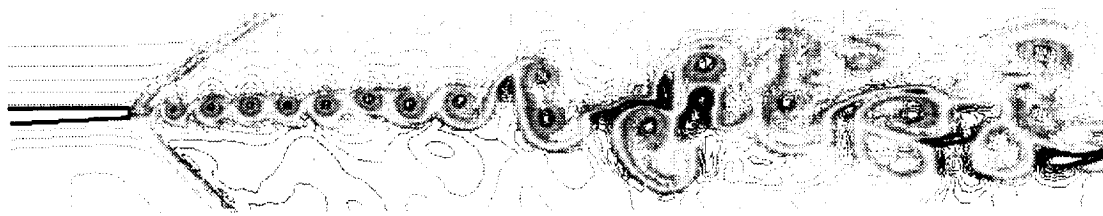


(g) $t = 7$

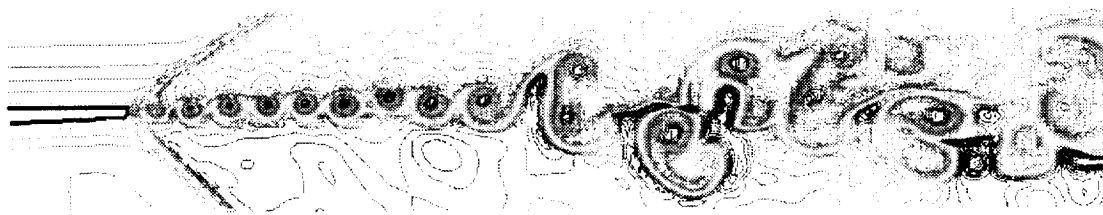


(h) $t = 8$

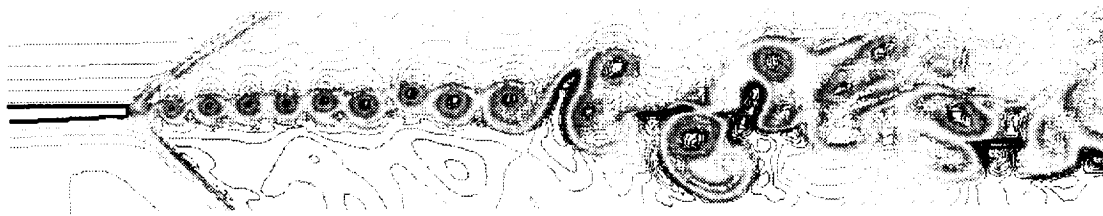
Figure D.1: Continued



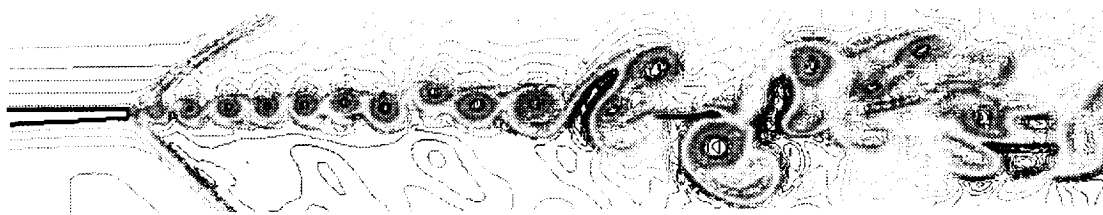
(i) $t = 9$



(j) $t = 10$

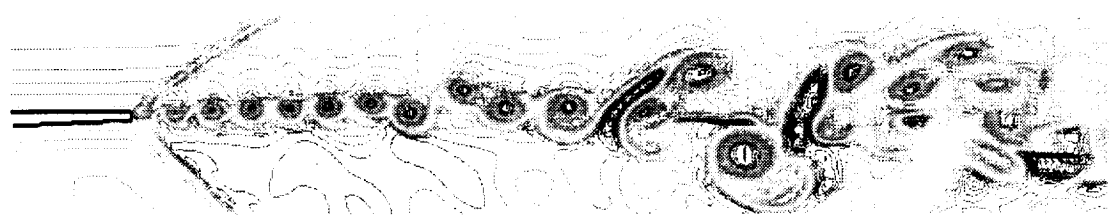


(k) $t = 11$

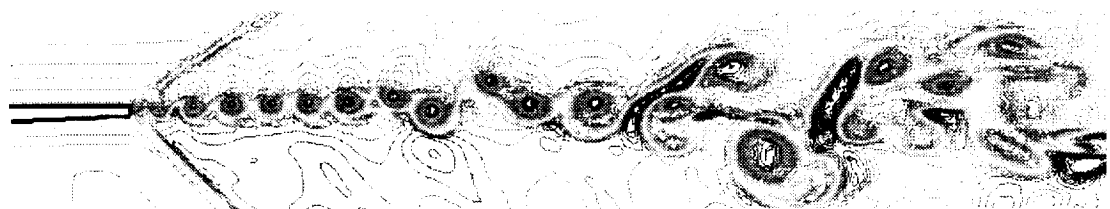


(l) $t = 12$

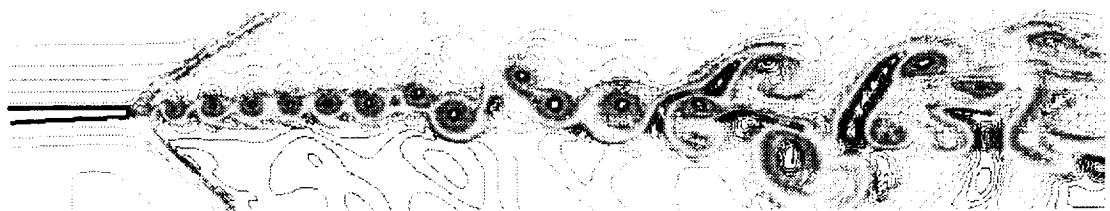
Figure D.1: Continued



(m) $t = 13$



(n) $t = 14$

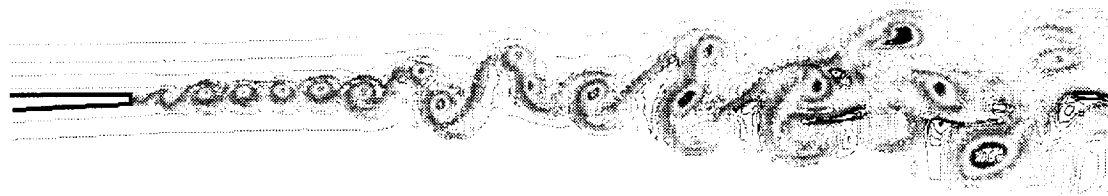


(o) $t = 15$

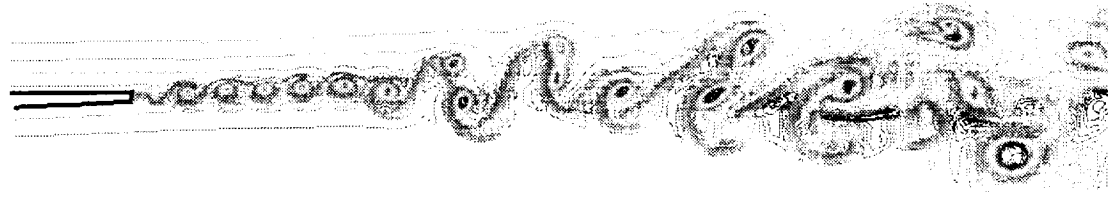


(p) $t = 16$

Figure D.1: Concluded



(a) $t = 1$



(b) $t = 2$

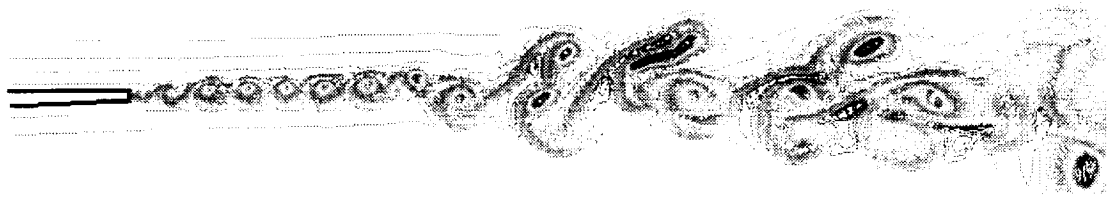


(c) $t = 3$

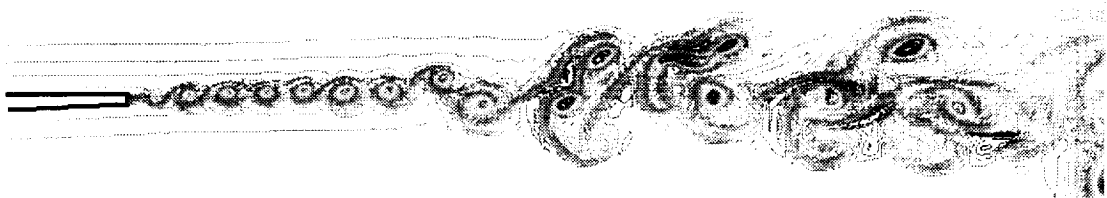


(d) $t = 4$

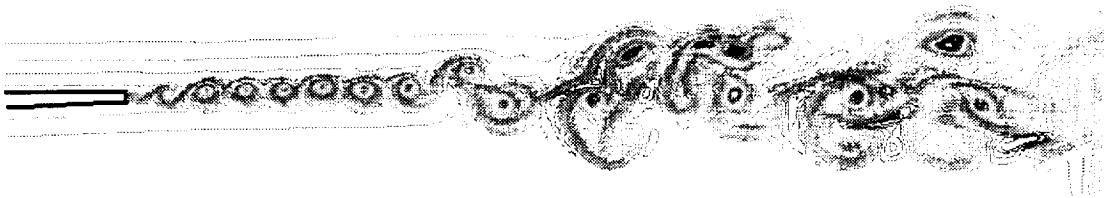
Figure D.2: Time series of entropy contours for the 3D hybrid calculation using the standard length scale expression and $C_s = 0.10$



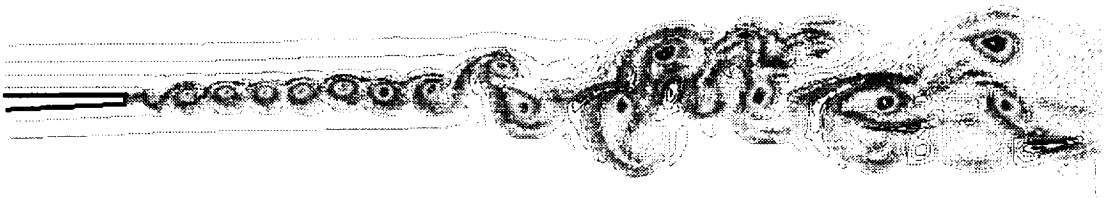
(e) $t = 5$



(f) $t = 6$



(g) $t = 7$

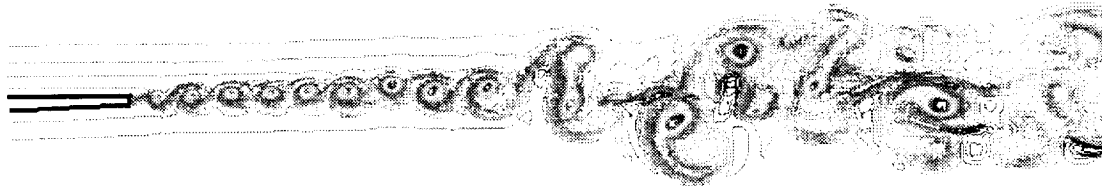


(h) $t = 8$

Figure D.2: Continued



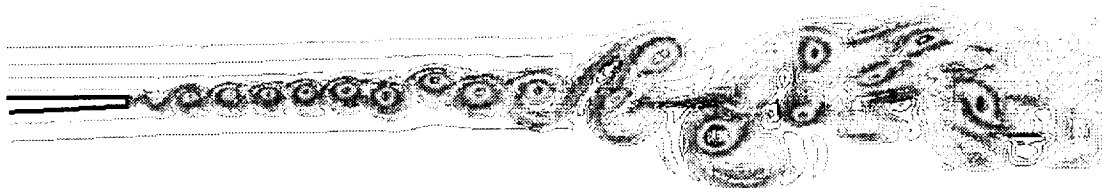
(i) $t = 9$



(j) $t = 10$

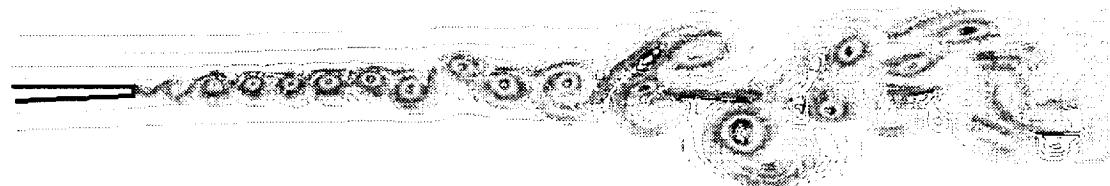


(k) $t = 11$

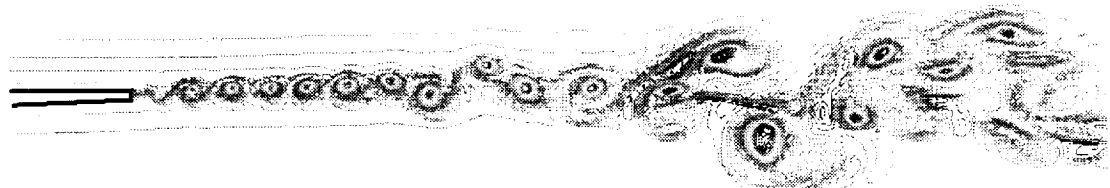


(l) $t = 12$

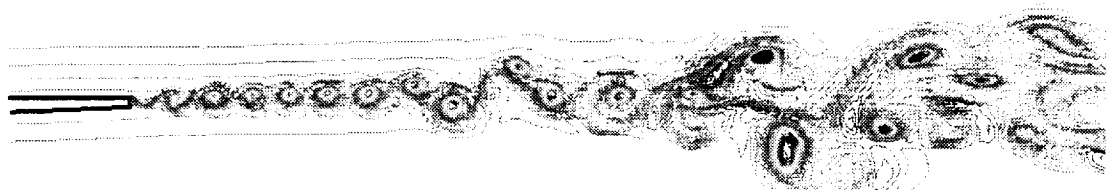
Figure D.2: Continued



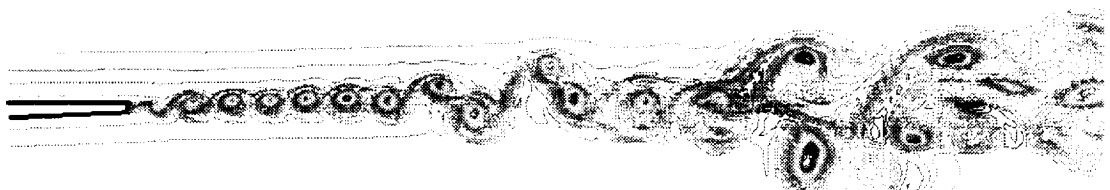
(m) $t = 13$



(n) $t = 14$



(o) $t = 15$



(p) $t = 16$

Figure D.2: Concluded

BIBLIOGRAPHY

Arunajatesan, N., Sinha, N., and Menon, S., "Toward Hybrid LES-RANS Computations of Cavity Flowfields," AIAA Paper 2000-0401, 2000. [1]

Avva, R., Smith, C., and Singhal, A., "Comparative Study of High and Low Reynolds Number Version of k-e Models," AIAA Paper 90-0246, 1990. [2]

Baldwin, B.S. and Barth, T.J., "A One Equation Turbulent Transport Model for High Reynolds Number Wall-Bounded Flows," AIAA Paper 91-0610, 1991. [3]

Baldwin, B.S. and Lomax, H., "Thin Layer Approximation and Algebraic Model for Separated Turbulent Flows," AIAA Paper 78-257, 1978. [4]

Barber, T.J., Chiappetta, L.M., DeBonis, J.R., Georgiadis, N.J., and Yoder, D.A., "An Assessment of Parameters Influencing the Prediction of Shear Layer Mixing," *AIAA Journal of Propulsion and Power*, **15** (1), 45-53, 1999. [5]

Bardina, J.E., Huang, P.G., and Coakley, T.J., "Turbulence Modeling Validation, Testing, and Development," NASA Technical Memorandum 110446, 1997. [6]

Batten, P., Goldberg, U., and Chaknavarthy, S., "Sub-Grid Turbulence Modeling for Unsteady Flow with Acoustic Resonance," AIAA Paper 2000-0473, 2000. [7]

Bayliss, A., Maestrello, L., Parikh, P., and Turkel, E., "Numerical Simulation of Boundary Layer Excitation by Surface Heating and Cooling," *AIAA Journal*, **24** (1) 1095-1101, 1986. [8]

Bayliss, A., Parikh, P., Maestrello, L. and Turkel, E., "A Fourth-Order Scheme for the Unsteady Compressible Navier-Stokes Equations," NASA CR 177994, 1985. [9]

Birch, S.F., "The Role of Structure in Turbulent Mixing," AIAA Paper 97-2636, 1997. [10]

Blasius, H., "The Boundary Layers in Fluids with Little Friction," (in German), *Zeitschrift fur Mathematik und Physik*, **56** (1), 1-37, 1908. English Translation available in NACA TM 1256. [11]

Bogdanoff, D.W., "Compressibility Effects in Turbulent Shear Layers," *AIAA Journal*, **21** (6), 926-927, 1983. [12]

Bradshaw, P., "The Effect of Initial Conditions on the Development of a Free Shear Layer," *Journal of Fluid Mechanics*, **26**, 225-236, 1966. [13]

Bradshaw, P., "Turbulence: The Chief Outstanding Difficulty of Our Subject," In *The Fifth Symposium on Numerical and Physical Aspects of Aerodynamic Flows*, California State University, Stewartson Memorial Lecture, 1993. [14]

Browand, F.K. and Latigo, B.O., "Growth of the Two-Dimensional Mixing Layer from a Turbulent and Nonturbulent Boundary Layer," *Physics of Fluids*, **22** (6), 1011-1019, 1979. [15]

Brown, G.L., and Roshko, A., "On Density Effects and Large Structures in Turbulent Mixing Layers," *Journal of Fluid Mechanics*, **64**, 775-816, 1974. [16]

Bui, T.T., *A Parallel Finite Volume Algorithm for Large-Eddy Simulation of Turbulent Flows*. PhD thesis, Stanford University, 1998. [17]

Cebeci, T., "Calculation of Compressible Turbulent Boundary Layers with Heat and Mass Transfer," AIAA Paper 70-741, 1970. [18]

Cebeci, T. and Smith, A.M.O., *Analysis of Turbulent Boundary Layers*, Academic Publishers, 1974. [19]

Choi, D., Barber, T.J., and Chiappetta, L.M., "Large Eddy Simulation of High-Reynolds Number Jet Flows," AIAA Paper 99-0230, 1999. [20]

Clemens, N.T., and Mungal, M.G., "Two- and Three-Dimensional Effects in the Supersonic Mixing Layer," *AIAA Journal*, **30** (4), 973-981, 1992. [21]

Coakley, T.J., Horstman, C.C., Marvin, J.G., Viegas, J.R., Bardina, J.E., Huang, P.G., and Kussoy, M.I., "Turbulence Compressibility Corrections," NASA Technical Memorandum 108827, 1994. [22]

Constantinescu, G.S. and Squires, K.D., "LES and DES Investigations of Turbulent Flow over a Sphere," AIAA Paper 2000-0540, 2000. [23]

Cziesla, T., Braun, H., Biswas, G., and Mitra, N.K., "Large Eddy Simulation in a Channel with Exit Boundary Conditions," NASA Contractor Report 198304, 1996. [24]

Deardorff, J.W., "A Numerical Study of Three-Dimensional Turbulent Channel Flow at Large Reynolds Numbers," *Journal of Fluid Mechanics*, **41**, 453-480, 1970. [25]

El-Hady, N.M., Zang, T.A., and Piomelli, U., "Application of the Dynamic Subgrid Scale Model to Axisymmetric Transitional Boundary Layer at High Speed," *Physics of Fluids A*, **6** (3), 1299-1309, 1994. [26]

Erlebacher, G., Hussaini, M.Y., Speziale, C.G., and Zang, T.A., "Toward the Large-Eddy Simulation of Compressible Turbulent Flows," NASA CR 187460, 1990, see also ICASE Report 90-76. [27]

Escher, W.J.D., "Synerjet for Earth/Orbit Propulsion: Revisiting the 1966 NASA/Marquardt Composite (Airbreathing/Rocket) Propulsion System Study," SAE Paper 851163, 1985. [28]

Fureby, C. and Grinstein, F.F., "Monotonically Integrated Large Eddy Simulation of Free Shear Layer Flows," *AIAA Journal*, **37** (5), 544-556, 1999. [29]

Georgiadis, N.J., Walker, J.F., and Trefny, C.J., "Parametric Studies of the Ejector Process Within a Turbine-Based Combined-Cycle Propulsion System," AIAA Paper 98-0936, 1998. [30]

Georgiadis, N.J. and Yoder, D.A., "Use of Navier-Stokes Methods for the Calculation of High-Speed Nozzle Flow Fields," AIAA Paper 94-3212, 1994. [31]

Georgiadis, N.J., Yoder, D.A., and DeBonis, J.R., "A Comparison of Three Navier-Stokes Solvers for Exhaust Nozzle Flowfields," AIAA Paper 99-0748, 1999. [32]

Germano, M., Piomelli, U., Moin, P., and Cabot, W.H., "A Dynamic Subgrid-Scale Eddy Viscosity Model," *Physics of Fluids A*, **3** (7), 1760-1765, 1991. [33]

Goebel, S.G., *An Experimental Investigation of Compressible Turbulent Mixing Layers*, PhD thesis, University of Illinois at Urbana-Champaign, 1990. [34]

Goebel, S.G., and Dutton, J.C., "Velocity Measurements of Compressible Turbulent Mixing Layers," AIAA Paper 90-0709, 1990. [35]

Goebel, S.G., and Dutton, J.C., "An Experimental Study of Turbulent Compressible Mixing Layers," *AIAA Journal*, **29** (4), 538-546, 1991. [36]

Gottlieb, D. and Turkel, E., "Dissipative Two-Four Methods for Time-Dependent Problems," *Mathematics of Computation*, **30** (136), 703-723, 1976. [37]

Hedges, L.S. and Eberhardt, S., "Numerical Simulation of Total Temperature Separation in Jets," AIAA Paper 92-0535, 1992. [38]

Hixon, D.R., "On Increasing the Accuracy of MacCormack Schemes for Aeroacoustic Applications," NASA Contractor Report 202311, 1996. [39]

Hixon, D.R., "Prefactored Compact Filters for Computational Aeroacoustics," AIAA Paper 99-0358, 1999. [40]

Hixon, D.R., Shih, S.H., Dong, T., and Mankbadi, R.R., "Evaluation of Generalized Coordinate Transformations Applied to High-Accuracy Finite-Difference Schemes," AIAA Paper 98-0370, 1998. [41]

Hoffman, K.A., Chiang, S.T., Siddiqui, S., and Papadakis, M., *Fundamental Equations of Fluid Mechanics*, Engineering Education System, 1996. [42]

Hudson, D.A. and Long, L.N., "Time Accurate Application of the MacCormack 2-4 Scheme on Massively Parallel Computers," In *ICASE/LaRC Workshop on Benchmark Problems in Computational Aeroacoustics*, pages 209–215, 1995. [43]

Hussain, A.K.M.F. and Clark, A.R., "Upstream Influence on the Near Field of a Plane Turbulent Jet," *Physics of Fluids*, **20** (9), 1416-1425, 1977. [44]

Inoue, O., "Vortex Simulation of a Turbulent Mixing Layer," *AIAA Journal*, **23** (3), 367-373, 1985. [45]

Jameson, A., Schmidt, W., and Turkel, E., "Numerical Solutions of the Euler Equations by Finite Volume Methods Using Runge-Kutta Time-Stepping Schemes," AIAA Paper 81-1259, 1981. [46]

Jones, W.P. and Launder, B.E., "The Prediction of Laminarization with a Two-Equation Model of Turbulence," *International Journal of Heat and Mass Transfer*, **15**, 301-331, 1972. [47]

Kennedy, C.A. and Carpenter, M.H., "Several New Numerical Methods for Compressible Shear-Layer Simulations," *Applied Numerical Mathematics*, **14**, 397-433, 1994. [48]

Kennedy, C.A. and Carpenter, M.H., "Comparison of Several Numerical Methods for Simulation of Compressible Shear Layers," NASA TP 3484, 1997. [49]

Khavaran, A. and Georgiadis, N.J., "Aeroacoustics of Supersonic Elliptic Jets," AIAA Paper 96-0641, 1996. [50]

Khavaran, A., Krejsa, E.A., and Kim C.M., "Computation of Supersonic Jet Mixing Noise for an Axisymmetric Convergent-Divergent Nozzle," *AIAA Journal of Aircraft*, **31** (3), 603-609, 1994. [51]

Klebanoff, P.S., "Characteristics of Turbulence in a Boundary Layer with Zero Pressure Gradient," NACA Technical Note 3178, 1954. [52]

Klebanoff, P.S., "Characteristics of Turbulence in a Boundary Layer with Zero Pressure Gradient," NACA Report 1247, 1955. [53]

Kuethe, A.M. and Chow, C.Y., *Foundations of Aerodynamics*, John Wiley and Sons, fourth edition, 1986. [54]

Lele, S.K., "Compact Finite Difference Schemes with Spectral-like Resolution," *Journal of Computational Physics*, **103**, 16-42, 1992. [55]

Lele, S.K., "Computational Aeroacoustics: A Review," AIAA Paper 97-0018, 1997. [56]

Li, N., Balaras, E., and Piomelli, U., "Inflow Conditions for Large-Eddy Simulations of Mixing Layers," *Physics of Fluids*, **12** (4), 935-938, 2000. [57]

Lilly, D.K., "On the Computational Stability of Numerical Solutions of Time-Dependent Non-Linear Geophysical Fluid Dynamic Problems," *Monthly Weather Review*, **93** (1), 11-26, 1965. [58]

Liou, T.M., Lien, W.Y., and Hwang, P.W., "Compressibility Effects and Mixing Enhancement in Turbulent Free Shear Flows," *AIAA Journal*, **33** (12), 2332-2338, 1995. [59]

Lyrintzis, A.S., "Review: The Use of Kirchoff's Method in Computational Aeroacoustics," *Journal of Fluids Engineering*, **166**, 665-676, 1994. [60]

MacCormack, R.W., "The Effect of Viscosity in Hypervelocity Impact Cratering," AIAA Paper 69-354, 1969. [61]

MacCormack, R.W., "Numerical Solution of the Interaction of a Shock Wave with a Laminar Boundary Layer," In *Lecture Notes in Physics*, Volume 8, 151-163, Springer-Verlag, Proceedings of the Second International Conference on Numerical Methods for Fluid Dynamics, 1971. [62]

Mager, A., "Transformation of the Compressible Turbulent Boundary Layer," *Journal of the Aeronautical Sciences*, **25** (4), 305-311, 1958. [63]

Mani, M., "A Compressible Wall Function for Steady and Unsteady Flow Applications," AIAA Paper 99-3216, 1999. [64]

Mankbadi, R.R., Shih, S.H., Hixon, D.R., and Povinelli, L.A., "Direct Computation of Sound Radiation by Jet Flow Using Large Scale Equations," AIAA Paper 95-0680, 1995. [65]

Menter, F.R., "Improved Two-Equation $k-\omega$ Turbulence Models for Aerodynamic Flows," NASA Technical Memorandum 103975, 1992. [66]

Menter, F.R., "Two-Equation Eddy-Viscosity Turbulence Models for Engineering Applications," *AIAA Journal*, **32** (8), 1598-1605, 1994. [67]

Mittal, R. and Moin, P., "Suitability of Upwind-Biased Finite Difference Schemes for Large Eddy Simulations," *AIAA Journal*, **35** (8), 1415-1417, 1997. [68]

Moin, P. and Jimenez, J., "Large Eddy Simulation of Complex Turbulent Flows," AIAA Paper 93-3099, 1993. [69]

Nelson, C. and Menon, S., "Unsteady Simulations of Compressible Spatial Mixing Layers," AIAA Paper 98-0786, 1998. [70]

Nelson, C.C., *Simulations of Spatially Evolving Compressible Turbulence Using a Local Dynamic Subgrid Model*, PhD thesis, Georgia Institute of Technology, 1997. [71]

Nichols, R.H., "Development and Validation of a Two-Equation Turbulence Model with Wall Functions for Compressible Flow," AIAA Paper 96-2385, 1996. [72]

Ota, D.K. and Goldberg, U.C., "Law of the Wall with Consistent No-Slip Limit," AIAA Paper 97-2246, 1997. [73]

Panton, R.L., *Incompressible Flow*, John Wiley and Sons, 1984. [74]

Pao, S.P. and Abdol-Hamid, K.S., "Numerical Simulation of Jet Aerodynamics Using the Three-Dimensional Navier-Stokes Code PAB3D," NASA Technical Paper 3596, 1996. [75]

Papamoschou, D. and Roshko, A., "The Compressible Turbulent Shear Layer: An Experimental Study," *Journal of Fluid Mechanics*, **197**, 453-477, 1988. [76]

Piomelli, U., "High Reynolds Number Calculations Using the Dynamic Subgrid-Scale Model," *Physics of Fluids A*, **5** (6), 1484-1490, 1993. [77]

Piomelli, U., "Large Eddy Simulations: Present State and Future Directions," *AIAA Paper 98-0534*, 1998. [78]

Pope, S.B., "An Explanation of the Turbulent Round-Jet Plane-Jet Anomaly," *AIAA Journal*, **16** (3), 279-280, 1978. [79]

Pulliam, T.H., "Artificial Dissipation Models for the Euler Equations," *AIAA Journal*, **24** (12), 1931-1940, 1986. [80]

Ragab, S.A. and Sheen, S.-C., "An Investigation of Finite-Difference Methods for Large-Eddy Simulation of a Mixing Layer," *AIAA Paper 92-0554*, 1992. [81]

Ragab, S.A. and Sheen, S.-C., "Large Eddy Simulation of Mixing Layers," In B. Galerpin and S.A. Orszag, editors, *Large Eddy Simulation of Complex Engineering and Geophysical Flows*, pages 255-285, Cambridge University Press, 1993. [82]

Reynolds, W.C., "The Potential and Limitations of Direct and Large Eddy Simulations," In *Whither Turbulence? Turbulence at the Crossroads, Lecture Notes in Physics*, pages 313-343, Springer-Verlag, 1990. [83]

Rodi, W. and Scheuerer, G., "Scrutinizing the $k-\epsilon$ Turbulence Model Under Adverse Pressure Gradient Conditions," *Journal of Fluids Engineering, Transactions of the A.S.M.E.*, **108**, 174-179, 1986. [84]

Rogallo, R.S. and Moin, P., "Numerical Simulation of Turbulent Flows," *Annual Review of Fluid Mechanics*, **17**, 99-137, 1984. [85]

Roshko, A., "Structure of Turbulent Shear Flows: A New Look," *AIAA Journal*, **14** (10), 1349-1357, 1976. [86]

Sandham, N.D. and Reynolds, W.C., "Compressible Mixing Layer: Linear Theory and Direct Simulation," *AIAA Journal*, **28** (4), 618-624, 1990. [87]

Sarkar, S., Erlerbacher, G., Hussaini, M.Y., and Kreiss, H.O., "The Analysis and Modeling of Dilatational Terms in Compressible Turbulence," *Journal of Fluid Mechanics*, **227**, 473-493, 1991. [88]

Sarkar, S. and Lakshmanan, B., "Application of a Reynolds Stress Turbulence Model to the Compressible Shear Layer," *AIAA Journal*, **29** (5), 743-749, 1990. [89]

Schlichting, H., *Boundary-Layer Theory*, McGraw-Hill, seventh edition, Translated by J. Kestin, 1979. [90]

Seiner, J.M. and Krejsa, E.A., "Supersonic Jet Noise and the High Speed Civil Transport," AIAA Paper 89-2358, 1989. [91]

Shih, S.H., Hixon, D.R., Mankbadi, R.R., Pilon, A., and Lyrintzis, A.S., "Evaluation of Far-Field Jet Noise Prediction Methods," AIAA Paper 97-0282, 1997. [92]

Sinha, N., Lee, R.A., Dash, S.M., and Pelz, R.B., "Advances in 3D Unsteady Jet Simulation Using LES Methodology in a Parallel Environment," AIAA Paper 96-1779, 1996. [93]

Smagorinsky, J., "General Circulation Experiments with the Primitive Equations," *Monthly Weather Review*, **91**, 99-164, 1963. [94]

Snyder, R.D. and Scott, J.N., "Comparison of Numerical Schemes for the Analysis Aeroacoustics," AIAA Paper 99-0354, 1999. [95]

Spalart, P.R., "Strategies for Turbulence Modeling and Simulations," *International Journal of Heat and Fluid Flow*, **21** (3), 252-263, 2000. [96]

Spalart, P.R., "Trends in Turbulence Treatments," AIAA Paper 2000-2306, 2000. [97]

Spalart, P.R. and Allmaras, S.R., "A One-Equation Turbulence Model for Aerodynamic Flows," *La Recherche Aerospatiale*, **1** (1), 5-21, 1994. [98]

Spalart, P.R., Jou, W.H., Strelets, M., and Allmaras, S.R., "Comments on the Feasibility of LES for Wings, and on a Hybrid RANS/LES Approach," In *First AFOSR International Conference on DNS/LES*, 1997. [99]

Speziale, C.G., "Turbulence Modeling for Time-Dependent RANS and VLES: A Review," *AIAA Journal*, **36** (2), 173-184, 1998. [100]

Steffen, C.J., Smith, T.D., Yungster, S., and Keller, D.J., "Rocket Based Combined-Cycle Analysis Using NPARC," AIAA Paper 98-0954, 1998. [101]

Thies, A.T. and Tam, C.K.W., "Computation of Turbulent Axisymmetric and Nonaxisymmetric Jet Flows Using the $k-\epsilon$ Model," *AIAA Journal*, **34** (2), 309-316, 1996. [102]

Trefny, C.J., "An Air-Breathing Launch Vehicle Concept for Single-Stage-to-Orbit," AIAA Paper 99-2730, 1999. [103]

Trefny, C.J. and Benson, T.J., "An Integration of the Turbojet and Single-Throat Ramjet," NASA Technical Memorandum 107085, 1995. [104]

Tucker, M., "Approximate Calculation of Turbulent Boundary-Layer Development in Compressible Flow." NASA Technical Note 2337, 1951. [105]

Viegas, J.R. and Rubesin, M.W., "A Comparative Study of Several Compressibility Corrections to Turbulence Models Applied to High-Speed Shear Layers," AIAA Paper 91-1783, 1991. [106]

Vreman, A.W., *Direct and Large-Eddy Simulation of the Compressible Turbulent Mixing Layer*, PhD thesis, Twente University, 1995. [107]

Vreman, A.W., Geurts, B.J., and Kuerten, J.G.M., "Subgrid-Modelling in LES of Compressible Flow," In P.R. Voke, L. Kleiser, and J.P. Chollet, editors, *Direct and Large-Eddy Simulation I*, 133-144. Kluwer Academic Publishers, 1994. [108]

Walatka, P.P., Buning, P.G., Pierce, L., and Elson, P.A., "PLOT3D User's Manual." NASA Technical Memorandum 101067, 1990. [109]

White, F.M., *Viscous Fluid Flow*, McGraw-Hill, 1974. [110]

White, F.M. and Christoph, G.H., "A Simple Analysis of Compressible Turbulent Two-Dimensional Skin Friction Under Arbitrary Conditions," AFFDL Technical Report 70-133, 1970. [111]

Wieghardt, K. and Tillman, W., "On the Turbulent Friction Layer for Rising Pressure," NASA Technical Memorandum 1314, 1951. [112]

Wilcox, D.C., "Simulation of Transition with a Two-Equation Turbulence Model," *AIAA Journal*, **32** (2), 247-255, 1994. [113]

Wilcox, D.C., *Turbulence Modeling for CFD*, DCW Industries, second edition, 1998. [114]

Zeman, O., "Dilatational Dissipation: The Concept and Application in Modeling Compressible Mixing Layers," *Physics of Fluids A*, **2** 178-188, 1990. [115]

REPORT DOCUMENTATION PAGE			Form Approved OMB No. 0704-0188
<p>Public reporting burden for this collection of information is estimated to average 1 hour per response, including the time for reviewing instructions, searching existing data sources, gathering and maintaining the data needed, and completing and reviewing the collection of information. Send comments regarding this burden estimate or any other aspect of this collection of information, including suggestions for reducing this burden, to Washington Headquarters Services, Directorate for Information Operations and Reports, 1215 Jefferson Davis Highway, Suite 1204, Arlington, VA 22202-4302, and to the Office of Management and Budget, Paperwork Reduction Project (0704-0188), Washington, DC 20503.</p>			
1. AGENCY USE ONLY (Leave blank)	2. REPORT DATE	3. REPORT TYPE AND DATES COVERED	
	May 2001	Technical Memorandum	
4. TITLE AND SUBTITLE		5. FUNDING NUMBERS	
A Hybrid Numerical Method for Turbulent Mixing Layers		WU-708-90-43-00	
6. AUTHOR(S)			
Nicholas J. Georgiadis			
7. PERFORMING ORGANIZATION NAME(S) AND ADDRESS(ES)		8. PERFORMING ORGANIZATION REPORT NUMBER	
National Aeronautics and Space Administration John H. Glenn Research Center at Lewis Field Cleveland, Ohio 44135-3191		E-12726	
9. SPONSORING/MONITORING AGENCY NAME(S) AND ADDRESS(ES)		10. SPONSORING/MONITORING AGENCY REPORT NUMBER	
National Aeronautics and Space Administration Washington, DC 20546-0001		NASA TM—2001-210811	
11. SUPPLEMENTARY NOTES			
<p>This report was submitted as a thesis in partial fulfillment of the requirements for the degree Doctor of Philosophy to Case Western Reserve University, Cleveland, January 2001. Responsible person, Nicholas J. Georgiadis, organization code 5860, 216-433-3958.</p>			
12a. DISTRIBUTION/AVAILABILITY STATEMENT		12b. DISTRIBUTION CODE	
Unclassified - Unlimited Subject Categories: 02 and 34 Available electronically at http://gltrs.grc.nasa.gov/GLTRS This publication is available from the NASA Center for AeroSpace Information, 301-621-0390.		Distribution: Nonstandard	
13. ABSTRACT (Maximum 200 words)			
<p>A hybrid method has been developed for simulations of compressible turbulent mixing layers. Such mixing layers dominate the flows in exhaust systems of modern day aircraft and also those of hypersonic vehicles currently under development. The method developed here is intended for configurations in which a dominant structural feature provides an unsteady mechanism to drive the turbulent development in the mixing layer. The hybrid method uses a Reynolds-averaged Navier-Stokes (RANS) procedure to calculate wall bounded regions entering a mixing section, and a Large Eddy Simulation (LES) procedure to calculate the mixing dominated regions. A numerical technique was developed to enable the use of the hybrid RANS-LES method on stretched, non-Cartesian grids. Closure for the RANS equations was obtained using the Cebeci-Smith algebraic turbulence model in conjunction with the wall-function approach of Ota and Goldberg. The wall-function approach enabled a continuous computational grid from the RANS regions to the LES region. The LES equations were closed using the Smagorinsky subgrid scale model. The hybrid RANS-LES method is applied to a benchmark compressible mixing layer experiment. Preliminary two dimensional calculations are used to investigate the effects of axial grid density and boundary conditions. Vortex shedding from the base region of a splitter plate separating the upstream flows was observed to eventually transition to turbulence. The location of the transition, however, was much further downstream than indicated by experiments. Actual LES calculations, performed in three spatial directions, also indicated vortex shedding, but the transition to turbulence was found to occur much closer to the beginning of the mixing section, which is in agreement with experimental observations. These calculations demonstrated that LES simulations must be performed in three dimensions. Comparisons of time-averaged axial velocities and turbulence intensities indicated reasonable agreement with experimental data.</p>			
14. SUBJECT TERMS			15. NUMBER OF PAGES 237
Turbulent mixing; Nozzle; Compressibility; Large eddy simulation; Navier-Stokes			16. PRICE CODE
17. SECURITY CLASSIFICATION OF REPORT Unclassified	18. SECURITY CLASSIFICATION OF THIS PAGE Unclassified	19. SECURITY CLASSIFICATION OF ABSTRACT Unclassified	20. LIMITATION OF ABSTRACT



